NTNU

Norwegian University of
Science and Technology

Hydrodynamic effects regarding free-fall lifeboat for compressible air in CFD simulations

Andreas Grung Svendsen

Marine Technology

Submission date: June 2017

Supervisor: Marilena Greco, IMT

Co-supervisor: Sebastien Fouques, Sintef
Andrea Califano, DNV-Gl

Norwegian University of Science and Technology
Department of Marine Technology

MASTER THESIS IN MARINE TECHNOLOGY

Spring 2017

FOR

Andreas Grung Svendsen

Hydrodynamic effects relevant for free falling lifeboat modelled with compressible air

(Hydrodynamiske effekter relevante for frittfallende livbåt modellert med komprimerbar luft)

Free-falling lifeboats represent a good alternative to conventional, davit launched, lifeboats (lowered to sea by means of cables) because they require shorter time for launching and can have more momentum for escaping the host ship/platform. The different phases of their evolution have been investigated during the project thesis with focus on the water-entry and later stages. A simplified body geometry was modelled numerically and studied with a selected CFD commercial solver assuming calm-water conditions and incompressible air.

The project activity was carried out together with two other master students. The master thesis will be individually carried out but with some shared investigations.

Objective

Present master thesis aims to continue the numerical investigations started during the project thesis focusing on the influence of water compressibility on the lifeboat behaviour during water-entry and later stages.

The work should be carried out in steps as follows:

1. Summarize major findings/outcomes from the project thesis and investigate possible reasons for questions left open. The latter part will be carried out in collaboration with the other two students working on the same simplified lifeboat concept.
2. Complement the literature study of the project with state-of-the-art works on numerical/experimental/theoretical studies on air-compressibility models and their effects relevant for the topic of interest.
3. Use the simplified lifeboat geometry studied during the project thesis and perform a systematic numerical study on the relevant parameters connected with initial conditions, assuming calm water and incompressible air, and using the CFD solver selected in the project work.
4. Using findings from the literature study performed in step 2 and for different initial conditions, perform a numerical investigation on the influence of air compressibility on the lifeboat behaviour using the CFD solver selected in the project work. Study the sensitivity of the results to the assumption of incompressible air and to use of different models for the air.

The work may show to be more extensive than anticipated. Some topics may therefore be left out after discussion with the supervisor without any negative influence on the grading.

The candidate should in his report give a personal contribution to the solution of the problem formulated in this text. All assumptions and conclusions must be supported by mathematical models and/or references to physical effects in a logical manner.

The candidate should apply all available sources to find relevant literature and information on the actual problem.

The thesis should be organised in a rational manner to give a clear presentation of the work in terms of exposition of results, assessments, and conclusions. It is important that the text is well written and that tables and figures are used to support the verbal presentation. The thesis should be complete, but still as short as possible. In particular, the text should be brief and to the point, with a clear language. Telegraphic language should be avoided.

The thesis must contain the following elements: the text defining the scope (i.e. this text), preface (outlining project-work steps and acknowledgements), abstract (providing the summary), table of contents, main body of thesis, conclusions with recommendations for further work, list of

symbols and acronyms, references and (optional) appendices. All figures, tables and equations shall be numerated.

The supervisor may require that the candidate, in an early stage of the work, present a written plan for the completion of the work. The plan should include budget for the use of computer and laboratory resources that will be charged to the department. Overruns shall be reported to the supervisor.

From the thesis it should be possible to identify the work carried out by the candidate and what has been found in the available literature. It is important to give references to the original source for theories and experimental results.

Supervisor : Marilena Greco

Co-supervisor : Andrea Califano

Co-supervisor : Sebastien Fouques

Submitted :15 January 2017

Deadline :11 June 2017

Marilena Greco

Supervisor

Preface

This thesis is a result of work done in collaboration with other students and induvial work to finish the Master of Science degree in Hydrodynamics.

In early 2016, I, Simen Groth and Vegard Netland decided to look for a master thesis, where we could work together and use each other's knowledge and specialties. In the autumn later that year, we were introduced to a thesis based on computational fluid dynamics, where we could do work in collaboration with each other in addition to individual parts more directed towards individual interests. A busy semester, combined with late accesses to the CFD software, StarCCM+, made the project thesis "Hydrodynamic effects relevant for free-fall lifeboats: preliminary studies" very challenging. The plan for the master thesis following this project, was to use the work done in collaboration with each other and then split up and focus on separate phenomena regarding lifeboat diving. In pursuance of this, we felt that we had to do the project thesis all over again to account for the errors made in, addition to an insufficient literature study. Therefore, the common part of our master thesis became bigger than first anticipated, influencing the time available for our own parts. For my individual part, three compressibility of air models have been compared with the assumption of incompressible air with only one initial condition. To account for this, I have tried to go more in depth when analyzing the differences obtained including damping ratios and comparisons with previous work.

This master thesis could not have been done if it was not for all the help I have received on my way.

First I would like to thank my supervisor, Professor Marilena Greco. She has always been helpful when problems have occurred. This includes everything from providing me relevant literature, useful insight and guidelines for the related problems. In addition to Greco, we had two Co supervisors, Andreas Califano and Sébastien Fouques. I would like to thank Califano for all the help and tips regarding the software Star-CCM+. He has also contributed to helpful discussions regarding lifeboat diving. Fouques has been very helpful regarding the understanding of all the phenomena related to lifeboat diving. His comments and discussion, especially for the literature study, has been very valuable.

I would also like to thank my coworkers Vegard Netland and Simen Groth. Netland has challenged me in the understanding of difficult physics for both the common and individual part. I would like to thank Groth for excellent computational skills, where he has found time to help me with Star-CCM+ and the

supercomputer, Vilje, whenever needed. I would also like to thank my friend Nicholas Mowatt Larssen for proof reading of my individual part with focus on the language.

Abstract

Free falling lifeboats are often used as a last resort evacuation system for fixed or floating offshore installations. Lifeboats are normally resting at a skid which is mounted at the mother vessel, until the hook holding the lifeboat at rest is released. It is important that lifeboat diving is a safe evacuation method. Therefore, the physics related to life boat diving phenomenon is important. Lifeboat diving is divided into launching phase, free falling phase, water entry phase, submerged phase, water exit phase and sail away phase. For a better understanding, these phases are included in a literature study, and compared with relevant literature for each phase. In this master thesis, lifeboat diving has been investigated using computational fluid dynamics (CFD), where the selected solver has been Star-CCM+.

A sensitivity analysis and convergence study were conducted for the incompressible simulation, with focus on how the time step, number iteration and mesh discretization influenced the simulation. This lead to a suitable relation between mesh discretization and time step, including 10 iterations. A convergence analysis was conducted in pursuance of an indication of how much the simulation was effected by the mesh discretization. The two finest mesh discretization were quite similar to each other in a global perspective such as motion, though local phenomena, especially in connection with cavity closure proved different. The order of accuracy was calculated under the assumption that the error approximated for a given quantity was proportional to Δx^{OA}, where Δx is the mesh discretization and OA is the order of accuracy. Since no experiments have been carried out, the exact solution for the problem was unknown. Therefore, a log linear relationship was assumed between the integrated quantity and mesh discretization, in the interest of finding the optimal solution, which the solver should converge towards. The coarsest grid discretization might “miss out on important phenomena due to the large cell size, further influencing the physics. Hence a log linear relation between the integrated quantity and mesh discretization is probably an inaccurate statement for this mesh discretization.

The physics related to a freefalling lifeboat is highly influenced by many parameters, such as wind loads, drop height and wave conditions. It is important to know how these parameters will influence the behavior of the lifeboat. Therefore, a parameter investigation was conducted in collaboration with Simen Groth and Vegard Netland. The main focus was to investigate how various parameters such as maximum submergence, sailing distance and accelerations were influenced by the different initial conditions when air was modeled as incompressible. The lifeboat behavior was less influenced by a

change in the vertical position of the COG_{body}.The maximum submergence and sailing distance were increased, when the COG_{body} was raised in z_{body} direction. The maximum submergence height was most influenced when the water entry angle was reduced or increased by 5 degrees from the initial water entry angle of 60 degree. The change in initial resultant velocity at water entry contributed also to large variations in the submergence. However, the sailing distance proved to be the parameter most effected by the initial water entry velocity. In addition, the cavity closure occurred earlier when the velocity was increased.

To investigate the influence of the compressibility of the air, three different compressible air relations where introduced to the software. These models were based on previous studies regarding air cushions in a tank due to slamming and CFD analysis with air modelled as compressible. The most significant difference was that the pressure on the aft part of the body started to oscillate with a frequency close to the natural frequency of the entrapped air, after cavity closure for the compressible air models. For the incompressible air simulation, only one distinctive pressure peak with much greater amplitude was present. The first pressure peak was also observed later, which might be a result of the compression of the entrapped air, before creating an instant push on the aft part of the body. These pressure oscillations on the aft part of the body, results in oscillating acceleration in x_{body} direction for all the compressible models. The oscillating acceleration in x_{body} direction, seems to oscillate with a mean value close to the acceleration in x_{body} direction for incompressible air, since both the velocities and motions are quite similar, though the sailing distance is a bit longer for incompressible air. The large acceleration peak in x_{body} direction for incompressible air will distinguish when the specified filter for calculations of CAR index is applied. Therefore, incompressible air simulations are most likely appropriate when estimating passenger safety. As for the structural integrity, pressure peaks may cause local failure. As a result of this, filters should not be used for the purposes of removing pressure peaks. In addition, the pressure measurements for compressible and incompressible are quite different. Hence, air should be modelled as compressible for an accurate structure assessment.

The natural frequency for the various compressible air models were found. The polytrophic gas relations showed a smaller natural frequency, compared to the adiabatic relation, which corresponds well with previous studies. The isothermal condition indicated the lowest natural frequency, which was also the case for Ommundsens simulations. The damping ratio of the pressure oscillations was investigated by assuming that the damping resembles the free decay of an under damped linear mass system. In order to get an accurate estimate of the damping, the varying hydrostatic pressure had to be subtracted. This

was done by using a second order Butterworth high pass filter, attenuating frequencies below 1Hz. The reason for conducting the polytrophic gas relation was due to the assumption that heat exchange contributes to damping of the entrapped air, which is not represented when an adiabatic process is assumed. The damping ratio for the polytrophic gas relation was slightly higher than adiabatic, but lower than the damping ratio for the isothermal condition. The author would recommend further studies with the polytrophic gas relations on the grounds of higher natural frequency than the isothermal condition and slightly higher damping ratio compared to the adiabatic process.

Table of content

Nomenclature

ξ	Damping ratio
β	Dead rise angle
Γ	Diffusion vector
γ	Surface tension
$\gamma(2)$	Forcing coefficient
Δt	Time step
Δx	Length of one cell
Δx_i	Mesh discretization, i = 1, 2, 3
δt_1	Expansion time
δt_2	Collapsing time
δ'_{ij}	Kronecker delta
ϵ	Dissipation rate
η	Surface elevation
η_b	Water spray point
θ	Angle
θ_0	Contact angle
κ	Von Karman's constant, polytrophic index,
μ	Dynamic viscosity
ν	Kinematic viscosity
ρ	Fluid density
ρ_{cavity}	Density in the air cavity
ρ_{gas}	Density in air cushion
ρ_l	Liquid density
ρ_0	Initial density at air pocket creation,Initial density at air cavity creation
ρ_s	Solid density
σ_{ij}	Stress tensor
σ_n	Undamped natural frequency of the gas cushion
τ_W	Shear stress
u_τ	Frictional velocity
γ	Vortex density
ϕ_{cav}	Velocity potential on cavity
ϕ	Velocity potential

$C_1(t)$	Velocity potential
F_D	Drag force
Fr	Froude number
F_3	Force in heave
F_n	Normal reaction force
f	Frequency
$f_{stretch}$	Stretch factor
g	Gravity
H_c	Cavity height
H_w	Height of the mean wind velocity
|H (f)|	Frequency domain transfer function
h_p	Pop-up height
I_{ii}	Moments of inertia, i = x, y, z
I_q	Integrated quantity
k	Wave vector
K	Kelvin
k	Kinetic energy
L	Length
M	Mass, molecular weight
m	Meters
N	Newton
P_i	Given pressure peak
R	Specific gas constant
R_u	Universal gas constant
n_{global}	Global coordinate system, n = x, y, z
n_{body}	Body fixed coordinate system, n = x, y, z
p_{abs}	Absolute pressure
p	Pressure
p_{cavity}	Pressure in the air cavity
p_0	Initial pressure at gas pocket creation, initial pressure at air cavity creation
p_d	Dynamic pressure of air cushion
p_{gas}	Pressure in the gas cushion
R	Radius

$\phi(2)$	Transport of a scalar property
$\phi(3)$	Current solution to the transport equation
ϕ^*	Value of the forces solution
S_θ	Source term
q_ϕ	Source term
Ω	Submergence, Cushion volume
$\dot{\Omega}$	Time rate of change of the cushion volume
ω	Frequency in rad/s
∇	Nabla operator
∂	Partial derivative
A	Area
A_{33}	Added mass in heave
A	Surface area of control volume
a_i	Acceleration in i direction, i = x, y, z
a	Surface vector
Bo	Bond number
C_a	Cappilary number
C_D	Drag coefficient
c	Wetted length
D	Diameter

Re	Reynolds number
R_{ii}	Radius of gyration, i = x, y, z
S_z^d	Residence term
s	Seconds
T_a	Average period
T_c	Cavity closure time
t	Time
t_i	Time at given pressure peak
t_0	Air cavity formation starting time
U	Velocity vector
U_w	Wind velocity
u, v, w	Velocity in x, y, z
u^+	Non-dimensional velocity
V	Volume
$v_{x'}$	Velocity in x_{body}
We	Webber number
X_h	Prism layer height
x_{min}	Minimum cell size
Y^+	Non-dimensional wall distance
y	Center of cell height
z_0	Creation position of air cavity
z_{0r}	Roughness length

VOF	Volume of fluid
CFL	Courant Friedrichs Lewy consition
CFD	Computational fluid dynamics
CAR	Combined Acceleration Ratio

VCG	Vertical centre of gravity
2D	Two dimensional
3D	Three dimmensional

1 Introduction

Free falling lifeboats are often used as last resort evacuation system for fixed or floating offshore installations. Free falling lifeboats offer a good alternative to conventional davit launched lifeboats, since they require shorter lunching time. The lifeboat will normally rest at a skid that is mounted at the mother vessel, approximately 20-30 meters above sea level. The evacuation starts when the hook holding the lifeboat is released and the lifeboat start to slide down the skid. The phenomena related to lifeboat diving is divided into launching phase, free falling phase, water entry phase, submerged phase, water exit phase and sail away phase.

The purpose of this paper is to get an insight in the complex problem of free falling lifeboats, since all the phases are dependent on each other. It is important that lifeboat diving is a safe evacuation method. Therefore, the physics related to life boat diving phenomenon is important. In this master thesis, lifeboat diving has been investigated by using computational fluid dynamics (CFD). Another approach is to conduct model test experiments. However, both approaches can be applied, where the results from the experiments can be used as validation for the numerical approach. All the simulations in this paper have been done with a commercial software, called Star-CCM+, where a simplified lifeboat geometry has been applied to simplify the CFD simulation. The geometry replicates a projectile, made by cutting an ellipsoid in the middle.

For all the simulations conducted in collaboration with Vegard Netland and Simen Groth, both air and water have been modelled as incompressible fluids. As for water, the assumption of incompressible fluid is valid due to the small variation in density. The density of air however, is highly influenced of the surrounding pressure and temperature. For a lifeboat, creation of air cavity is expected when penetrating the free surface due to the large dimensions, drop height (.i.e. high velocities) and sharp corners. Air cavity creation is not only present on the very aft part of the body, but also behind appendages on the hull surface, due to the sharp corners. For the simulations, all appendages such as a wheelhouse have been neglected to simplify the lifeboat geometry. Hence, air cavity creation is only present on the aft part of the lifeboat. In case of compressible air, the air cavity will likely alter in size as the surrounding water squishes the entrapped air due to the density difference for the air and water. How the compressibility of air will influence the aspect of a free falling life boat compared with incompressible, will be investigated in the individual part of this paper.

2 Introduction to free-falling lifeboat phases and physics

In the case of free-falling lifeboat diving, the process is divided into different phases. The body operates in different fluids, enters the water in high velocity, gets fully submerged, ascents to the surface and should then it be able to operate as a sailing vessel. This complex matter is thus divided into launching phase, free-falling phase, water entry phase, submerged phase, water exit phase and the sail away phase.

The theory in the submerged phase, water exit phase and partly the water entry phase, will be based on studies of water entering and exiting projectiles and spheres, combined with theory from previous papers regarding free-falling lifeboats.

2.1 Launching phase

The lifeboat will normally rest at a skid mounted on the mother vessel. Several releasing mechanisms for launching are available, most common are the releasing hook. The lifeboat is released from the hook by a manually driven hydraulic pump that is possible to operate from the inside. After releasing, the lifeboat slides along the skid driven by the gravitational and frictional forces. As the boat passes the end of the skid, an increasingly part of the lifeboat will be free falling, while the behind part will have contact with the end of the skid. This will lead to a rotation which depend on the position of the skid in the global coordinate system.

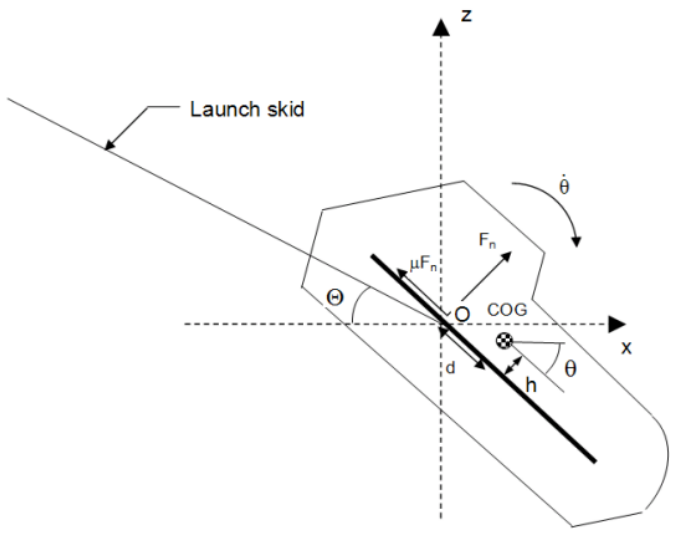

Figure 2.1: Shows the lifeboat on a launch skid, as the center of gravity passes the end of the launch skid.

Assuming a global coordinate system shown in Figure 2.1 where z represents the vertical axis, and x and y the two normal horizontal axes. The gravitational force will act downwards in z-direction. Ideally the skid plane lies in the x-z plane, the lifeboat will then move straight forward down the skid, without any translation in the y- direction. Then if the centre of gravity of the lifeboat lies along the y-axis, there will only be rotation about one axis, the y-axis. This rotation is pitch.

Since the lifeboat is used in emergency cases, the operational conditions will likely be harsh, and an ideal launch situation will be unlikely. When the skid plane moves out of the x-z plane, the skid plane will be skewed seen in the y-z plane. The gravity force pulls on the centre of gravity, leading to rotation in roll and yaw as well as pitch. The skid plane can also be tilted forward and backwards as a consequence of rotational motion of the mother vessel parallel to the x-axis of the skid plane. The result of this can respectively be an increase and decrease in the initial free-falling velocity. The rotation is dependent on the velocity at the end of the skid. If the lifeboat slides slowly over the skid end, the gravity has a large amount of time to pull down the part that has passed the skid end, causing a large rotation. In the case of high sliding velocity, the rotation will be small.

The launching plane is dependent on the motion of the mother vessel, hence the initial conditions in the launching phase is crucial for the further phases.

2.2 Free-falling phase

The free-falling phase starts when the lifeboat no longer has contact with the skid, that is when the normal reaction force from the skid is zero, $F_n = 0$, seen in Figure 2.1. The free-falling phase is affected by the rotation (angular velocity), initial velocity out from the skid, skid plane angle (launching angle), air resistance and wind loads. The free-falling time is dependent on the diving height, that is the freeboard position of launching.

Figure 2.2: Shows a free-falling lifeboat in the free-falling phase. This is a Norsafe AS production, one of the leading lifeboat producers. (Consultance, 2017)

In wave conditions where the launching point on the vessel has a relatively steady global position, the diving height will depend on the phase of the impact wave. It will increase if the lifeboat is launched such that it enters in a through and decrease when entering at a crest. Longer free-falling time leads to a larger effect of the air resistance, wind loads and larger impact velocities. However, the wind loads are not constant trough the free-falling distance. The wind velocity profile is dependent on the atmospheric stability conditions. It is also dependent on the hour of the day and changes between day and night, dawn and dusk. An example of a wind velocity profile from DNV for stable (low temperature lapse rate), neutral (medium temperature lapse rate) and unstable (high temperature lapse rate) atmospheric conditions are shown in Figure 2.3. (DNV-GL, 2010) It should be noted that most lifeboats are installed between 10-30 meter above sea level, hence, the difference regarding the wind velocity for the presented atmospheric condition is small.

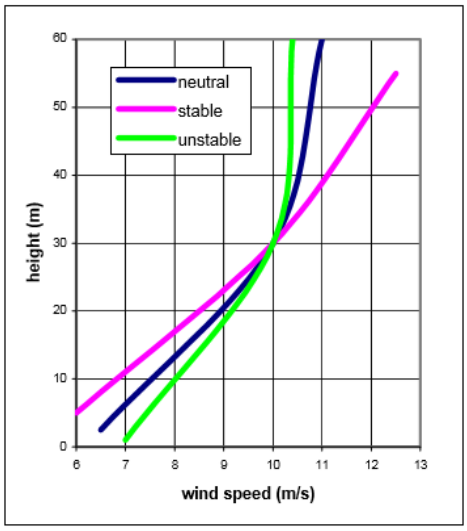

Figure 2.3: Wind conditions (DNV-GL, 2010)

A logarithmic wind velocity profile for neutral atmospheric conditions from DNV-GL is expressed as

$$U_w(z) = U_w(H_w)\left(1 + \frac{ln\left(\frac{z}{H_w}\right)}{ln\left(\frac{H_w}{z_0}\right)}\right) \qquad [1]$$

Where H_w is the height of the mean wind velocity measuring, z is the height at any given point and z_0 is the terrain roughness parameter also known as the roughness length. In open sea with waves, this value is in the range of 0,0001 – 0,01 m.

The effect of the rotation, air resistance and the wind loads are dependent on the diving time. Rotation is measured in rotation angle over time, hence the water entry angle is dependent on launching angle and the rotation given at the end of the skid and free-falling time.

2.3 Water entry phase

The water entry phase starts from initial impact between body and the free surface, and ends when the aft part of the body is below the undisturbed free surface. The launching and free-falling phases sets the initial parameters for the water entry. These parameters are the velocity, water entry angle and angular

velocity in roll pitch and yaw. The typical diving height for a free-falling lifeboat launched at a skid, is between 20 m and 30 m. This will provide an impact velocity of approximately 20 m/s. The skid usually has a value of 35°, and a desirable water entry angle has a value of 50°-60°, hence the angular velocity is providing the water entry angle. As the body enters the water it is subjected to resistance forces in terms of drag, viscosity effects and slamming. The influence of slamming forces is most critical for the water entry phase, due to the transfer of momentum from the lifeboat to the impact fluid.

2.3.1 Slamming

In the water entry phase, the free-falling lifeboat will experience impulse loads with high pressure peaks, propagating from the bow to the stern. This phenomenon is known as slamming. It is a strongly non-linear problem. It is very sensitive of the relative impact velocity, that is the liquid-body velocity, and the dead rise angle, β, which is the angle between the water and the body. The sudden transition from air to water leads to large forces on the body, and can lead to global elastic transient resonance oscillation. The slamming load are the most critical load in the matter of free-falling lifeboats, and govern the design of the local hull structure. In this phase, the pitch rotation will reverse from the free-falling rotation. The rotation is now counter clockwise, when using Figure 2.4 as reference, and causes increased slamming pressure on the aft part of the hull. For oval geometry cases, such as the lifeboat form, it is important that the water entry angle does not become too low. If it does, the slamming forces will increase rapidly due to the large change in added mass.

Some of the physical phenomena connected with slamming is compressibility of water, air cushions/bubbles (for small angle between the body and the water), hydroelasticity, cavitation and ventilation.

2.3.1.1 Simplified calculation approach

There has been performed extensive researching on the field of slamming. Von Karman (1929) and Wagner (1932) had a large impact on the field.

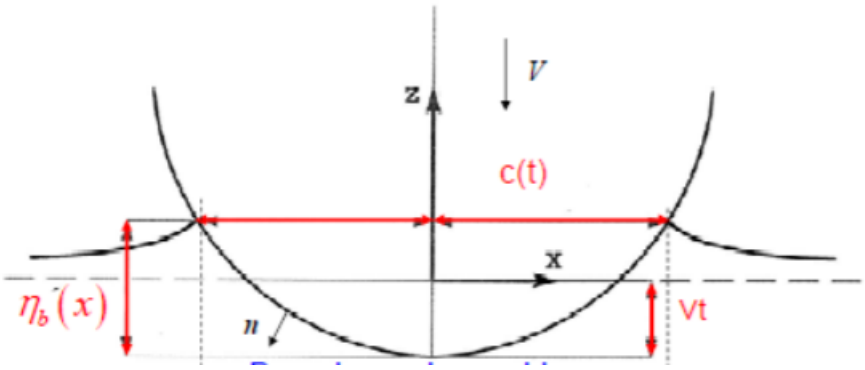

Figure 2.4: Shows how the different parameters are defined in the analysis of impact forces and pressure on a body.

The wetted area is taken to be between $-c(t) \leq x \leq c(t)$, shown in Figure 2.4. Von Karman (1929) developed a method with a simplified approach. The wetted length is taken at the free surface, excluding the up-rise water effect. Wagner (1932) includes this effect and the wetted area is taken at a height $\eta_b(x)$ which is defined as the distance from where the body has its maximum submerged point up to the point of water spray.

The density of water is almost independent of the temperature and pressure (Engineering ToolBox, u.d.), which make the incompressible assumption appropriate. For a frictionless fluid, there will be no shear forces and torque. A frictionless flow without initial fluid rotation, will never start to rotate, and the velocity can be derived by the velocity potential spatial derivatives. Equation [3] - [8], shown below, are only valid for frictionless, stationary and incompressible fluid, meaning that potential theory is applicable.

$$U = \nabla\phi \qquad [2]$$

Then for a simple two-dimensional projectile penetrating the free surface, the force in heave can be written as

$$F_3 = \frac{d}{dt}(VA_{33}) + \rho g \Omega(t) \qquad [3]$$

F_3 is the force in heave, A_{33} is the added mass in heave. The term $\rho g \Omega(t)$ is the time dependent buoyancy force, and is initially zero. The velocity and added mass in heave are time dependent variables, hence equation [3], by utilizing the product rule, can be written as

$$F_3 = A_{33}\frac{dV}{dt} + V\frac{dA_{33}}{dt} + \rho g \Omega(t) \qquad [4]$$

In this case, the pressure can be defined from the Bernoulli equation

$$p = -\rho g z - \rho\frac{\partial \phi(x,z)}{\partial t} - \frac{1}{2}\rho(\nabla\phi)^2 \qquad [5]$$

For the slamming case, by assuming that $z = 0$ at the mean water surface, and neglecting the spatial derivatives of the velocity potential, as they are much smaller than the time derivatives of the velocities potential, equation [5] can be simplified to

$$p = \rho\frac{\partial \phi(x,z)}{\partial t} \qquad [6]$$

The velocity potential on the body can be written as

$$\phi = -V\sqrt{c^2 - x^2}\,, \quad |x| < c(t) \qquad [7]$$

Then by time differentiate the velocity potential, the pressure becomes

$$p = \rho\frac{dV}{dt}\sqrt{c^2 - x^2} + \rho V\frac{c}{\sqrt{c^2 - x^2}}\frac{dc}{dt} \qquad [8]$$

The first term from equation [8], $\rho\frac{dV}{dt}\sqrt{c^2 - x^2}$, represents the added mass pressure and the second term, $\rho V\frac{c}{\sqrt{c^2 - x^2}}\frac{dc}{dt}$, represents the slamming pressure. (Faltinsen, 1990)

For a “real flow”, viscous forces will always be present, resulting in shear stresses and boundary layers, but for large $Re = \frac{uL}{\nu}$, irrotational fluid flow outside the boundary layer is a valid assumption. For the slamming case, it is assumed that the spatial derivatives are negligible compared to the time derivatives. Since the viscous term is multiplied with the spatial derivatives in the Navier–Stokes equation, the inviscid fluid assumption is reasonable for the case of slamming.

2.3.1.2 Slamming calculations for free-falling lifeboats

Calculation of the slamming pressure for free-falling lifeboats is a complex matter. There will be an oblique impact, the body is three-dimensional and waves should be considered. Sauder proposed a method for calculating the slamming phenomena for free-falling lifeboats. The method is developed to predict the trajectory in the six degrees of freedom in waves. In able to do so, three dextral orthogonal coordinate systems are used, and some approximation and assumptions had to be set.

Approximations:

- Three-dimensional formulation of fluid momentum conservation
- Long wave
- A boundary element method for evaluating the added mass matrix

Assumptions:

- The viscosity and the compressibility of the water are neglected
- Potential theory is applied
- The fluid acceleration is assumed to be much larger than the gravity acceleration, hence the high-frequency free surface boundary condition $\phi = 0$ can be used.
- Von Karman approach, local water up-rise is neglected. The pressure in the spray area will be very close to atmospheric pressure. It is the hydrodynamic pressure and forces that are of interest.
- Ventilation, cavitation and hydroelasticity are neglected

(Sauder & Fouques, 2009)

2.3.1.3 Hydroelasticity

In slamming hydroelasticity is relevant for dead rise angles $\beta < 5°$ and when the loading time associated with water entry is small or comparable to the natural wet period of the structure. Hydroelasticity means that the hydrodynamic loads affect the structural elastic vibrations and in return the elastic vibrations affect the fluid flow and related pressure field. When hydroelasticity matters in the slamming problem, the hydrodynamic and structural problems must be solved simultaneously. In extreme cases of flat impacts with hydroelasticity the maximum pressures cannot be used to estimate the structural response. Hydroelasticity is a phenomenon connected with slamming where the dead rise angle $\beta < 5°$. (Greco, 2012)

2.3.2 Parameters defining the water entry

There are several parameters which influence the physics during a water entry problem, resulting in air entraining, super cavitation or maybe no cavity formation at all. Water entry with air cavity formation and air entraining are emphasis on in this thesis.

Air cavity is a result of viscous forces outweighing the surface tension, and the contact line is then pinned to the body surface at the air-water project line. This resulting in air to be entrained behind the body as the air cavity develops. For water impacts, where the fluid velocity is high, a small horizontal jet gets ejected at great radial velocity outwards from the intersection point. For Spheres, Thorodsen et. al (2004) found that this was the case for Re > 9000. (Truscott, et al., 2013)

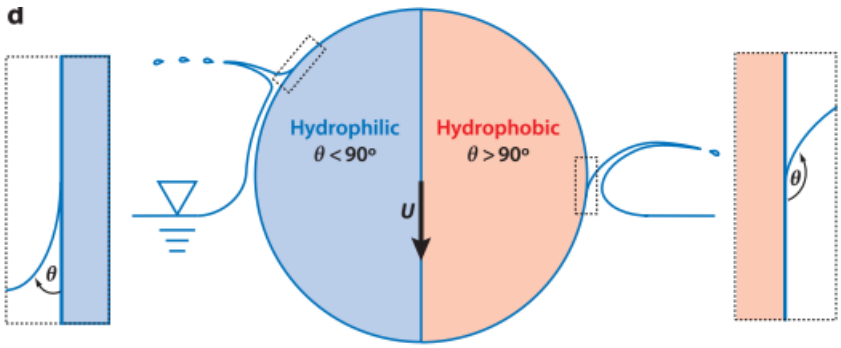

Figure 2.5: Shows the difference in splash crown formation for a hydrophilic and a hydrophobic case (Truscott, et al., 2013)

Important parameters for the entering body are geometry, wettability, density and location of center of mass, and due to variation in geometry, impact conditions and material properties, the water entry phenomenon is very complex and difficult to predict. Wettability is defined with the static contact angle θ_0 shown in Figure 2.5. If this contact angle, θ_0, is below 90 degrees, the water entry is called hydrophilic, while a θ_0 > 90 is called hydrophobic. For an interaction between a body and a given fluid with constant surface tension, less impact velocity is needed for the body at a higher θ_0 to ensure cavity creation.

Impact parameters influencing cavity creation are the impact angle, impact velocity, transverse and longitudinal spin. Truscott, et al. (2013) did experience with billiards ball, where the contact angle varies from one side to another, due to an initial spin counter clockwise. The left-hand side of the sphere experienced a larger dynamic wetting angle, due to an advancing contact angle resulting in a larger outward splash. For the right-hand side, the spin resulted in positive vertical velocity, contributing to a wedge of fluid is drawn across the cavity and inhibits splash growth. (Truscott, et al., 2013)

Important parameters for the opposite fluid is viscosity, density and surface tension. Surface tension is due to the cohesive force between the liquid molecules, with dimension force per unit length. For sea water it has a natural value of $72.8 * 10^{-3}\ N/m$. Truscott did experiments with spheres, only changing the body density ρ_s, showing the dependency of density relation, $\frac{\rho_s}{\rho}$, and cavity closure height divided on total cavity height, $\frac{H_c}{H}$. The experiment showed that $\frac{H_c}{H}$ increased with increasing $\frac{\rho_s}{\rho}$. More about cavity shapes and creation will be included in the submerged phase, section 2.4.

The value of the surface tension may be of importance for how the air cavity forms. Further influencing all the aspects of the behavior of a body, such as acceleration, velocity and trajectory when the body moves from the water entry phase to the submerged phase. For relatively large bodies and velocities, surface tension can be neglected, though it might be of importance near cavity closure. The formation of an air cavity can be predicted by non-dimensional numbers. They are all inverse proportional with the surface tension force γ. A high Capillary number may indicate that an air cavity will form, defined as

$$C_a = \frac{\mu U_0}{\gamma} \qquad [9]$$

Where μU_0 is the viscous force. The Bond number is the ratio between gravitational forces, $\rho g D^2$, and surface tension forces. The air cavity shape is dependent on the ratio between surface tension and inertia forces for a low Bond number, defined as

$$Bo = \frac{\rho g D^2}{\gamma} \quad [10]$$

For low Bond numbers the cavity shape will be dependent on the ratio between inertia forces and surface tension, this is known as the Webber number. The cavity breakup and characterization of the splash crown stability can be predicted by this number, given as

$$We = \frac{\rho U_0^2 D}{\gamma} \quad [11]$$

Where $\rho U_0^2 D$ represents the inertia force. The Froude number characterizes the macroscopic behaviour of the air cavity

$$Fr = \frac{U_0}{\sqrt{gD}} \quad [12]$$

The lifeboat structure is relative large and the water entry velocity is relative high. Additionally, a low surface tension for water, results in very high non-dimensional numbers. Therefore, the surface tension will have little influence in the submerged phase.

2.4 Submerged phase

The submerged phase starts when the aft part passes the free surface, and for this phase, the focus will mainly target the understanding of the cavity evolution of the air cavity behind the free-falling body. The body will experience large hydrostatical pressure on the hull as well as hydrodynamic forces. The translational and rotational velocity and the water entry angle at initial water entry, affects the

trajectory through the water. As mentioned earlier in the water entry phase, there are several parameters influencing the water entry, increasing the complexity of the submerged phase. External forces will also have great effect on the trajectory. These external forces are primarily waves, but also strong current can have an effect. The waves have local phase dependent fluid particle velocity and acceleration properties, as well as wave surface elevation and slope.

2.4.1 Air cavity formation

As the very aft passes the free surface, the corner at the newly created free surface has an initially infinite curvature. The gravitational force tries to flatten out this new surface, dragging the two corners diagonally inwards towards the body-center. The contact point of where the two surfaces collapses will be the point of air cavity closure. At this point a singularity will emerge. This results in a formation of water jets. The water jets move in oppositely directions from the collapse location, one towards the body inside the entrapped air bubble, and the other in the reversed water entry direction. As the two water surfaces collapses, the body will experience an abrupt change in acceleration. The reason for this is that the newly entrapped bubble behind the lifeboat is compressed by the water surrounding it, resulting in that the body will get a positive acceleration contribution in the direction of motion. After the first compression, the entrapped bubble will oscillate due the difference in pressure inside the bubble and the surroundings, while it decreases in size until it gets dissolved.

The formation of an air cavity behind the lifeboat contributes to a stronger retardation. Hence when designing a lifeboat hull, there will be a high focus on minimizing the air cavity by mainly altering the lifeboat-stern geometry. The formation of the air cavity is most pronounced at the aft part of the body. However, there will be appendages and a wheelhouse on a lifeboat, where air cavity also will be present, but in a smaller scale. (DNV-GL, 2016)

2.4.2 Cavity classifications

The creation of air cavity begins in the first few moments after impact, as the fluid is displaced downward and upward, forming a splash curtain.

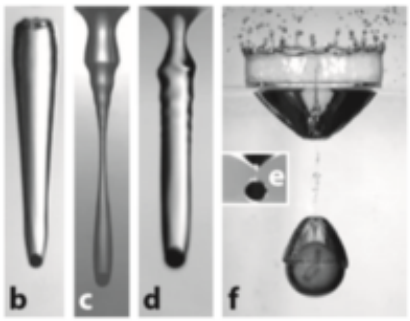

Figure 2.6: Visualization of different water entry events (Truscott, et al., 2013)

Air cavity can be divided into four types of cavity formations after water impact. Surface seal, deep seal, shallow seal and quasi-static seal, Figure 2.6 b, c, d and f, respectively. Surface seal is defined when cavity closure occurs at the free surface, with a long cavity attached beyond the body. Surface seal is often more relevant for higher Froude's Number, while a deep seal, where the pinch off occur closer to the body often is connected with relatively low Froude Number. For shallow seal, the pinch of occurs just below the water surface, like a deep seal, but with a shape more like a surface seal.

The main difference between a shallow and a deep seal is that the pinch of close to the surface in a shallow seal is due to capillary instabilities rather than hydrostatic pressure. The opposite is the case for a deep seal. Quasi-static seal is often in connection with pinch of at the body or close to it. This is common for cases where the body is almost restrained to enter the water due to the large surface tension. Aristoff and Bush (2009) presented low Bond number cases where $10^{-2} < Bo < 10^{3}$ versus Froude numbers of $\sqrt{10^{-0,5}} > Fr < \sqrt{10^{2,5}}$ and stated that only surface and deep seal occurs for $Bo > 10^{3}$. Lee et al. (1997) suggest that deep seal occurs roughly halfway between the surface and a projectile for $\sqrt{20} < Fr < \sqrt{70}$, where transition to surface seal occurred for $Fr > \sqrt{150}$.

In the case of free-falling lifeboats, the surface tension is considerably low. This leads to high Capillary, Bond and Webber number (Equations [9] - [11]), which predicts air cavity formation in form of deep seal corresponding with Froude number range for lifeboats.

2.4.3 Physical insight

The study regarding the dynamics of water impact and air cavities was intensified during the world war because of the needed design of military projectile entering water in high speed. Therefore, most of these early experiments were conducted with a high Froude Number, resulting in relative unimportant gravity effects. In recent years, scientific interest and practical importance have led to an increase of studies with relatively low Froude number, where gravity effects are comparable to inertia forces.

To better understand the physics in the submerged phase, it is important with a basic knowledge of the cavity development and evolution, regarding both assumptions and simplifications made for the varies derivations. Experiments is often conducted with high Reynolds number to ensure more accurate cavity parameter calculations when potential theory is applied. This is due to the small influence of the viscous forces. Not only experiments have been conducted regarding water entry dynamics, but also theoretical and numerical studies have been performed.

Birkhoff and Zaranthello (1957) and Lee, Longoria and Wilson (1997) used a two-dimensional analytic model to study the air cavity dynamics. In a two-dimensional potential flow, air cavity cannot be created, and to account for the three-dimensional flow effects, they had to introduce an arbitrary constant to make the kinetic energy finite. This arbitrary constant was further determined by fitting the theoretical prediction with experimental data and/or nonlinear numerical simulations. A thorough explanation of a specific derivation regarding the air cavity dynamics will be included in the compressible part for this thesis. (Yan, et al., 2009)

A simple derivation of how the cavity closure is dependent of the Froude number, can be obtained by dividing the water entry of a body and the following air cavity into two main phases. Assuming a relative low Fr>10 and a constant vertical velocity, the vertical position of the bow, z_b, after impact can be defined as $z_b = \mathrm{Vt}$, if $t = 0$ at initial impact. At some height, z_0, the creation of the cavity begins, with an initial radius $r(z_0, t_0) \approx R$, where R is the body radius assuming an axisymmetric body. As the body continuous to descend below z_0 ($t > t_0(z_0)$), the cavity expands, $\frac{\partial \mathrm{r}}{\partial \mathrm{t}} > 0$, for some time. When the cavity has reached the maximum radius, the expansion time $\delta t_1(z_0)$ is over, and the radius will decrease, eventually resulting in collapsing of the air cavity. Generally speaking, there is a height H_c, where the cavity first closes at $t = T$, and $r(H_c, T) = 0$. Initial air cavity closure can occur above the free surface, referred to as surface closure, or below the free surface, often referred to as deep closure or

pinch of. Cavity closure is dependent on Froude number, where deep closure usually occurs for relatively low Froude numbers, while surface closure is more common for larger Froude numbers, discussed in section 0. Regarding the contraction phase, a basic estimate of closure time at any height z_o can be obtained by assuming steady state, with a constant radial velocity derived from Bernoulli equation,

$$-\frac{\partial r}{\partial t} = u(z_o) = (2gz_0)\text{^}0{,}5 \text{ for } t > t_o + \delta t_1 \qquad [13]$$

The time of collapse is $t_c(z_0) = t_0 + \delta t_1 + \delta t_2$, where δt_2 is equal to the collapsing phase time, and can be estimated as $\delta t_2(z_o) \cong R/u(z_o)$, by assuming that the maximum cavity radius is equal to the body radius. For many body shapes, like long vertical cylinders, the expansion phase is short compared to the collapsing phase, and can be neglected. Resulting in closure time defined as: $T = min_{z0}\,[t_0(z_0) + \delta t_2(z_0)]$ and substituting δt_2 in terms of z_o, a relation between Froude number and closure time can be found

$$\frac{TV}{D} \approx \left(\frac{3}{2^{5/3}}\right) Fr^{2/3} \qquad [14]$$

At pinch of position $z = H_c$, assuming that the total cavity height $H = TV$ at pinch of, is equal to $3H_c$. According to Duclas, et al. (2007), this relation, even though with many simplifications, will show good agreement with reality in the case of relatively long vertical cylinders. More detailed derivation of the equation above can be found in Mann (2005) and Mann, et al. (2007). (Yan, et al., 2009)

2.4.4 Capillary waves evolution in the air cavity water surface

As the two surfaces collapses together at the air cavity closure, it will result in a shock, leading to air, water jet and capillary waves moving towards the body along the free surface of the air cavity. The shock creates a wave packet containing wave of different frequencies, the waves spread with the velocity $c = \omega/k$, given by the dispersion relation $\omega^2 = \left(\frac{\gamma}{\rho}\right) k^3$, where plane capillary waves are assumed. γ is the surface tension and k is the wave vector. (Gekle, et al., 2008)

2.5 Water exit phase

An important parameter for the water exit for a body breaching the water surface, is the pop up height, h_p. It is defined as the height from the body center, to the undisturbed free surface. Pop-up height is of interest for all applications where objects breach the surface. For example, an emperor penguin breaches the surface to escape from predators. They release bubbles from their feather during ascent to reduce drag forces, resulting in an increased water exit velocity. In the case of a free-falling lifeboat, water exit speed is beneficial for a longer sail away distance.

The pop-up height depends on the free surface exit speed, which is dependent on the under-water trajectory and dynamics during surface breach. Vortex shedding is dependent on the release depth, and will in addition influence the trajectory and speed of the body. During ascent, vortices will shed differently, depending on the Reynolds number. This leads to three underwater trajectory regimes, often referred to as vertical, oblique, and oscillatory. This is demonstrated in Figure 2.7.

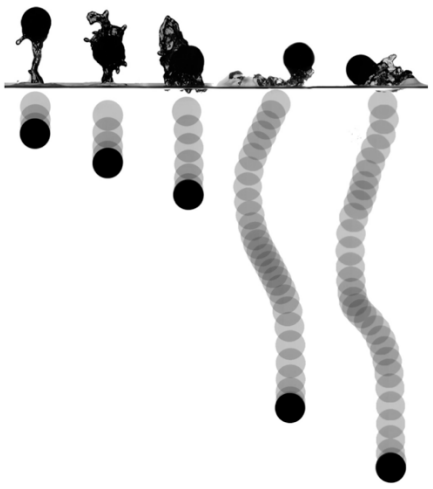

Figure 2.7: Trajectory dependent on released depth for ping-pong balls (Truscott, et al., 2016)

Depending on the Webber number (equation [11]) and the Froude number (equation [12]), during water exit in addition to the structure of the vortex shed near the water surface, the resulting splash plume and cavity will take on various forms. This indicates varying amounts of energy transferred to the fluid during water exit. A rough estimate of h_p can be derived from the mechanical energy considering

the body at breach, assuming constant mass. The added mass will actually vary as the body breaches the surface, making the problem more complex

$$\frac{V_1^2}{2} + gh_1 = \frac{V_2^2}{2} + gh_2 \qquad [15]$$

Where $h_1 = h_p$, V_1 is the vertical velocity equal to zero at maximum h_p. V_2 is the vertical velocity at surface breach and h_2 is the height of the body center at water surface, equal to zero. When assuming zero net hydrodynamic forces acting on the body during breach, neglecting the work done by buoyancy and dynamic pressure forces and ignoring the energy lost when the body breaches the surface, resulting in splash and wave production, equation [15] can be simplified to

$$gh_p = \frac{V_2^2}{2} \qquad [16]$$

this yields

$$\frac{h_p}{D} = \frac{V_2^2}{2Dg} = \frac{1}{2} * Fn_b^2 \qquad [17]$$

Seen from formula [17], the pop-up height depends on the vertical free surface exit speed as mentioned above. An increased depth of release does not have to result in higher pop-up due to the fact that the water exit velocity do not correlate with an increasing function of the release depth. For a more reliable derivation of the exit speed, where the force balance is modeled for a sphere by setting the net vertical acceleration equal to zero, see Truscott, et.al. (2016), equation 4.

Depending on the pop-up height, slamming can also occur after the water exit phase, referred to as second slamming. In the cases of second slamming, the lifeboat can have a water entry angle close to zero degrees. This angle provides the maximum slamming forces at for a given velocity. Since the slamming force is proportional with square of the velocity, and the velocity at second water entry is significantly lower, slamming forces for the first water entry is of main interest. (Truscott, et al., 2016)

2.6 Sail away phase

The main objective in the sail away phase is to get away from hazardous events. The ability to sail away from the evacuation scene is crucial and all the other phases will affect this phase. Here, the functionality of the lifeboat is described as a sailing vessel, that is resistance, maneuverability and stability. As the conditions are most likely to be challenging, the sail away performance must be of high standard, where the forward distance performance depends on the lifeboat initial motion right after resurfacing, which will be affected by waves. (Jin, et al., 2014)

2.7 Motion patterns

DNV-GL has identified four different main motion patterns for free falling lifeboat launches in calm water.

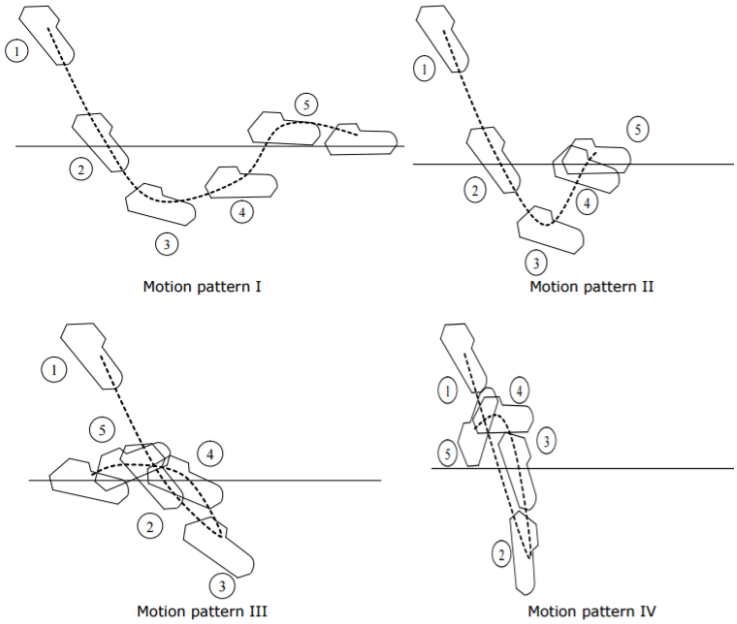

Figure 2.8: Motion patterns for a free-falling lifeboat

Where motion pattern 1, in Figure 2.8, is when the lifeboat pitches significantly at maximum submergence and ascent so that it surfaces with a positive forward velocity. Motion pattern 2, in Figure 2.8, is the same, but the forward velocity is reduced to zero and it surfaces with a negative (backward)

velocity. Motion pattern 3 and 4, in Figure 2.8, is when the lifeboat moves backwards after reaching maximum depth in water, these two motions are often referred to as *log dive*, and should be avoided. (DNV-GL, 2016)

2.7.1 Log dive

Log dive is an unwanted water exit path where the body exits with aft part first. This can occur if the water entry angle is too large. Launching problems, wind loads and entry in a through can lead to an increased water entry angle. Also, the air cavity formation should stay intact in order to have the strong drag force, pulling on the lifeboat back into the entry trajectory, reversing the path. One criteria for log dive to occur is if the maximum negative longitudinal velocity in the ascent phase accommodate the following criteria

$$v_{x'} < -\sqrt{2g * VCG} \qquad [18]$$

$v_{x'}$ is the velocity in the body fixed x-direction, VCG is the vertical position of the center of gravity.

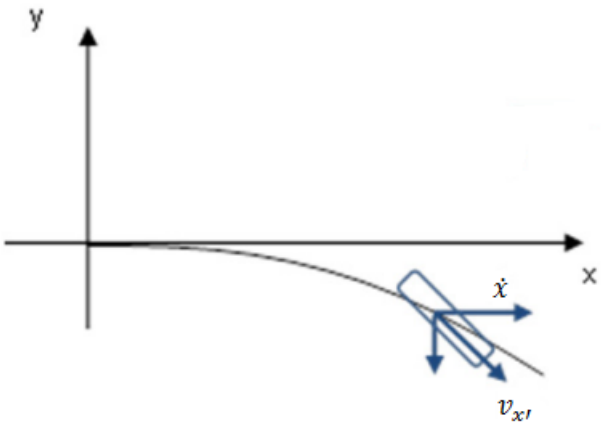

Figure 2.9: $\dot{x}$ is the horizontal velocity of the lifeboat and $v_{x'}$ is the sum of the horizontal and the vertical velocity components in the direction of motion. (DNV-GL, 2016)

2.8 Occupant safety

Accelerations induced on the lifeboat is important regarding the safety and comfort for the occupants. To ensure that the passengers does not get harmed by the induced acceleration, the lifeboat designer has to focus on complex combination of various relations like for example body sizes and seating.

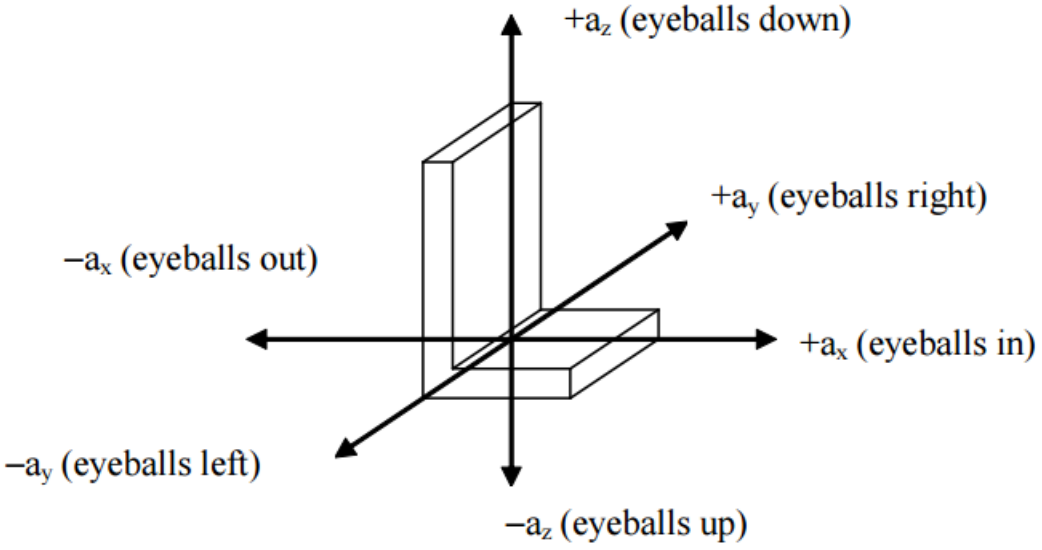

Figure 2.10: The local seat coordinate system (DNV-GL, 2016)

The basis for quantifying the acceleration induced loads on the human body in a free-fall lifeboat dive consist of acceleration components in the relevant directions. See Figure 2.10 for description of acceleration components a_x, a_y and a_z. An accepted criterion for occupant acceleration, is the Combined Acceleration Ratio (CAR), which is defined as

$$CAR = \max \sqrt{\left(\frac{a_x}{18g}\right)^2 + \left(\frac{a_y}{7g}\right)^2 + \left(\frac{a_z}{7g}\right)^2} \qquad [19]$$

18g, 7g and 7g is the normalization constants for the accelerations a_x, a_y and a_z, respectively.

- CAR_1 for out of seat acceleration – positive a_x values in the times series only.
- CAR_2 for into seat accelerations – negative a_x values in the times series only.

For into the seat acceleration it is recommended that the normalization constant a_x is reduced with 50% from 18g to 9g. A CAR value of less than one is defined as safe.

When interpreting the CAR index the acceleration data from the time series is to be filtered with a minimum 20Hz low-pass filter. A Butterworth fourth-order filter is to be used for filtering of the acceleration data, where the frequency domain transfer function, |H(f)|, is described as

$$|H(f)|^2 = \frac{1}{1 + \left(\frac{f}{20}\right)^4} \qquad [20]$$

where f is an arbitrary frequency (1/s). (DNV-GL, 2016)

3 Computational fluid dynamics

Computational fluid dynamics (CFD) is a branch of fluid mechanics that uses numerical analysis and algorithms to solve and analyze problems that involve fluid flows. CFD uses computers to perform the calculations required to simulate the interaction between the body and the fluid defined by the boundary conditions.

In a CFD process there are 5 to 6 main interconnected steps; 1) Geometry definition, 2) Surface grid generation, 3) Volume grid generation, 4) Flow calculation, 5) Data reduction, and 6) Experimental validation, if it can be provided. Then the software creates a second mesh, but now representing the volume occupied by the fluid, this is done to determine the behavior of the particles. After the meshes are finish, the software will set up a clear image on how the fluid will come in contact with the initial surface or object, while also emphasizing the exact problems encountered by it in the process. The software works to solve the Navier-Stokes problem, and afterwards the post-processing begins. It is assumed that the governing equations are valid. By applying the mass conservation equation and the momentum equation, four equation emerges and the pressure and the velocities in the three dimensions can be calculated. The results from CFD simulations are generally validated with previous experiments. (J. Andreson, 2009)

3.1 Governing equations in CFD

CFD calculations is based on solving the Navier-Stokes problem for four equations and four unknowns. The first of two equation that govern the fluid mechanics, is the conservation of mass. It described the balance of mass through a control volume. The equation for this is called the continuity equation and can be expressed as:

$$\frac{\partial \rho}{\partial t} + \frac{\partial}{\partial x_j}(\rho u_j) = 0 \qquad [21]$$

Where u_j is the velocity vector in all three directions, and the operator $\frac{\partial}{\partial x_j}$ is the respectively derivatives. It implies that the mass cannot be created or destroyed in a flow field. Hence, if there is a change in density there must be a change in the volume. It must be compressed or stretched in at least one direction, in order to conserve the mass in the control volume.

The other three equations can be expressed from

$$\frac{\rho D u_i}{Dt} = \frac{\partial \sigma_{ij}}{\partial x_{ij}} + \rho f_i \qquad [\,22\,]$$

This is the basic conservation law for momentum in fluid mechanics and is valid for every relation between deformation rates and viscous stress. The stress tensor vector can be written as

$$\sigma_{ij} = -p\delta_{ij} + \sigma' \qquad [\,23\,]$$

where the viscous stress tensor for Newtonian fluid, defined as “The resistance which arises from the lack of lubricity in the parts of fluid, other things being equal, is proportional to the velocity by which the part of the fluid are being separated from each other” (White, 2006) have the relation:

$$\sigma' = (\frac{\partial u_i}{\partial x_j} + \frac{\partial u_j}{\partial x_i} - \frac{2}{3} * \delta'_{ij} * \frac{\partial u_k}{\partial x_k}) \qquad [\,24\,]$$

δ'_{ij} is the two variables function, called the Kronecker delta. Its value is an integer, and equal to one if the velocity component changes in its defined direction, and zero if not, shown in equation [25].

$$\delta_{ij} = \begin{cases} 0 & if\ i \neq j \\ 1 & if\ i = j \end{cases} \qquad [\,25\,]$$

By inserting equation [24] into equation [23] and then into equation [22], the famous Navier-Stokes equation appears:

$$\rho \frac{Du_i}{Dt} = -\frac{\partial p}{\partial x_i} + \frac{\partial}{\partial x_j}\left[\mu\left(\frac{\partial u_i}{\partial x_i} + \frac{\partial u_j}{\partial x_j} - \frac{2}{3}\delta_{ij}\frac{\partial u_k}{\partial x_k}\right)\right] + \rho f_i \qquad [\,26\,]$$

In the case of constant fluid density, which is assumed in most CFD calculation for free fall lifeboats equation [26] can be reduced to:

$$\rho \frac{Du_i}{Dt} = -\frac{\partial p}{\partial x_i} + \mu \nabla^2 u_i + \rho f_i \qquad [\,27\,]$$

(Ytrehus, u.d.) (White, 2006) (J. Andreson, 2009)

3.2 Previous work with the use of CFD for free-falling lifeboats analysis

Since free falling lifeboats mainly operates at sea, experimental results for typical north-sea waves is hard to come by. Here CFD is a valuable resource for calculating forces, accelerations, path and other parameters and features.

3.2.1 Validation of CFD with experiments

Tregde (2015) ran CFD simulations of a free-falling lifeboat which started 0.5m above water level, and with initial conditions received from previous CFD simulations. The trajectory of the lifeboat is assumed to be governed by the Reynolds averaged Navier-Stokes equations in which turbulence effects are included. In the simulations some simplifications were made, such as;

- Water is assumed to be incompressible
- The lifeboat geometry is somewhat simplified to ease the meshing
- The lifeboat is assumed to be a rigid body, hydroelastic effects are not taken in account
- Air is assumed to be either incompressible or compressible with ideal gas relation
- Implicit 1st order time scheme has been used.

The simulations were compared with experimental results, where the compressible CFD simulations compared with the full scale experimental data showed good correlation for pressure on the top of canopy, figure 7 and 8 in the paper.

Tregde concludes that incompressible flow simulations would give reliable results for motions, accelerations and most pressures, except in the aft sections of the vessel, where the compressed air bubble makes a big difference. (Tregde, 2015)

3.2.2 Free-falling lifeboats in waves

Berchiche, et al. (2015) ran 12 cases for a free falling-lifeboat in waves with CFD simulations, were the waves had different headings and hit point locations, seen in table 2 in the paper. It should be noted that the simulations were done with laminar flow, with Reynolds-Averaged Navier-Stokes (RANS) and an implicit unsteady model with second order time scheme. Also there it was concluded that the CFD simulations were able to predict the motions, accelerations and pressures of the lifeboat during water entry into waves of various directions. Similar as Tregde (2015), Berchiche, et al. (2015), also states that for the local pressures at places where air-cavities are formed and then collapse, such as the aft wall of the lifeboat, it is necessary to model the air as compressible. (Berchiche, et al., 2015)

3.2.3 Sail away phase

The work is done by Jin, et al., (2014). The forward distance performance of a free-falling lifeboat after water exit is addressed. A numerical study with irregular sea state under constant wind and current velocities has been used. Three weather directions, two autopilot settings and different initial motion conditions of the lifeboat are considered in the simulations. The waves are modeled using the JONSWAP spectrum, where the waves have no directional spreading and the wave forces included are of first-order. The current and the wind has a constant velocity. The current forces are implemented by superposing the current velocities onto the local forward and transverse velocities onto the local forward and transverse velocities through the sea. The sea state is represented in table 2 in the paper. Within this weather data the directions considered was: head sea, bow quartering sea and beam sea.

The two autopilot system headings were set to against the weather and the other is along the launch direction. They are represented in table 3 in the paper.

The results obtained from the simulations, shows that the forward distance performance depends on the lifeboat initial motion right after resurfacing of the forward distance simulation. Positive initial surge velocity and small initial yaw angle gives better forward distance performance compared to those with negative surge velocity and large yaw angle. When the desired heading is set to along launch direction, the forward distance is observed best in beam sea condition, and the transverse motion is observed smallest in head sea condition. For the bow quartering and beam sea the transverse motion is quite similar. With positive surge velocity and negative initial yaw angle, the lifeboat is able to turn straight against weather without drifting sidewise. Some important aspects have been identified in the paper, such as that the lifeboat can be pushed backwards before gaining forward distance in some cases, and that the drift motion can be difficult to avoid in bow quartering and beam seas. (Jin, et al., 2014)

3.3 Star-CCM+

Berichiche, et al. (2015) and Tregde (2015) used the software Star-CCM+ when simulating with CFD and free-falling lifeboats, therefore Star-CCM+ is a reasonably choice of software. The software is developed by CD-Adapco and features step-by-step tutorials to minimize the steep learning curve of the software.

3.3.1 Physics

To get the most realistic results from the CFD simulations, the physics are carefully selected. This involves volume discretization, turbulence models, interface capturing, wall Y^+equations, Courant number validation and boundary conditions. Star-CCM+ is a leading software in the matter of CFD analysis, it is a commercial code, and later theories are related to this software.

3.3.1.1 Transport equation

Star-CCM+ uses the governing equation in fluid mechanics and transforms it in to a set of algebraic equations. For this transformation, the equations have to be discretized in space and time. Then the

resulting linear equations are solved by an algebraic multigrid solver. A closed set of equations are obtained after introducing an appropriate constitutive relation into the conservation equation. The integral form of the transport equation, equation [28], is obtained by integrating the generic transportation problem over the control volume and applying Gauss divergence theorem:

$$\frac{d}{dt}\int_V \rho\phi dV + \int_A \rho \boldsymbol{v}\phi \cdot d\boldsymbol{a} = \int_A \Gamma\nabla\phi d\boldsymbol{a} + \int_V S_\phi dV \qquad [28]$$

Where the first term is the transient term, the second term is the convective flux, the third term is the diffusive flux and the fourth term is the source term. V is the control volume ϕ is the transport of a scalar property, $\boldsymbol{A}$ is the surface area of the control volume and $d\boldsymbol{a}$ represents the surface vector, Γ is the diffusion vector and S_ϕ is the source term.

3.3.1.1.1 Segregated flow solver

To solve the integral conservation equation of mass and momentum in a sequential manner, the segregated flow solver can be used. Then by iteration process the non-linear governing equation are solved for the solution variables, that is the velocities and the pressure. A pressure correction equation is solved to fulfil the mass conservation constraints on the velocity field used in the employed pressure-velocity coupling algorithm. The momentum equation and the continuity equation is used for the construction of the pressure correction equation. Then the predicted velocity field fulfils the continuity equation, this is achieved when correcting the pressure. The pressure correction equation also obtains the pressure as a variable.

3.3.1.2 Turbulence model

In Star-CCM+, there are currently four major classes of Reynolds-Average Navier-Stokes (RANS) turbulence models, which are time averaged equation of motion for fluid flow.
To obtain RANS equation, the Navier-Stokes equations for the instantaneous velocity and pressure field are decomposed into a mean value and a fluctuating component. “The averaging process may be though of as time averaging for steady state situations and ensemble averaging for repeatable transient situations.” (Steve CD adapco, 2016)

3.3.1.2.1 Spalart –Allmares

It is applicable for cases where the boundary layers are largely attached and separation is mild if it occurs. It is often used in connection with aerospace external flow applications, like flow over a wing. This turbulence model is not suited for flows dominated by free share stress layer in connection with complex recirculation. Therefore, this turbulence model is not of interest, due to separation on the aft part of the lifeboat. (Steve CD adapco, 2016)

3.3.1.2.2 K-Epsilon model

The K-Epsilon turbulence model is a two-equation model that determines the turbulent viscosity. This is done by solving the transport equations for the turbulence kinetic energy $\boldsymbol{k}$ and its dissipation rate ϵ. According to Star-CCM+, this turbulence model provides a good comparison between robustness, computational cost and accuracy. Unlike the Spalart–Allmares model, K-Epsilon are suited for complex recirculation, with and without heat transfer. (Steve CD adapco, 2016)

3.3.1.2.3 K-Omega model

The K-Omega model and K-epsilon both solve two transport equations. The main difference is the choice of the second transported turbulence variable. The K-Omega model has improved performance for boundary layer under adverse pressure gradients, compared to the K-Epsilon model. This is perhaps the most significant advantage for the K-Omega model. In the K-Omega model original form, the largest disadvantage is that the boundary layer computations are very sensitive of the specific dissipation rate (ω) in the free stream. This leads to extreme sensitivity in the inlet boundary conditions for internal flows. This problem is not present for the K-Epsilon model. (Steve CD adapco, 2016)

3.3.1.2.4 Reynolds stress transported model

According to Star-CCM+, it is the most complex and computationally expensive models offered. It is best suited for situations where the turbulence is strongly anisotropic. This is highly relevant for the swirling flow in a cyclone separator (Cyclonic separation is a method of removing particulates from an air, gas or liquid stream). (Steve CD adapco, 2016)

3.3.2 Free boundaries approximations

For fluid dynamics, both Langrangian and Eularian coordinates are commonly considered. The Langrangian coordinate system is following the fluid particle at each point, and then the fluid properties are determined as the fluid particle is moving. The Eulerian coordinate system is just observing the fluid properties as a function of time and space. Lagrangian coordinates are most common to use as basis for numerical solution algorithms in connection with structural dynamics. Eularian coordinates are often used since the free boundaries undergo such large deformations that Lagrangian methods cannot be applied. Free boundaries are often referred to as surfaces where discontinuities exist in one or more variable. Shock waves and interfaces between fluid and deformable structures are example of free boundaries. The problems related to numerical treatment of free boundaries can be divided into three; their discrete representation, evolution in time and the way boundary conditions are imposed on the free boundaries. (Hirt & Nichols, 1979)

3.3.2.1 Volume of fluid method

There are varies ways to approximate free boundary in finite numerical simulations, but the most common method is based on the concept of a fractional Volume Of Fluid (VOF). This method defines a function F. Its value is of unity if the point of interest is fully occupied with fluid, and otherwise zero. For a distinctive cell, represented by several points, the average value of F will then represent the volume fraction of the cell occupied by the fluid. A cell that only contains fluid will have the value of unity, while a zero value represent no fluid. Hence, if F has a value greater than zero and smaller than one, it implies that the cell must contain a free surface. The VOF method solves the transport equation for the volume fraction F of the occupied liquid in each cell in the grid (see equation [29]). Only one value for the fractional volume is required for each cell, where the fractional volume at the current time step in each cell is located using the velocity field and fractional volume at the previous timestep. This method is time efficient and beneficial due to the fact that it only requires one storage word for each cell. In addition to identify the cells with boundaries, it is important to know where the fluid is located at the boundary. This is predicted only by the scalar fractional volume value and the filling state of the cells sharing a common side, which is considered as the methods main draw back.

$$\frac{\partial F}{\partial t} + u * \frac{\partial F}{\partial x} + v * \frac{\partial F}{\partial y} = 0 \qquad [\ 29\ ]$$

Equation [29] is an example of the derivations of the transport equation for two-dimensional cases, where F moves with the fluid. This can readily be extended to three dimensional calculations.

When both the value of F and the direction of the boundaries are known, a line separating the cell can be constructed to represent the interface, which further can be used when setting the boundary conditions. For cases related to surfaces where the fluids do not remain fixed, but have relative motion in addition, the equation above must be modified. Handling of boundaries between single face and two face fluid regions and shockwaves are examples for when the equation must be modified. (Hirt & Nichols, 1979) (Faltinsen & Timokha, 2009)

3.3.3 Wall Y^+

The non-dimensional wall distance, Y^+, for a wall bounded flow is given as

$$Y^+ = \frac{y u_\tau}{\nu} \qquad [\ 30\ ]$$

u_τ is the frictional velocity at the body, y is half the cell height closest to the body and ν is the local kinematic viscosity (m^2/s) of the fluid. It is commonly used for boundary layer theory and the non-dimensional velocity u^+ is given as

$$u^+ = \frac{u}{u_\tau} \qquad [\ 31\ ]$$

Where $u_\tau = \sqrt{\frac{\tau_W}{\rho}}$ and τ_W is the shear stress.

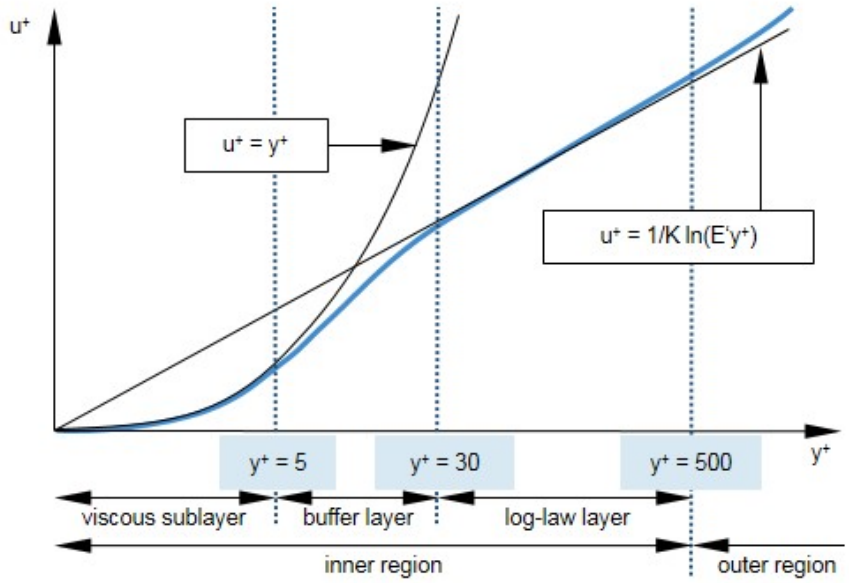

Figure 3.1: Correlation between Y^+ and u^+ (Steve CD adapco, 2016)

The logarithmic layer from Figure 3.1 can be described as:

$$u^+ = \frac{1}{\kappa}\ln\left(E' y^+\right) \qquad [\,32\,]$$

Where κ is the von Karman's constant, approximately equal to 0,42. $E' = \frac{E}{f}$ where E is a coefficient equal to 5,1 and f is the roughness form function. Figure 3.1 shows that u^+ follows the relation of Equation [32] after as Y^+ passes the value of approximately 30. (J. Andreson, 2009) (Steve CD adapco, 2016)

Regarding the wall treatment, three different settings can be chosen in Star-CCM+, this depends on the value of Y^+. If the value is in the viscous sublayer, that is $Y^+ < 5$, the" low Y^+" setting should be used. Often utilized when:

- The accurate prediction of the boundary layer velocity and/or temperature profile is important.
- Simulation time and therefore cell count is not a critical issue.

If the value is in the "log-law layer", that is $Y^+ > 30$, the "high Y^+ should be used. Beneficial to utilize when:

- The wall roughness effect must be included.
- Simulation time and cell count is of critical issue.

A third setting is the "all Y^+". It is a hybrid treatment that uses both the low and high Y^+ treatment. For the buffer layer $1 < Y^+ < 30$ it uses a blending function and gives reasonable solutions for low values in the buffer layer. It is beneficial to choose this setting when Y^+ is varying due to varying geometry and velocity scale associated with the model. (Steve CD adapco, 2016)

3.3.4 Courant Friedrichs Lewy Number

The formula for the dimensionless CFL (Courant Friedrichs Lewy) number is given as:

$$CFL = \frac{u\Delta \mathrm{t}}{\Delta x} \qquad [33]$$

It gives an indication of the ratio between the simulated fluid distance for a given time step, Δt, and the length of one cell, Δx. For every time step, Δt, the Navier-Stokes equations are solved by the iteration process. If the CFL number has a value smaller than one, it implies that there will be at least one solution for each cell. For a moving mesh, such as overset meshes, u is defined as the velocity relative to the mesh in Star-CCM+. Small CFL are advantageous for the quality of the solution, but as a compromise for the computational calculation time, some increase must be tolerated. (Steve CD adapco, 2016)

The CFL number is of interest where the body intersect with the surrounding fluid. Due to the change in density across the cell in a free surface, a low time step is important to ensure robustness for the interface capturing of the free surface. This can be showed by a simplified momentum equation for incompressible, isothermal and immiscible fluids, where the flow does not have pressure and velocity gradients. The momentum equation then reduces to

$$\frac{\partial u_i \rho}{\partial t} = -\nabla \rho u_i u_i \qquad [34]$$

Seen from equation [34], a change in density across the cell will lead to change in the acceleration. Large difference in the density within a cell combined with a time step too “coarse” can therefore lead to unrealistic large accelerations. The fluid will in addition accelerate when it passes sharp corners. Hence, numerical instabilities are most pronounced when sudden changes in geometry (like sharp corners) intersect with the free surface. (Kim & Park, 2016)

3.4 High Performance Computers

With the use of CFD calculations the need of processing power increases with the amount of cells in the simulation. Here high performance computers (HPC) will be valuable. With the use of these computers, more accurate simulations is possible, and the time before the results is available for the user decreases.

Vilje is NTNU's HPC and has 1404 nodes with two hyperthreaded eight-core processors per node of the type Intel Xeon E5-2670 ('Sandy Bridge'), which results in a total of 22 464 cores. There are 32GB RAM attached to each node. (NTNU HPC Group, 2016) As the simulation goes downwards in mesh size and time step, more CPU power is required. Vilje is que based where the job is submitted with a wall time and a number of processors that shall be used, an advice from Andrea Califano was that the simulations should at least have one processor per 30 000 cells. Which was extended to roughly 40 000 cells per processor to reduce que time at Vilje.

By using Vilje, one encountered limitation was the mesh operation, since this operation had to be done beforehand. For this operation, an Asus Zenbook U500V with Intel® Core™ i7-3612QM processor and 10 GB RAM was used. Star-CCM+ recommended approximately 1 GB RAM per 500 000 cells for this study’s mesh configurations, which results in a maximum of 20 000 000 cells in the simulations. (Steve CD adapco, 2016)

4 Pre-Processing

In order to establish the accurate solutions for the simulations, a geometry, mesh configurations, boundary conditions and physics has to be interpreted into Star CCM+.

4.1 Geometry

For the simulations of a free-falling lifeboat, a simplified geometry was chosen. The reason for the simplification is to not complicate the process with appendages such as a wheelhouse. Still, the essence of the behavior of the body will be similar to an actual lifeboat. This gives valuable training in simulating free fall lifeboat diving. The geometry chosen is therefore an ellipsoid, Figure 4.1, with specifications in Table 4.1.

Figure 4.1: Simplified geometry

PARAMETERS	VALUES	DIMENSIONS
LENGTH	10	m
DIAMETER	3	m
MASS	23561.9	kg
VOLUME	47.1	m^3
I_X	21205.8	$kg*m^2$
I_Y	481841.8	$kg*m^2$
I_Z	481841.8	$kg*m^2$
I_{XX}	21205.8	$kg*m^2$
I_{YY}	150501.9	$kg*m^2$

I_{ZZ}	150501.9	kg*m^2
R_{XX}	0.949	m
R_{YY}	2.527	m
R_{ZZ}	2.527	m
COG_X	3.75	m
COG_Z	-0.5	m

Table 4.1: Simplified geometry properties taken from the body fixed coordinate system

a) b)

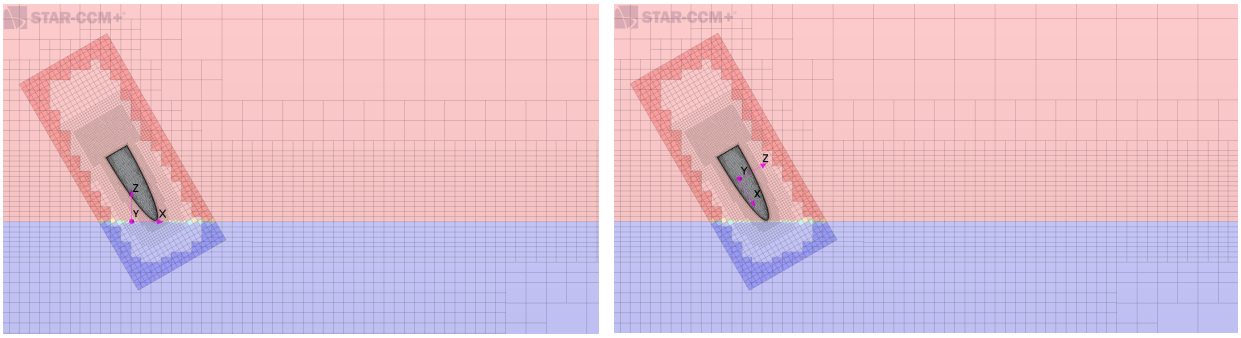

Figure 4.2: Visualization of the coordinate systems, a) is the global coordinate system and b) is the body fixed

Figure 4.2 a) shows the global coordinate system where the origin is located at [0, 0, 0] at all times in the simulations and it is referred to as COG_{global}. The body-fixed coordinate system shown Figure 4.2 b), will be located in the body centre of gravity, and will follow the motion of the body. The different coordinate systems will be referred to as n_{global} for the global coordinate system and n_{body} for the body fixed, where n = x, y or z.

4.2 Boundary conditions

In order to get results that matches a realistic solution, the boundary conditions applied to the different regions in the CFD simulation must be defined. These conditions define the inputs of the simulation model. Whether the fluid flows around or through the body in question, or if the fluid enters or leaves the domain. Hence the boundary conditions connect the simulation model with its surroundings.

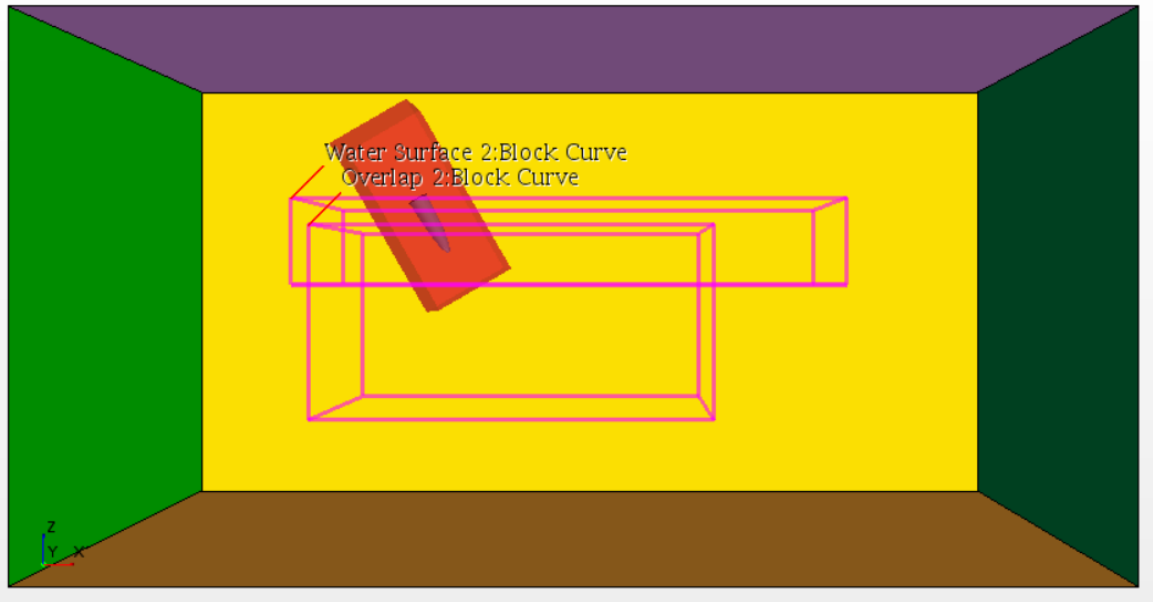

Figure 4.3: Boundary conditions illustration

Figure 4.3 shows the domain chosen for this study. Bright green is labelled as “inlet”, green as “outlet”, purple as “top”, brown as “bottom”, yellow as “port”, red as “overset”, and the transparent as “starboard”. In Figure 4.3, two additional areas are highlighted. The upper one is the “water surface” and the lower one the “overlap”. Their different dimensions are found in Table 4.2

PART NAME	**CORNER 1 DIMENSION** (x, y, z) $[m, m, m]$	**CORNER 2 DIMENSION** (x, y, z) $[m, m, m]$	**CELL SIZE IN 0,08m MESH** $[m]$
BOUNDARIES	-50, -40, -45	100, 40, 32	5.12
OVERLAP	-15, -20, -25	45, 20, 4	0.64
WATER SURFACE	-18, -18, 8	65, 18, -5	0.64, 0.64, 0.32
OVERLAP OVERSET	-18, -11, -11	10, 8, 8	0.64
OVERSET	-17.5, -7, -7	13.25, 7, 7	0.32
BOX BEHIND	-8.5, -3.5, -3.5	-3.75, 3.5, 3.5	0.08

Table 4.2: Dimensions for each part in the simulation, where Overlap Overset, Overset and Box Behind is measured in the body fixed coordinate system, while the rest of the parts in the global coordinate system

Port, starboard, top, bottom, inlet, outlet, water surface and overlap will be referred to as the domain, while overset and the lifeboat will be referred to as it is. This is due to the set up in Star-CCM+ where they are assigned as two separate regions.

In Star-CCM+, the domain was assigned as one region with different boundaries, were as the inlet, top and bottom is assigned as velocity inlet. The velocity inlet represents the inlet of a duct for a known flow velocity and is therefore set to zero in this case, as there is no initial current or velocity flows. The outlet of the domain is assigned as pressure outlet. The boundary face velocity is extrapolated from the interior using reconstruction gradients. The boundary condition for the lifeboat is set to wall. There will be no slip at this boundary, meaning that the fluid attached to the boundary will follow the body, resulting in a boundary layer with thickness δ and velocity gradients.

The lifeboat is impermeable, hence there will be no fluid passing through this boundary. Port and starboard side of the domain are assigned as symmetry plane. The symmetry plane can be seen as walls, due to the impermeability. However, slip condition is applied, which results in zero shear stress. The assigned parts should be placed such that the velocities at the boundaries is equal to the inlet velocity, resulting in zero velocity gradients close to the assigned parts. Large velocity gradients close to or in the boundaries will influence the simulations, therefore a large domain for this case was necessary. The overset is the interaction between the two regions, domain and lifeboat, and is where the volume to solve on is generated. For the interaction between the domain and overset to work properly, the mesh size in the overset cannot be smaller than half of the mesh size in the overlap region. (Steve CD adapco, 2016)

4.3 Mesh configurations

In order to get accurate results, a good mesh configuration is needed. In this thesis, a region based meshing was used combined with the Star-CCM+ overset mesh, where the overset mesh follows the body. The overset mesh describes how the regions in the simulation are related to each other, it creates an interface between the background (domain) and the body in question (the lifeboat). The mesh is generated with surface re-mesher, trimmer and prism layer options are enabled. Surface re-mesher uses the existing surface and optimizes it for the volume mesh models. The trimmer model is used to provide a robust and efficient method of producing a high-quality grid for both simple and complex mesh generation problems. Here hexahedra cells were used with smaller cells closer to the body such that all data were captured. The prism layer model is used with the two other models to generate orthogonal prismatic cells next to wall surfaces or boundaries. This layer of cells is necessary to improve the

accuracy of the flow solution, due to better capturing of velocity gradient and viscous effects. It should be pointed out that the mesh operation is time-consuming, since the solving area should be large enough, such that near-wall disturbances do not occur. In this case it will be the lifeboat inside the overset region. The complete mesh is shown in Figure 4.4.

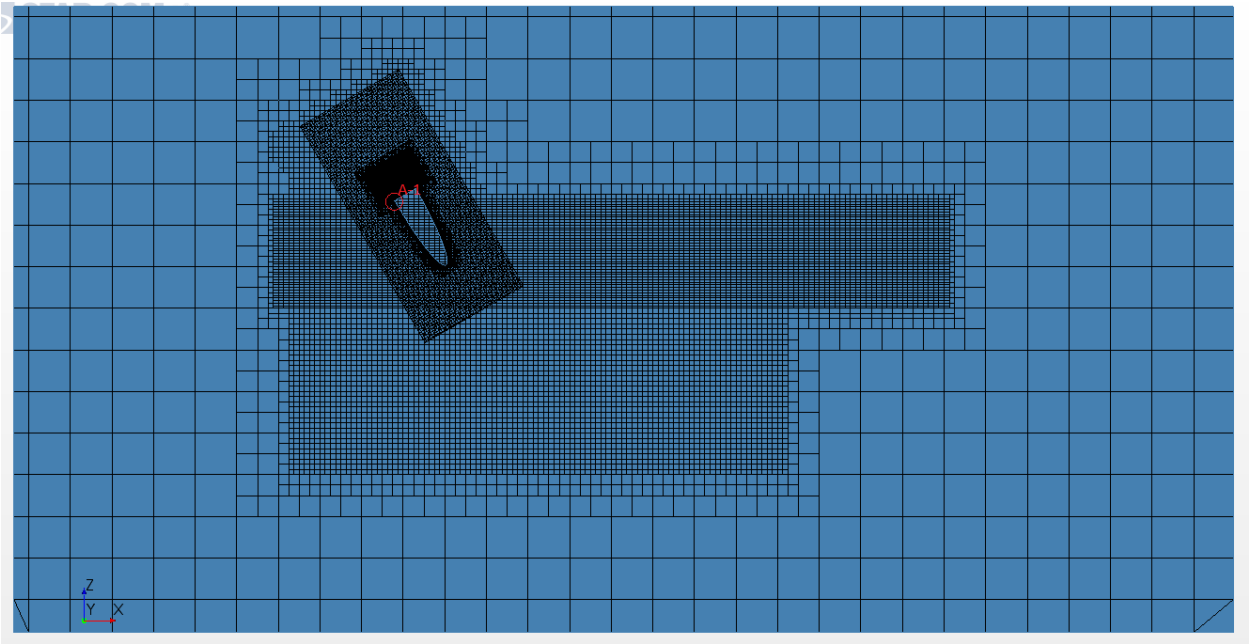

Figure 4.4: Mesh

As mention in section 0

Wall Y^+ **,** the closest cell to the body should be so small that the wall Y^+ value is within the region of the selected model. This was done using the prism layer model, as mentioned, where the total height, number of prismatic layers and height for the cell closest to the body were inserted into Star-CCM+. The total height of the prism layers is influenced by the number of prism layers, and this number was recommended by Star-CCM+ user guide to ensure a stretch factor over the cells to be between 1.3 and 1.5. Though the simulations were conducted with varying mesh size, the cell height closest to the body were kept constant in the prism layer, hence small changes for the Y^+ values.

$$X_h = x_{min} * \sum_{n=0}^{N} f_{stretch}^{n} \qquad [35]$$

Equation [35] shows how the prism layer height, X_h, is obtained from the minimum cell size, x_{min}, and stretch factor, f_{strech}. To ensure a smooth transition between the prism layer and the surrounding mesh the total height of the prism layer and the last cell in the prism layer is close to the size of the first cell outside the prism layer, as seen in Figure 4.5.

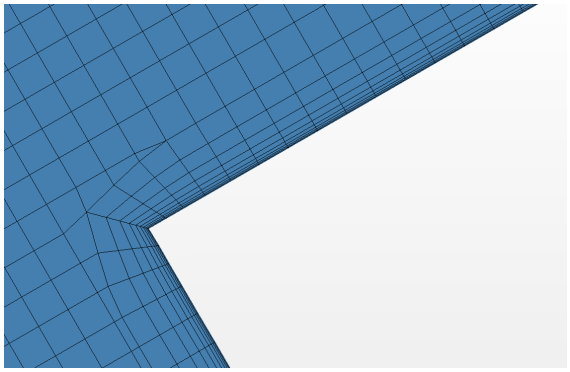

Figure 4.5: Prism layer illustration on the corner, cut-out A-1 from Figure 4.4

To capture the behaviour of the air cavity formed on the aft, a refined mesh was applied here, as seen in Figure 4.6**.**

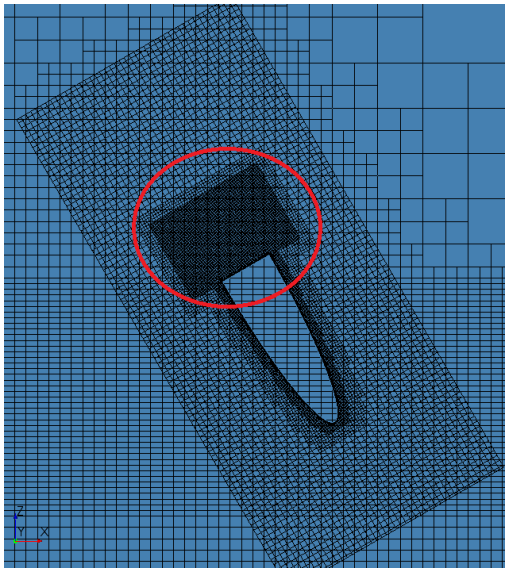

Figure 4.6: Refined mesh on aft part inside the overset

4.4 Applied physics

As described in section 3.3 Star-CCM+ offers a large variety of physics modules. In order to narrow the modules down for the case of a free-falling lifeboat, the work done by (Berchiche, et al., 2015), (Califano & Brinchmann, 2013) and (Tregde, 2015) has been used as guidelines. For this thesis the main physic modules are found in Figure 4.7.

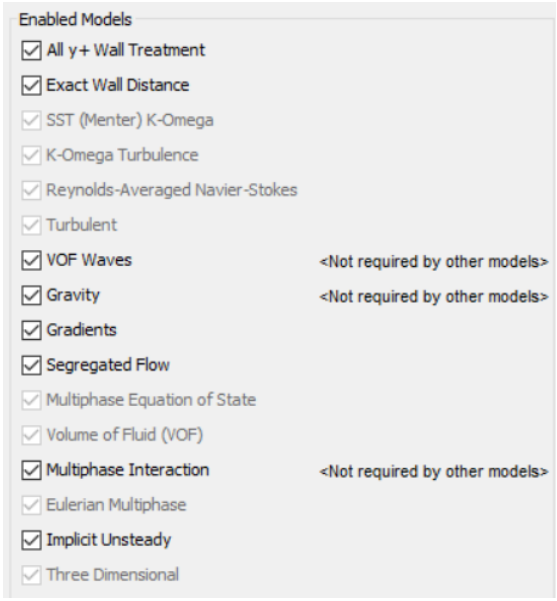

Figure 4.7: Main applied physics in the simulations

For the simulations discussed in 3.2 Berchice et al. (2015) used a laminar flow, Califano & Brinchmann (2013) used a K-Omega module and Tregde (2015) a K-Epsillon module. Simulations with different turbulence models were conducted, where the difference in path and acceleration were unnoticeable. K-epsilon had longer solving time then K-omega for the same time step, but tolerated a higher time step before the simulation diverged. The reason for the all Y^+ treatment, was due to the density difference in water and air causing huge variation for the Y^+ at the same time instance, resulting in some values lower than 30. Y^+ values outside the log layer relation is less realizable for high Y^+, as mentioned in section 0

Wall Y^+. Therefore, a hybrid version of low and high wall Y^+ where chosen.

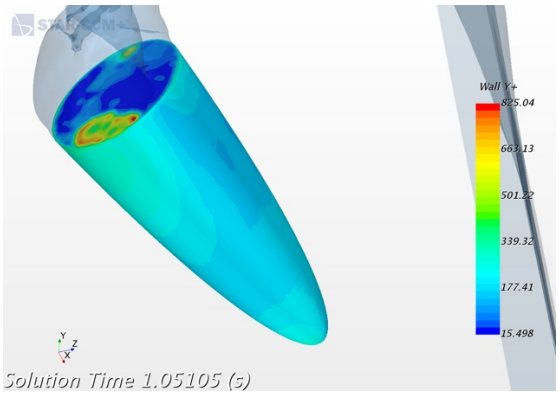

Figure 4.8: In the aft part of the body, air is still entrapped after 1.05 seconds, though the body is fully submerged, results in Y^+ values below 30.

Both (Califano & Brinchmann, 2013) and (Berchiche, et al., 2015) used an implicit unsteady time scheme with second order temporal discretization. An unsteady time scheme with second order temporal discretization have been applied for all the simulations conducted with incompressible air. The interface technique has been VOF for all the simulations, where the basic concept regarding this method is mentioned in section 3.3.2.

The solver chosen is the segregated flow solver, mentioned in section 3.3.1.1. It should be noted that the segregated flow solver can handle mildly compressible flows and low Rayleigh number natural convection, but it is not suitable for shock capturing, high Mach number and Rayleigh number amplifications. (Steve CD adapco, 2016)

5 Sensitivity & Convergence

In order to get accurate results, it is necessary to determine a time step that correlates with the grid and mesh size. In addition, a sufficient amount of iterations for each time step has to be obtained, such that each time step converges.

A convergence study has been conducted to see how the cell size in the grid affects the solution. It is assumed that the solution is improved by decreasing the cell size. A convergence study is also useful for selecting the mesh size with respect to solution quality and computational time.

5.1 Sensitivity Analysis

The sensitivity analysis has been conducted for the mesh with the lowest number of cells. This is for the sake of the low CPU cost, and acceptable results for the purpose.

5.1.1 Residuals

The residuals indicate how well the governing equations for each solver quantity are being satisfied numerically. This will be different for each simulation due to the varying Δt, but as the Star-CCM+ user guide states: The amount that a residual decrease is dependent on the particulars of the simulations. Therefore a drop of 3-4 magnitude in the residuals might be sufficient for one simulations, but not for another. (Steve CD adapco, 2016) This does not indicate that the solution necessarily is the correct one, but the correct one for that mesh size with the corresponding Δt.

Figure 5.1: Residuals for the whole simulation with Δt =1.2ms and 10 inner iterations.

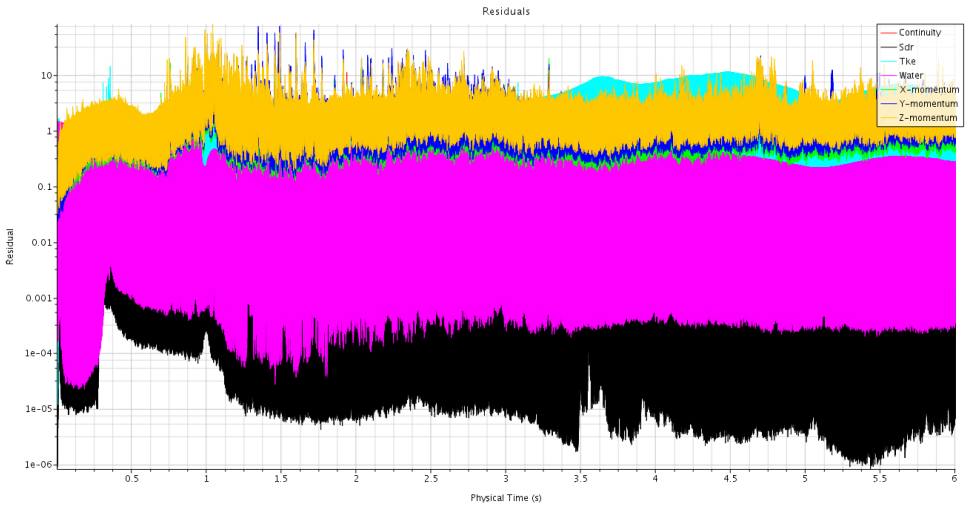

Figure 5.2: Residuals for the complete simulation with Δt=0.6ms and 10 inner iterations

By comparing the residuals values for each of the two time steps, Figure 5.1 and Figure 5.2, it is possible to see that the solver gets better residual values for lower time steps. The most critical area for the solver is around 0.3 s - 0.6 s, in the transition between water entry phase and submerged phase. As for the two time steps, 1.2 ms and 0.6 ms, the difference between the residuals in this critical region is in the order of approximately 10^9. Mentioned in 3.3.4, unphysical numerical solution might occur for sudden changes in geometry in connection with interaction with free surfaces, if the time step is not sufficiently low. Seen from Figure 5.1, the turbulence model (Tke) seems to diverge after approximately

0.45 s. This is when the sharp corners on the aft part of the body gets submerged, and unphysically high fluid accelerations may influence the robustness of the turbulence model. Therefore, the lowest time step of 0.6 ms was chosen to correspond with the coarsest grid.

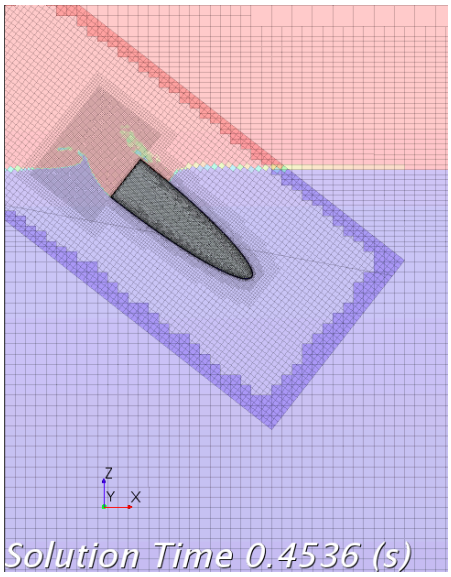

Figure 5.3: VOF picture approximately from where the turbulence model starts to diverge for larger time steps, even though the time steps are relatively small

5.1.2 Number of iterations

The maximum inner iteration is based on the number of inner iterations that the solver executes for transient analyses. As for the 6-DOF solver, it computes fluid forces, moment and gravitational forces on a 6-DOF body, in this case the lifeboat. Pressure and shear forces are integrated over the surface of the lifeboat. The forces and moments acting on the 6-DOF body are used to compute the translational motion of the center of mass of the body and the angular motion of the orientation of the lifeboat.

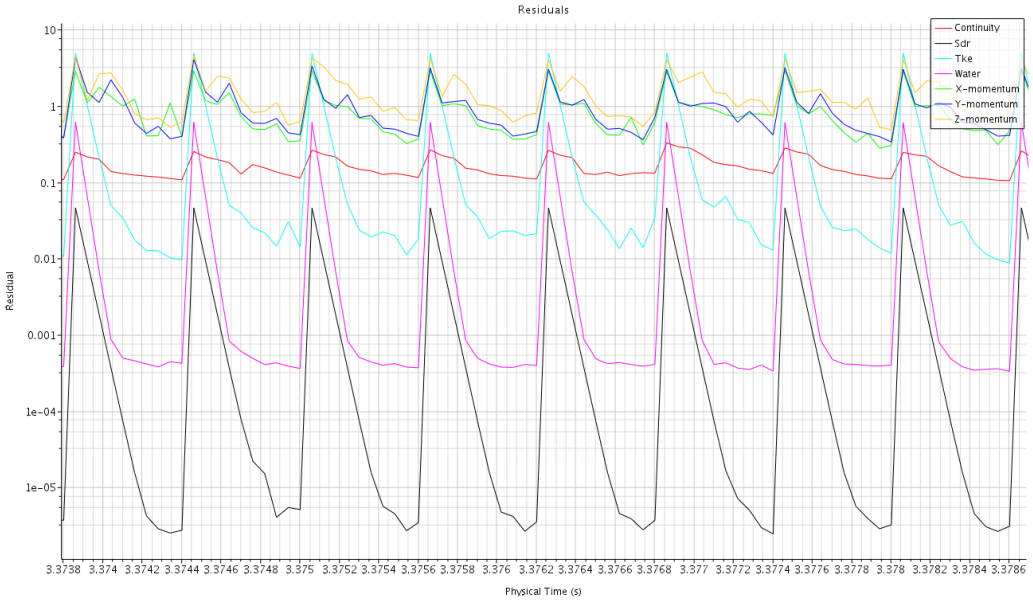

Figure 5.4: Residuals where the iterations for each time step is showed

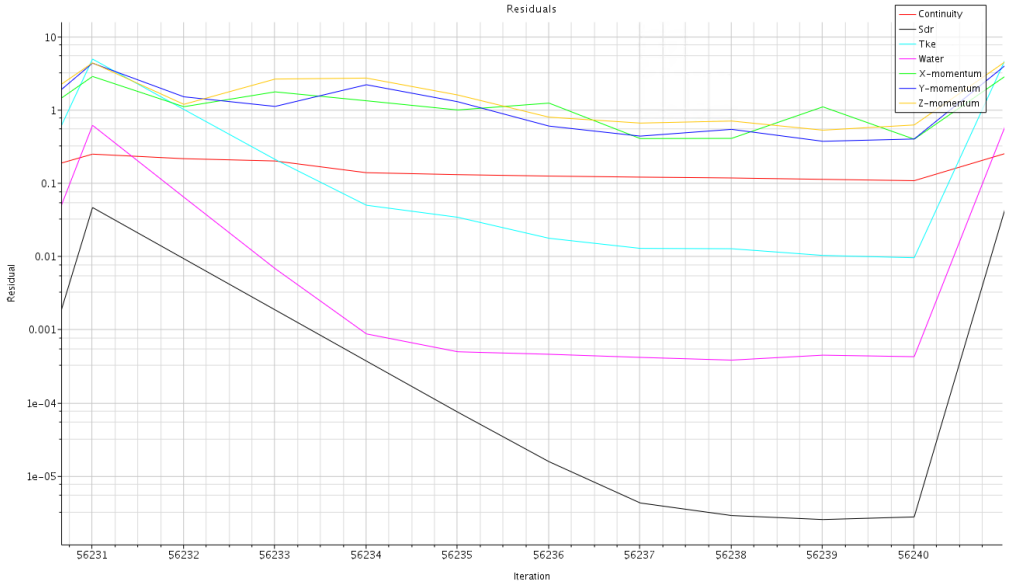

Figure 5.5: Residuals for one time step

An analysis to find the most efficient and precise number of inner iterations were conducted for respectively 6, 10 and 14 inner iterations. All the simulations were conducted with the same mesh and grid configuration for a time step of 0.6 ms, which was found from 0. With 10 inner iterations, the residual values seem to flatten out and converge at the end of each Δt after approximately 8-9 inner

iterations, as seen in Figure 5.4 - Figure 5.5. Hence, 10 iterations are chosen as a basis for the varies simulations and 4 DOF-solver iterations.

5.1.3 CFL number analysis

Two different simulations with a time step of 1.2 ms and 0.6 ms were conducted to determine the sensitivity of the simulation with respect to the CFL value.

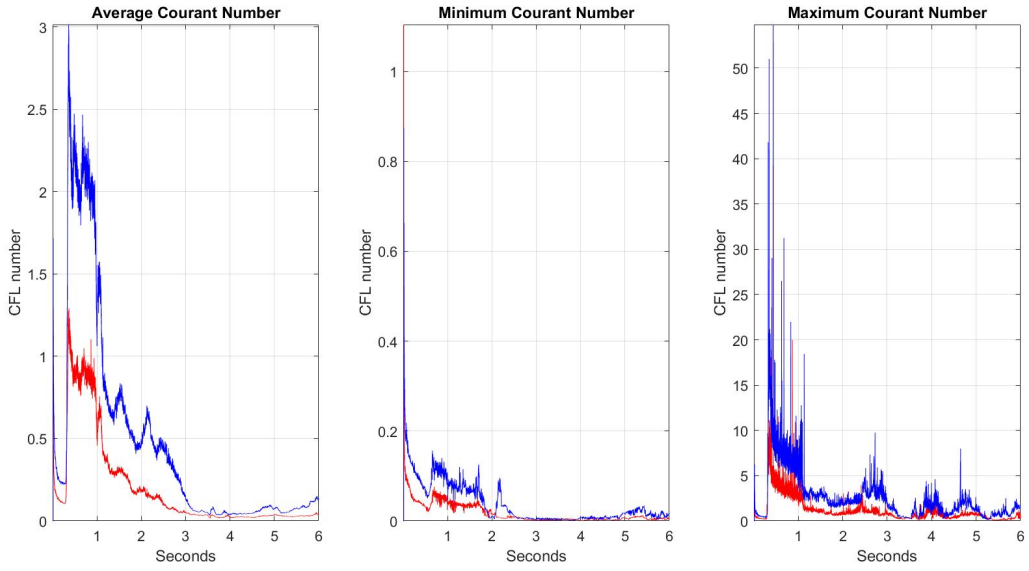

Figure 5.6: CFL values for free surface interaction, where blue is for Δt=1.2ms and red is for Δt=0.6ms

As described in section 3.3.4 the CFL number gives an indication of the ratio between the simulated fluid distance for a given time step, Δt, and the length of one cell, Δx. The values in the plots above are measured in the aft part of the body where the air cavity is located. The CFL plots for the two given time steps, seem to have the same trend, where the simulation with the lowest time step corresponds with lower CFL, which is reasonable.

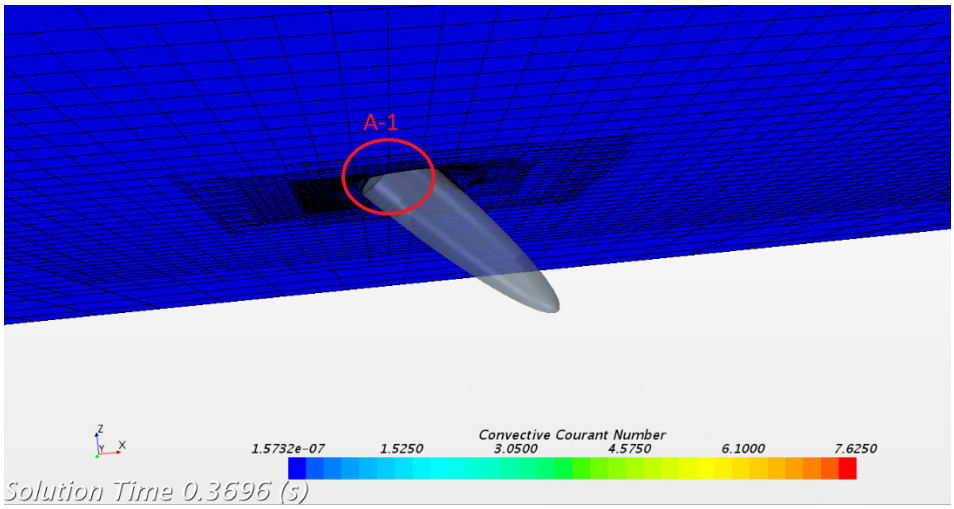

Figure 5.7: Courant scene for a global view at the end of water entry phase

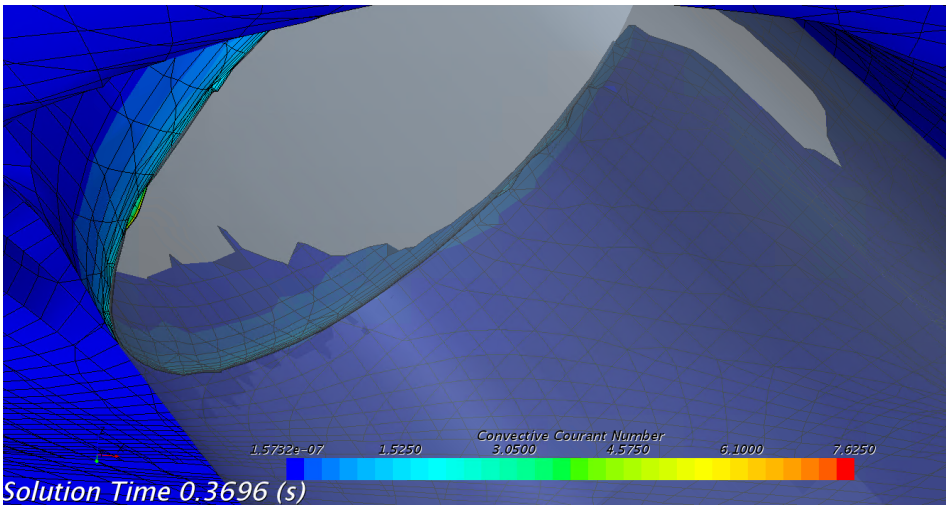

Figure 5.8: Local Courant scene from cut A-1 in Figure 5.7

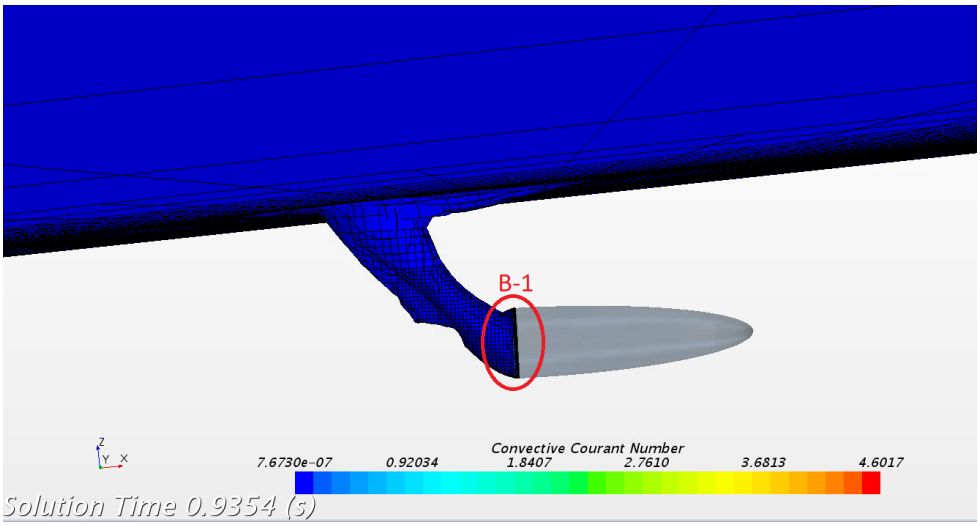

Figure 5.9: Global Courant scene right before cavity closure

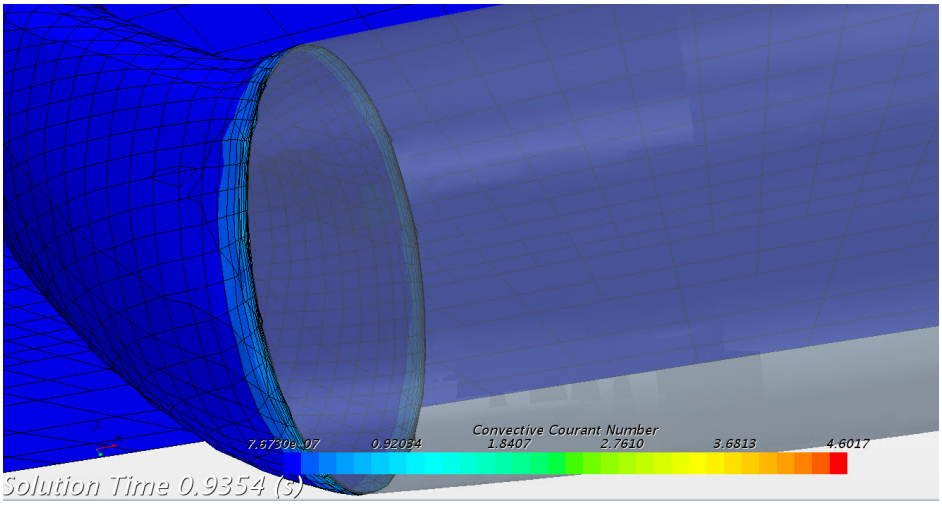

Figure 5.10: Local Courant scene right before cavity closure, cut B-1 from Figure 5.9

Both Figure 5.8 and Figure 5.10 shows the local CFL number, which indicates that the value has its maximum in the sharp corner on the aft part. This corresponds well with increased fluid acceleration around corners, and smallest cell size closest to the lifeboat surface (prism layer).

5.2 Convergence Study

In pursuance to investigate the convergence of the solution, the cell sizes in the grid has been changed. All the cells within the coarsest grid has been halved ones for the medium grid and twice for the finest grid. In favour of having a more reliable convergence study, this is also done for the time step. Than the CFL-number will be quite similar, though cell sizes is different. Meaning that the main parameter influencing the solution will be the cell size. An overview of the meshes is given in Table 5.1, and for the prism layers in Table 5.2. The parameters that will be investigated in this convergence study is acceleration, motion and pressure on the aft part of the lifeboat. The plots are integrated for global convergence and local points are selected for interesting points of time.

SMALLEST CELL SIZE $[m]$	**DISCRETIZATION**	**# CELLS LOCATED IN THE DOMAIN**	**# CELLS LOCATED IN THE OVERSET**	**TIMESTEP** $[s]$
0,16	Δx_3	88 186	203 043	0.0006
0,08	Δx_2	585 083	1 003 599	0.0003
0,04	Δx_1	4 409 925	6 839 080	0.00015

Table 5.1: Mesh description, where the cell sizes from the prism layer is excluded as smallest cell

	Δx_3	Δx_2	Δx_1
# OF PRISM LAYERS	12	10	16
TOTAL PRISM LAYERS HEIGHT [M]	0.31858	0.1527	0.16023
STRETCH FACTOR	1.4983	1.516	1.2419
CELL HEIGHT CLOSEST TO THE BODY [M]	0.00125	0.00125	0.00125

Table 5.2: Prism layer specification for each mesh discretization

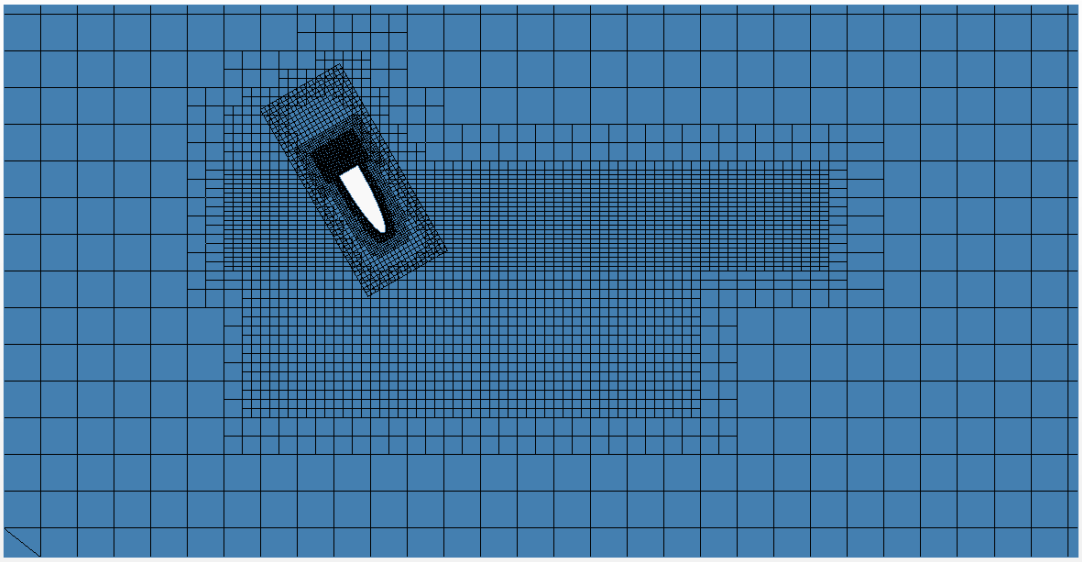

Figure 5.11: Mesh with 0,16 m as smallest cell, discretization Δx_3

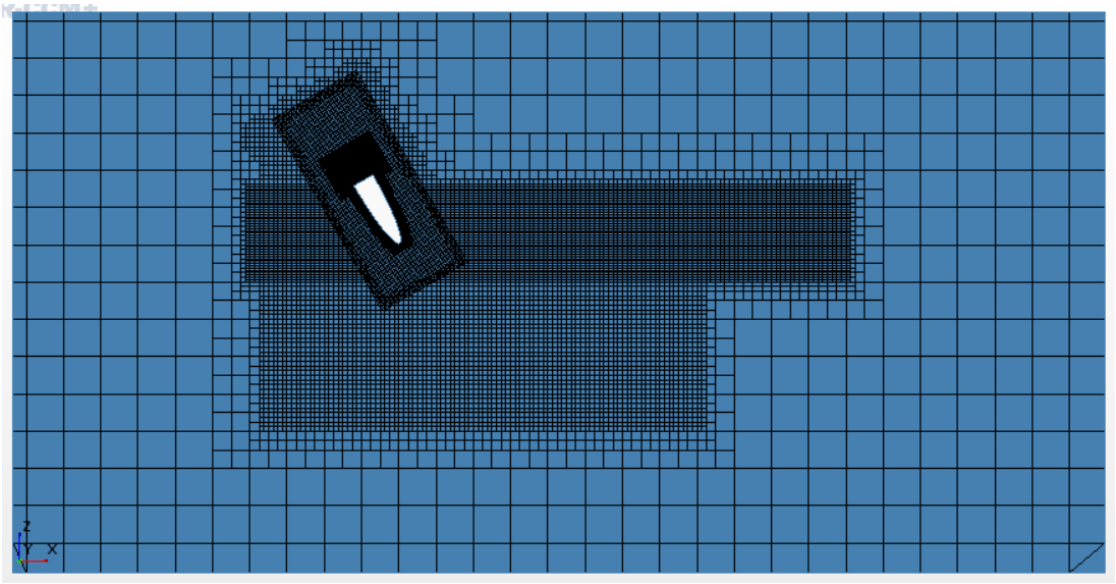

Figure 5.12: Mesh with 0,08 m as smallest cell, discretization Δx_2

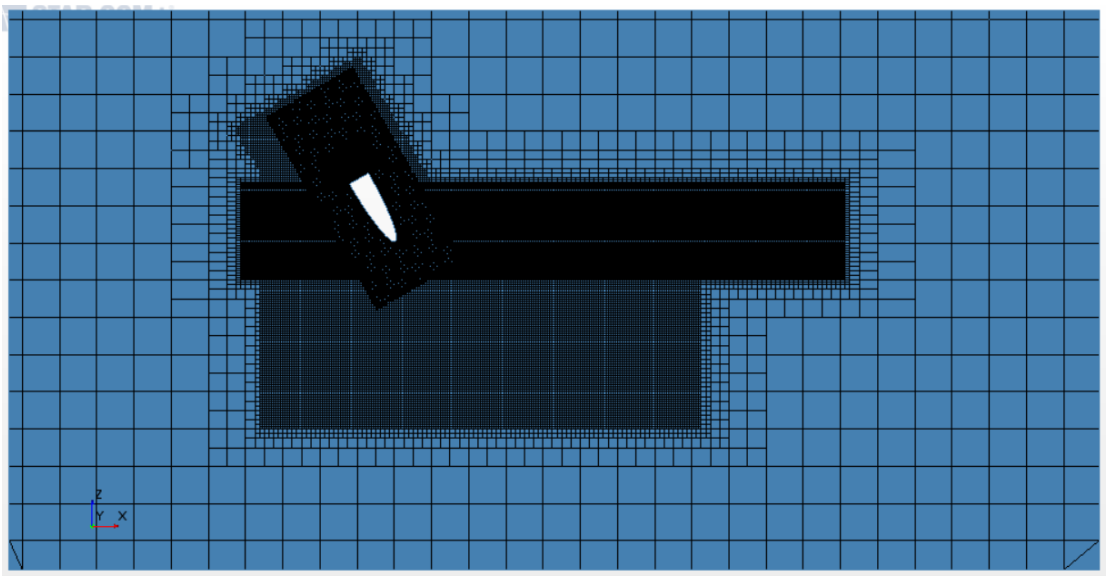

Figure 5.13: Mesh with 0,04 m as smallest cell, discretization Δx_1

As seen in Figure 5.11 - Figure 5.13 it is not only the cells located around the body that goes down in size, the water surface and overlap regions are also reduced in size in the same manner as the cells around the body. This is because of the overset mesh interaction with the domain, and it is recommended by the user guide that the overset cells are of similar size as the overlap cells. (Steve CD adapco, 2016)

A convergence study has been carried out, inspired by the paper written by Colicchio, et al. (2006). Assuming that the error approximated for a given quantity, q is proportional to Δx^{OA}. OA is the order of accuracy and has been defined as:

$$OA := \frac{\log\left(\frac{\left|I_g(\Delta x_2) - I_g(\Delta x = 0)\right|}{\left|I_g(\Delta x_1) - I_g(\Delta x = 0)\right|}\right)}{\log\left(\frac{\Delta x_2}{\Delta x_1}\right)} \qquad [36]$$

$I_q(\Delta x_1)$ and $I_q(\Delta x_2)$ are integrated values of given quantity, q, predicted numerically for discretization Δx_1 and Δx_2, representing different mesh resolutions. $I_q(\Delta x = 0)$ represent the exact time integral of the quantity q. Positive values are desired, where larger values mean that the results converge faster to a specific value. Since there has not been conducted experiments for similar lifeboat geometry and very small cell sizes causes too large CPU time, the exact integrated value for given quantities, $I_q(\Delta x = 0)$ is

unknown. Hence, equation [36] has to be modified, where the exact solution can be derived by assuming a linear logarithmic relationship between $I_q$and Δx, by extrapolation from the integrals on three different meshes, $I_q(\Delta x_1), I_q(\Delta x_2)$ and $I_q(\Delta x_3)$. (Colicchio, et al., 2006)

$$-\frac{\log\left(\frac{\left|I_q(\Delta x_2)-I_q(\Delta x=0)\right|}{\left|I_q(\Delta x_1)-I_q(\Delta x=0)\right|}\right)}{\log\left(\frac{\Delta x_2}{\Delta x_1}\right)}=-\frac{\log\left(\frac{\left|I_q(\Delta x_3)-I_q(\Delta x=0)\right|}{\left|I_q(\Delta x_2)-I_q(\Delta x=0)\right|}\right)}{\log\left(\frac{\Delta x_3}{\Delta x_2}\right)} \qquad [\,37\,]$$

The numerical solver uses a 2. order convection scheme. Hence, for the sake of having a satisfactory convergence, the order of accuracy should have a value close to 2.

Since the order of accuracy mostly is determined by integrated quantities, it is important to consider which time interval that is of interest and provide accurate predictions. Time intervals where the various plots intersect, will alter the accuracy since the integrated values may be of similar measure, even though the shape is not. Therefore, the first time interval (yellow area) is chosen from 0.22 s - 0.75 seconds, the second time interval is for the cavity closure peak (blue area) chosen from 0.985 s – 1.0125 s and the third time interval (purple area) chosen from 1.4 s – 2.4 s, shown in Figure 5.14

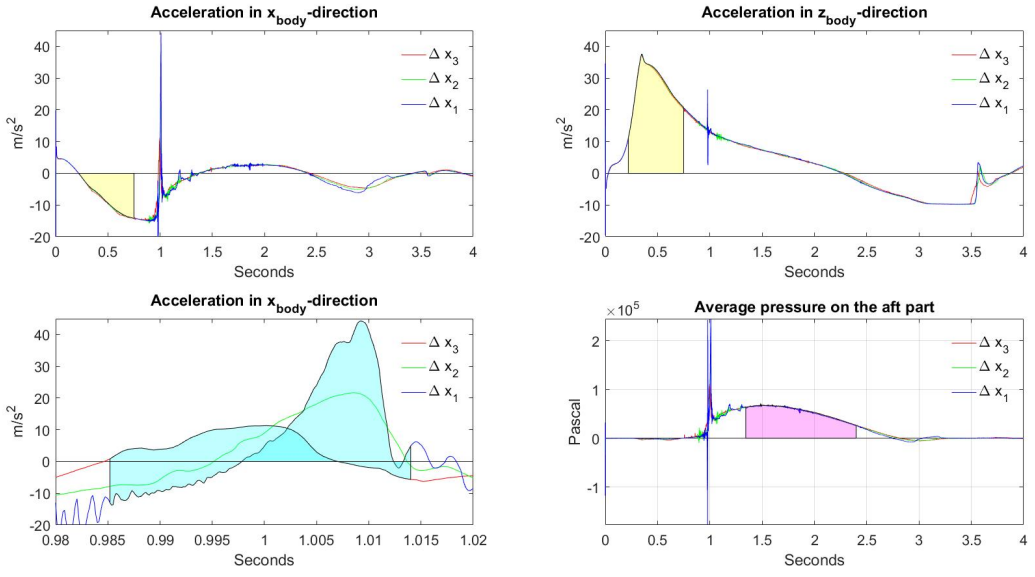

Figure 5.14: Convergence plots, where yellow is the time instance of 0.22 s – 0.75 s, blue 0.985 s – 1.0125 s and purple 1.4 s – 2.4 s

DESCRIPTION OF VALUES	TIME INTERVAL/SINGLE POINT	ORDER OF ACCURACY (OA)
INTEGRATED VALUE OF ACCELERATION IN x_{body}	0.22 s - 0.75 s (water entry phase)	0.545
INTEGRATED VALUE OF ACCELERATION IN z_{body}	0.22 s - 0.75 s (water entry phase)	0.958
INTEGRATED VALUE OF ACCELERATION IN x_{body}	0.985 s - 1.0125 s (air cavity closure peak)	1.190
INTEGRATED VALUE OF AVERAGE PRESSURE IN AFT PART	1.4 s – 2.4 s (Submerged phase, post air cavity closure)	0.546
CAVITY CLOSURE TIME	Single point	3.807
MAXIMUM SUBMERGENCE, z_{global}	Single point	1.384

Table 5.3: Order of accuracy for different integrals and points for selected time intervals and point of time.

All the measures of the order of accuracy are positive, indicating that the two finer grid discretization are more similar than the coarsest for the given quantities. Even though the plots shown in Figure 5.14 are very similar, they do not seem to converge with the order of accuracy that is expected for the solver. As mentioned above, intersection for the varies plot, will alter the reliability of the integrated quantities. This theory gets strengthen, since the OA is significantly higher for single point values, though the cavity closure time indicates a convergence rate, faster than the solvers accuracy. Another error source influencing the order of accuracy, might be the turbulence and corresponding Y^+ model applied. A hybrid model of the Y^+ model was chosen because of the density differences, as mentioned in section 0, Wall Y^+. The code used for modelling of various Y^+ ranges for the hybrid model are not shown in the manual, hence an inaccurate solver method is not unlikely. As for the turbulence, the solver struggled to model the turbulence when the aft part intersected with the free surface even though a relatively low time steps were applied. This will surely alter the order of accuracy, even though it is of secondary importance for short duration of impact problems with flow separation from sharp corners. (Faltinsen & Greco, 2013) The low values in OA can also be caused by the inaccuracy of the coarsest mesh. If the mesh is to coarse, it can lead to large unreal manifestations in the solution, since physics may not be properly simulated. A finer mesh discretization, with a cell height closer to the second finest mesh discretization, Δx_2 , could result in a more satisfactory OA. For the peak interval in Figure 5.14 for the

body fixed x-accelerations, it is easy to see that there is no local convergence due to the large difference in shape of the plot, even though the OA is quite high. However, the trend seems to converge, as the closure time is almost the same for the two finest grids and the maximum submergence point only have a difference of 4 cm between the finest grid and the coarsest grid, which implies global convergence.

DISCRETIZATION	SOLVING TIME $[hours]$	# OF PROCESSORS	CPU COST
Δx_3	25	9	225
Δx_2	51	39	1989
Δx_1	150	272	40800

Table 5.4: Mesh discretization with its specific solving time, number of processors used and computational cost

The solution does not seem to have local convergence. However, the quite similar position plots show that the local accelerations do not have large manifestations in the global behaviour of the body. It is assumed that the finest mesh gives the most accurate results, but it is not computational economic. The second finest mesh has a global solution very close to the finest one. Hence, a compromise between computational time and accuracy is made, and Δx_2 is the chosen mesh discretisation for further studies in this thesis.

6 Results with initial conditions

As concluded with in 5.2, the results presented is obtained with the Δx_2 mesh discretization. This is due to the low CPU cost for each simulation, as well as section 5.2 concludes with that this discretization gives accurate results for most of the phases. This will also give a better representation of the comparison of a change in different parameters in section 7, where this discretization has been used. The results are obtained with an initial condition seen in Table 6.1.

CONDITION	VALUE	DIMENSIONS
WATER ENTRY ANGLE	60	degrees
VELOCITY$_{\text{BODY FIXED}}$	[20, 0, -5]	m/s
ANGULAR ROTATION	15	degrees/s

Table 6.1: Initial conditions

a)

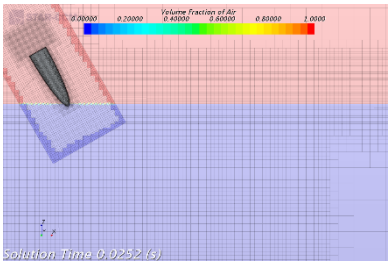

b)

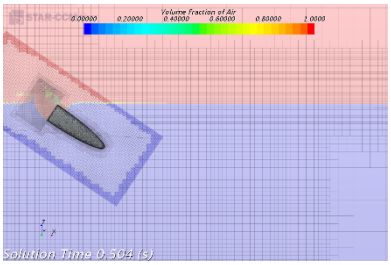

c)

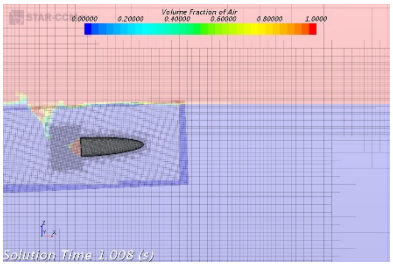

d)

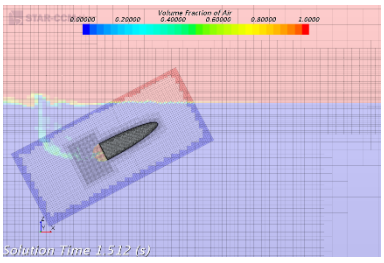

e)

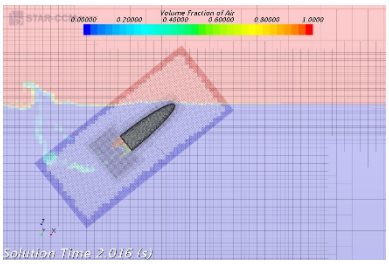

f)

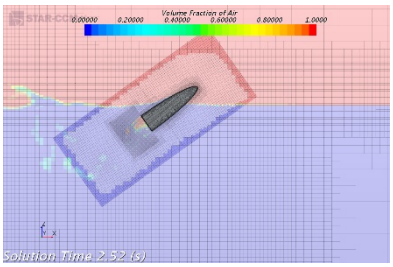

g)

h)

i)

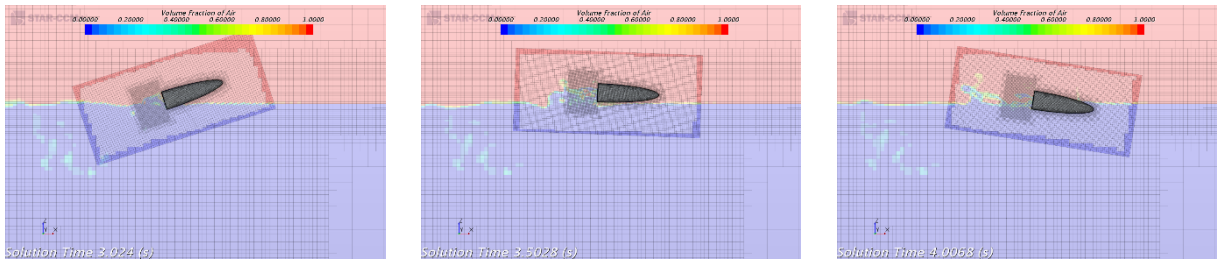

Figure 6.1: VOF of air representation of the path from water entry to sail away

From Figure 6.1 it is possible to see the global behaviour of the path of the lifeboat with its initial conditions.

6.1 Acceleration and angular acceleration

The acceleration results are divided into the different phases the lifeboat goes through, from water entry to sail away phase. The air cavity formation and collapse are also included here.

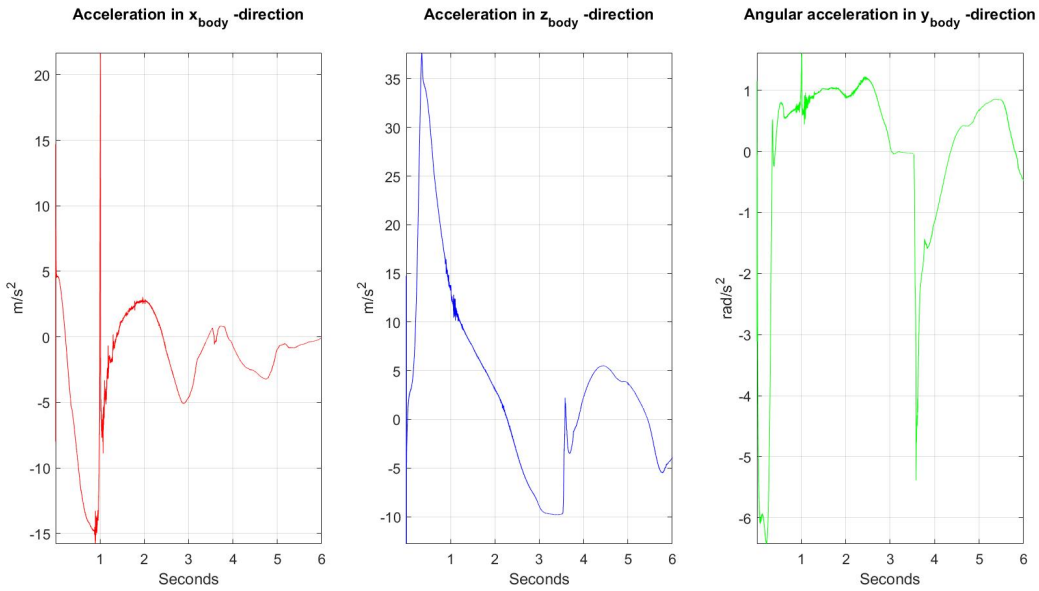

Figure 6.2: Acceleration and angular acceleration measured in the body fixed coordinate system

6.1.1 Water entry

The body has an initial free-falling acceleration, with a constant clockwise rotational velocity, until the water entry starts after 0.0085 s. As the lifeboat bow enters the water it is subjected to slamming forces. As mentioned in section 4.4, the segregated flow solver does not give a good representation of this phenomenon. From the acceleration plot (Figure 6.2), it is possible to see that the initial acceleration is counteracted in both x_{body} and z_{body}. The body will also get counter clockwise angular acceleration, the rotation is decreased and eventually reversed in the water entry. This occurs as the centre of gravity gets pulled down, while the bow is partially constrained in the fluid. When the added mass increases, there is a small clockwise angular acceleration which is slowly increasing for a while.

6.1.2 Air cavity formations

In the acceleration plot from Figure 6.2, the air cavity closure appears as a the large peak in x_{body} acceleration. It is caused by the pressure from the water on the newly formed air bubble located on the aft part of the body. The air in the bubble is modelled as incompressible. A consequence regarding this, is that the entrapped air bubble is rigid, hence the appearance of a single peak with a high value. The air in the entrapped bubble is in fact compressible, the acceleration plot is therefore not realistic at the point of air cavity closure. It is expected that the entrapped air bubble will oscillate in size, and that the first peak will be less pronounced than the peak in Figure 6.2.

a)

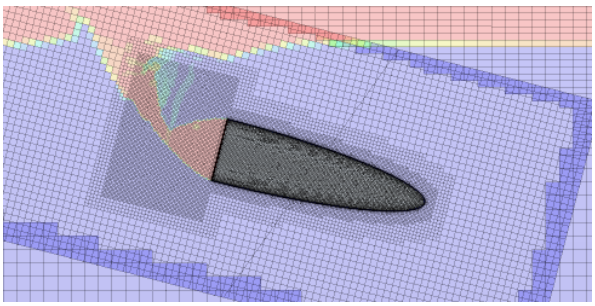

b)

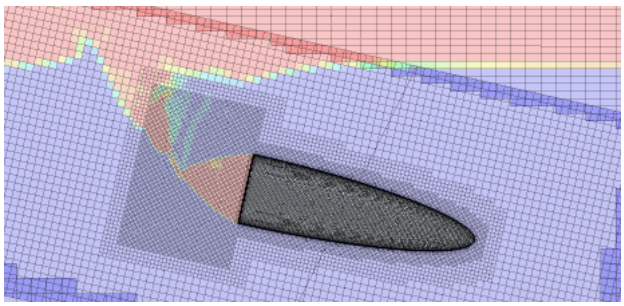

c)

d)

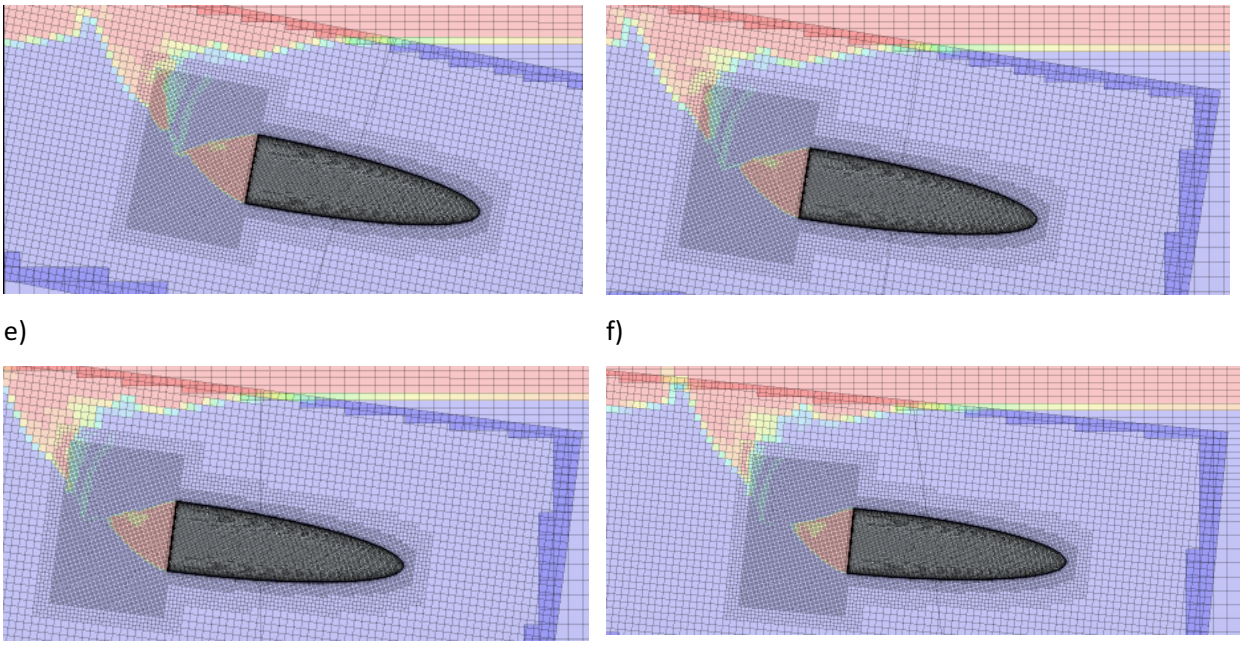

Figure 6.3: Beginning of the air cavity closure, 2-D, starting from solution time 0.756s with $\Delta t = 0.025s$, until 0.882s

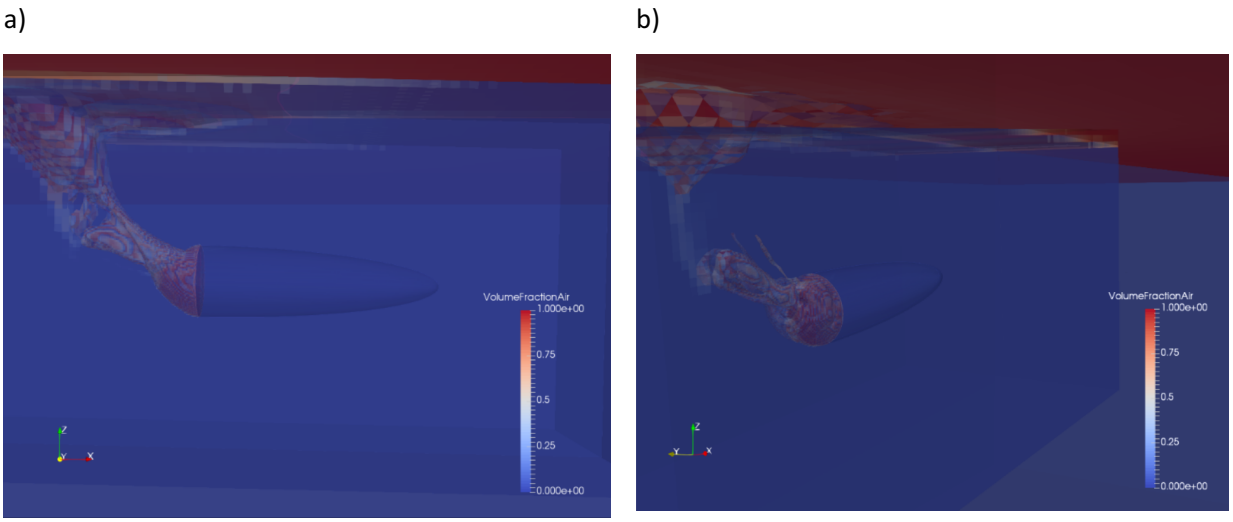

Figure 6.4: Visualization of the air cavity closure in 3D where a) shows the solution time 1.002 s and b) shows solution time 1.102 s

Figure 6.3 shows the air cavity and the beginning of the closure in the period between Figure 6.1 b) and c). As the pictures are in 2D, it is difficult to see the exact moment of air cavity closure later in the time-series. A 3D representation of the air cavity closure is shown in Figure 6.4.

6.1.3 Submerged phase after air cavity formation

The body will continue to rotate, and eventually the x_{body}-direction will be parallel to the water surface. At this position, the body is close to maximum submergence. The body still has a counter clockwise rotation, this can be seen in Figure 6.5. Shortly after maximum submergence, when the bow is turning upwards, the x_{body} motion and the buoyancy force will both have a positive contribution in the global z-direction. The point can be seen at 1.375 s in the x_{body} acceleration in Figure 6.2, where the body gets a positive acceleration contribution. There is a positive x_{body} acceleration contribution until the point where the gravitational forces excide the buoyancy forces at the water exit.

6.1.4 Water exit

As the body exits the water, the buoyancy acts upwards on the aft part, while the gravitational force acts downwards on the fore part. This creates a large increase in clockwise rotation, while the body gets deaccelerated in the negative vertical direction by the gravitational force. The small positive x_{body} acceleration from the gravitational force before re-entering the water, is due to the x_{body}-motion changes in the vertical global direction. As the body has a certain pop-up height, it is subjected to a second slamming at the re-entering of the surface. It is apparent as the peak at 3.6 s in z_{body} acceleration, Figure 6.2.

6.1.5 Sail away phase

After water exit and the second water entry, the body will have a negative acceleration in the body fixed x-axis as it is slowed down by resistance forces, and the only thing driving it forward is the initial water exit velocity.

6.2 Velocity

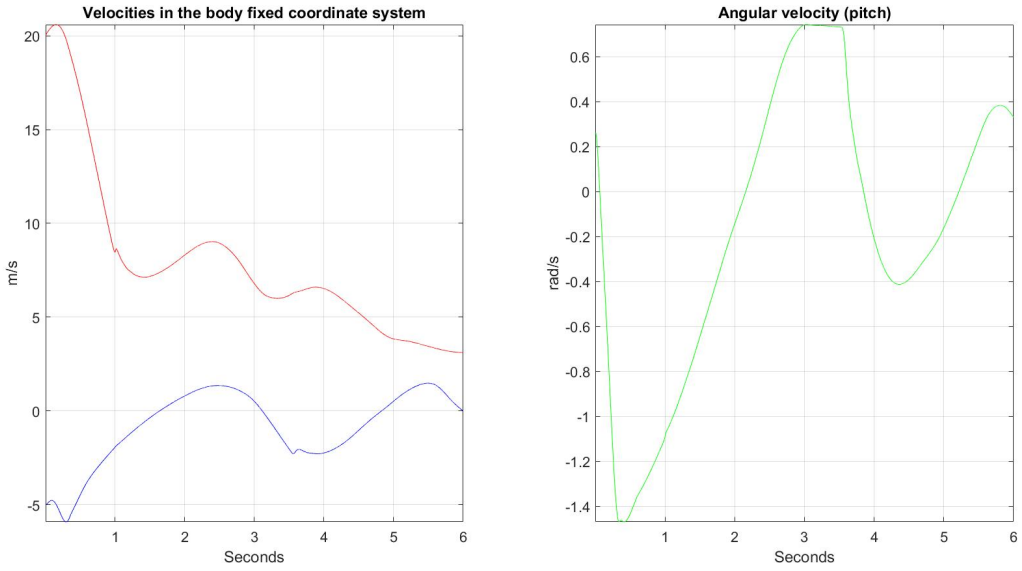

Figure 6.5: Velocity plot where the red is in the x_{body} -direction and blue in z_{body} -direction

The body fixed velocity in x-direction reaches its maximum value after approximately 0.25 seconds. After initial impact the velocity is rapidly decreasing. The body is resurfacing at 2.45 s, this is noticeable in the velocity plot as the body fixed velocities in both x and z has a local maximum for this point. The velocity plot is smother than the acceleration plot, which is logical as the acceleration is the time derivative of the velocity. The large acceleration peaks for the point of air cavity closure and second water entry are shown to have little effect on the velocity, they are noticeable as small discontinuities in the plot at 1.0 s in x_{body} and at 3.5 s in z_{body}, respectively. At 6 s, the body has a positive velocity in x-direction. This is beneficial as the sail away distance will increase as the time passes.

6.3 Motion

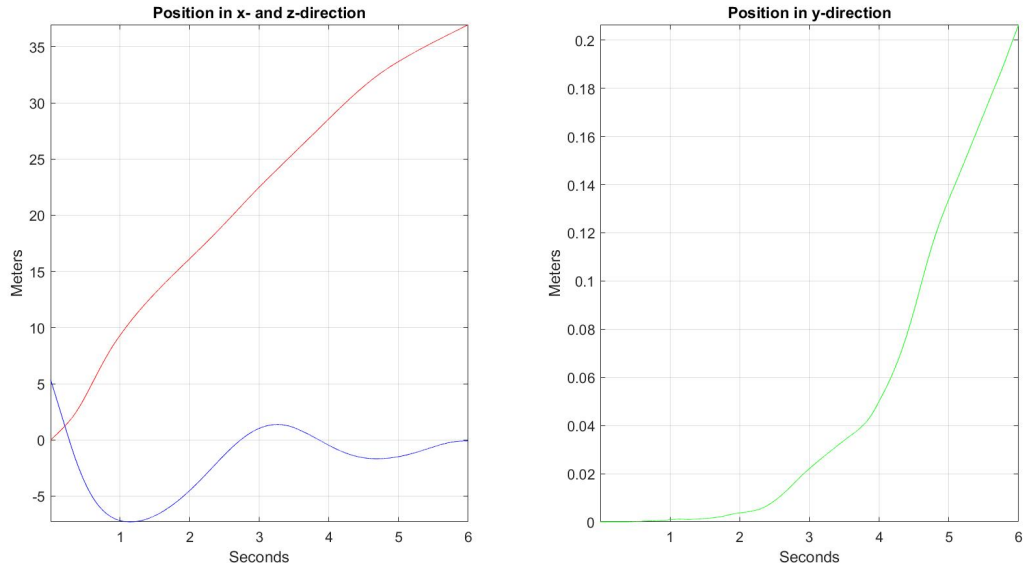

Figure 6.6: Position plot, where the red line is in the x-direction, blue in the z-direction and the green in y-direction

The position is the time integrated velocity. Figure 6.6 shows a continuous line which imply that the impulse forces inflicted at air cavity closure and at the second water entry are not large enough to make sudden changes in the position. The lifeboat reaches maximum submergence after approximately 1.2 seconds with a depth of 7 meters. After 6 seconds, the lifeboat has managed to sail 36 meters away from the point of initial water entry. As seen in Figure 6.5, the velocity is still positive at 6 s, which leads to an increase in sailing distance later on. By comparing the lifeboat motion in Figure 6.6 with Figure 2.8, the lifeboat trajectory shows resemblance with motion pattern 1, where the lifeboat pitches significantly at maximum submergence and ascent so that is surfaces with a positive forward velocity, as seen in Figure 6.1. According to DNV-GL, this is the preferred trajectory. (DNV-GL, 2016)

6.4 Pressure aft

The pressure on the aft part is mostly affected when the body is in the submerged phase, hence this is the period that will be discussed. To be sure of structural integrity in the aft part, e.g. for a weak part like a door, filtering of the pressure peaks is not an option since these large oscillations can results in

local structural failure. Hence, the air cavity should ideally be modelled as compressible for such calculations to be utilized, as Tregde (2015) concludes with in his paper. (Tregde, 2015)

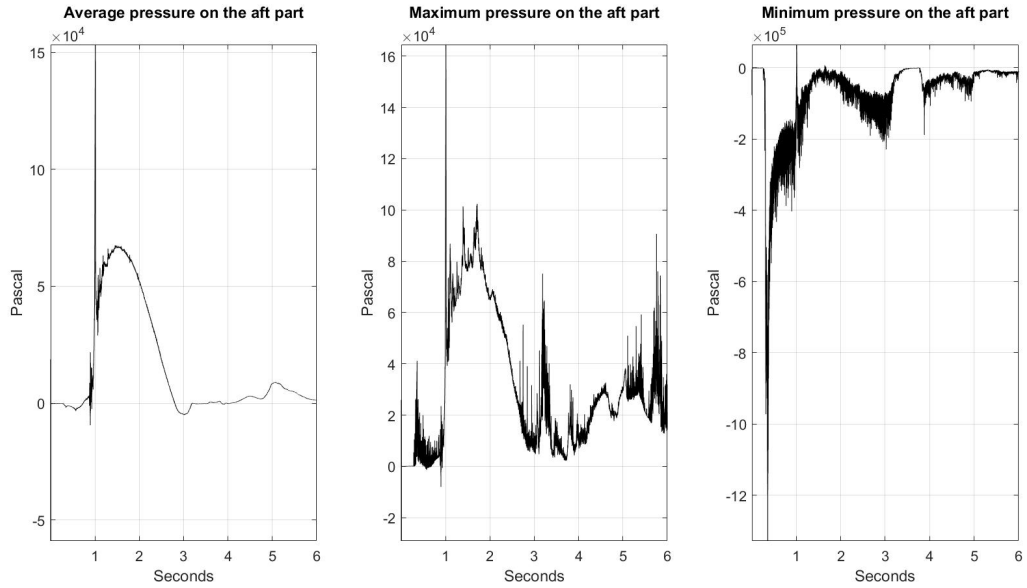

Figure 6.7: Pressure plots on the aft part

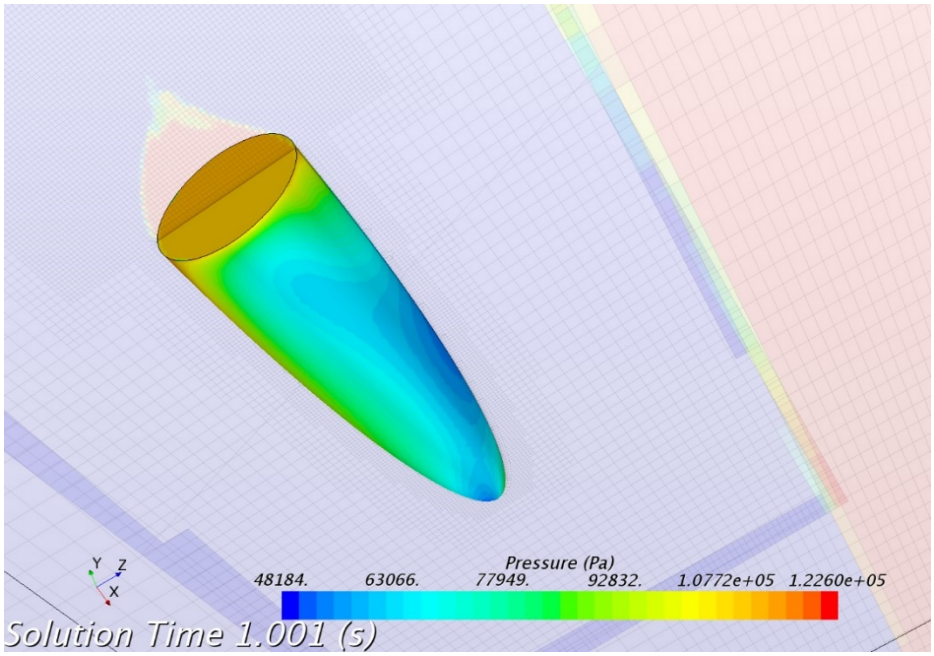

Figure 6.8: Pressure distribution on the lifeboat 7ms before the peak

The pressure is proportional to the acceleration, which means that the peaks should appear at the same distinctive time. By comparing Figure 6.2 and Figure 6.7 is it possible to see the resemblance of this. The air cavity closure is seen as the large peak in Figure 6.7 for average, maximum pressure and also a smaller positive peak for the minimum pressure. Figure 6.8 shows that the high pressures is in the area where the air cavity is located and the lower pressures seen in the minimum pressure plot, Figure 6.7, is in the area where the air cavity ends and water attaches to the body. Throughout the submerged phase, the average pressure and maximum pressure in Figure 6.7 follows the same tendency. As seen in Figure 6.8 the pressure is close to uniformly distributed on the aft part during this phase. The pressure increases until the air bubble is at maximum submersion, due to the hydrostatic pressure. After this the pressure is decreasing until the aft part is above the calm water level.

a) b)

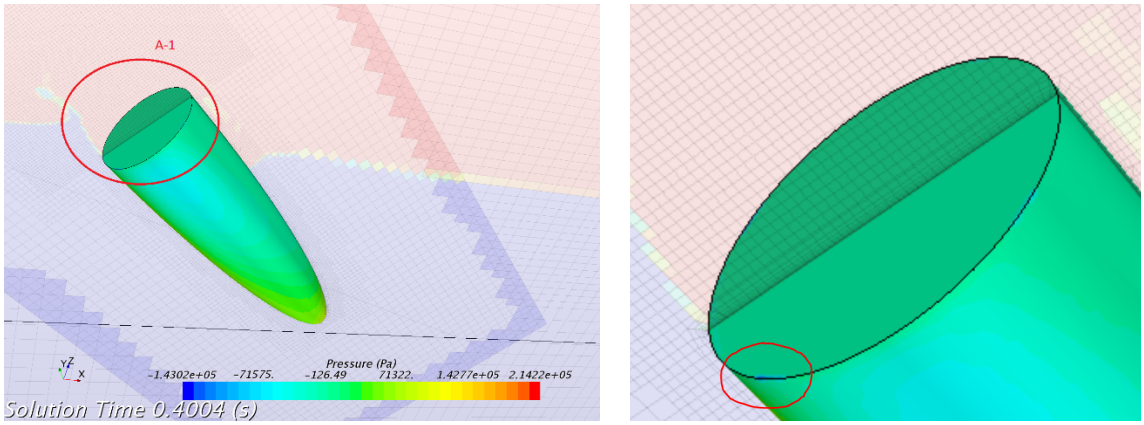

Figure 6.9: Minimum pressures from the splash crown, where a) shows the global and b) more locally of the same time instance

As seen in Figure 6.7 the minimum pressure has large negative values at approximately 0.4 s – 0.6 s, this indicates that the water entry splash crown and the air cavity formation creates a suction on the aft part. This is illustrated in Figure 6.9.

6.5 Comparison with theory

6.5.1 Air cavity investigation

As mentioned in 0, high Capillary number is beneficial to ensure air cavity formation. An air cavity was therefore expected, due to the relatively large viscous forces compared to the surface tension in water and the sharp corners in the aft part. In addition, surface tension has been neglected for the simulations due to its insignificance in the case of lifeboat diving, as mentioned in 0. For Bond number higher then 10^3, only deep and surface seal occurs, where the transition from deep seal to surface seal occurs for $Fr > \sqrt{150}$. This corresponds to a velocity greater than 60 m/s for the body in this thesis. Hence, deep seal is expected, corresponding well to Figure 6.3. f).

In section 0, the derivation between Froude number and closure time is obtained in equation [14]. From studying the VOF-picture at approximatly1 s, a deep seal is apparent. The air cavity height is clearly less than one half of the distance travelled from the entry point in the water surface to the aft part of the body. By studying the VOF-pictures, the aft part of the body gets submerged after 0.4284 s, and the air cavity initiation starts after approximately 0.6 s. The air cavity seems to be largest in diameter for this time instant, meaning that the expansion time is short compared to the collapse time, since the collapse seems to happen at approximately 1.0 s. This results in a closure time $T_c = t_0 + \delta t_2 = 0.17\ s + 0.4\ s = 0.57\ s$. Then by solving equation [14] with a characteristic diameter of 3 m, and a velocity of 20 m/s, the theoretical closing time is calculated to be

$$T_c = \frac{3m}{20m/s}\left(\frac{3}{2^{5/3}}\right)\left(\frac{20m/s}{\sqrt{9{,}81m/s^2 * 3m}}\right)^{2/3} = 0{,}34\ s$$

The body investigated in this thesis has a long cylindrical shape, but the dimensions, centre of gravity and density is somewhat different than the body investigated in the paper from Tan, et al. (2009). (Yan, et al., 2009) An important assumption was that the cavity closure height, H_c was approximately $\frac{1}{3}$ of the cavity height H. For this case, the dimensions of H and H_c is difficult to measure, as the VOF pictures are in 2D. The main difference is that there is an oblique impact and a pitch velocity, the simplified lifeboat geometry has a low density and it is not axisymmetric as the centre of gravity is moved in z-direction. For this derivation, the vertical velocity is also assumed constant, though the decrease is significant. These differences prevent a good comparison.

6.5.2 Water exit

From theory (see section 2.5) the relationship between the pop-up height and the water exit velocity in the global vertical direction can be tested utilizing equation [16]. When the centre of gravity passes the water surface, the global vertical velocity is:

$$w_{global} = \frac{8.6m}{s} * \sin(27°) + \frac{1.25\ m}{s} * \cos(27°) = 5.02\ m/s$$

For the simplified case, then the pop-up height should approximately be

$$H_{pop-up} = \frac{v_{vert}^2}{2g} = 1.28\ m$$

From the motion plot, the pop up height is read to be 1.23 m, corresponding well with the assumption that energy is lost due to splash plume and wave making. (Truscott, et al., 2016)

6.6 Courant validation

An indication of the expected CFL were investigated for the coarsest grid discretization, mentioned in section 5.1. Therefore, a new validation is needed, though the time step used is two times smaller.

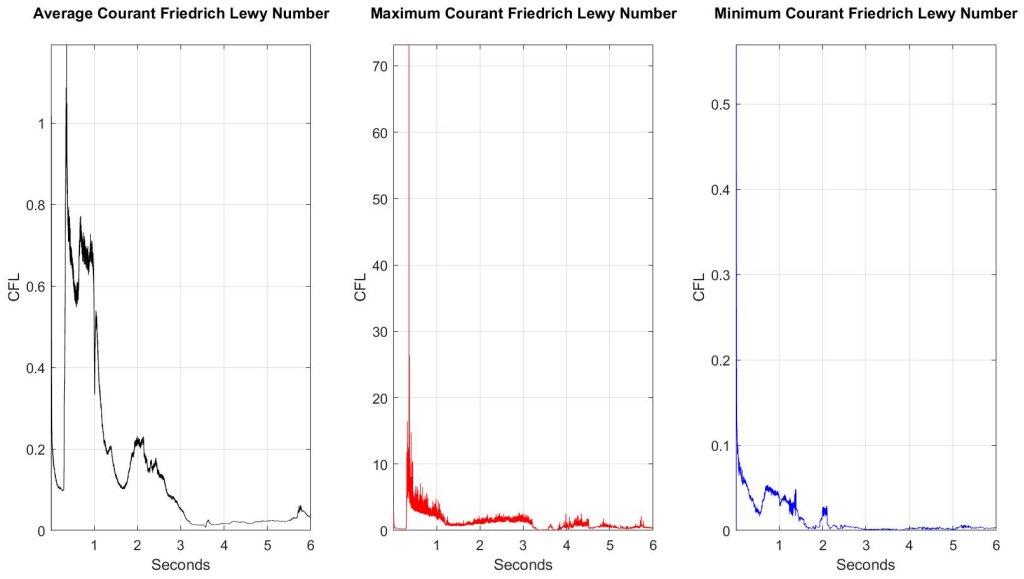

Figure 6.10: CFL number throughout the simulation

The average CFL number measured in the cells located around the aft part of the body shows resembles to the average CFL values for the coarsest mesh discretization, Δx_3, which is reasonable considering the solver approach for solving this value. There is still a distinctive peak at approximately 0.4 seconds, where problems related to solving the turbulence model occurred. This matter will be investigated later in error sources

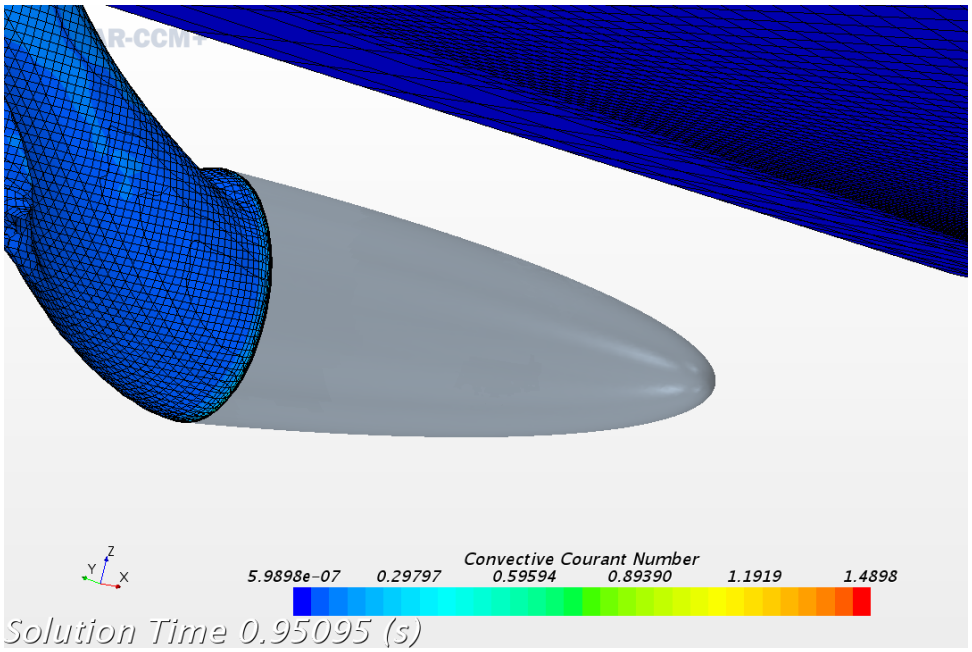

Figure 6.11: CFL visualization

The highest CFL values are still located around the sharp corners on the aft part of the body, but smaller in magnitude compared to the coarsest grid. This is probably a result of relatively similar prism layer distribution in terms of height for the varies mesh discretization's, though the time step is halved.

7 Parameter investigation

Since a lifeboat is a last resort solution of escaping the mother vessel, the weather conditions will not likely be ideal. The launching and free-falling phase can therefore be affected, which results in difference in the behaviour in the four later phases, as described in section 2. The water entry angle and the velocity are two parameters that can be affected by wind loads and by which wave phase it is entering. Also, the centre of gravity can change, as it depends on the number of passengers and their seating arrangement. Hence, an investigation of the effect these changes can have, has been carried out. The chosen values are shown in Table 7.1. Only one parameter will be changed for each simulation, in the interest of examining the influence of the different parameters. However, if the free-falling time and distance increases, both velocity and water entry angle is likely to increase.

PARAMETER		**-**	**IC**	**+**	**Δ**
$\boldsymbol{\theta}$	[°]	55	60	65	5
COG_z	[m]	-0.7	-0.5	-0.3	0.2
V	[m/s]	15.62	20.62	25.62	5

Table 7.1: Parameter investigation values

From these parameters, accelerations, velocities, air cavity formation, path and pressure has been studied to get an insight of how they are changing with the varying parameters.

7.1 Velocity

Three different velocities have been tested to investigate the effect they will have for the behaviour of the body. Their maximum values are 15.62 m/s, 20.62 m/s and 25.62 m/s. The ratio between the velocities in x_{body} and z_{body} is held constant.

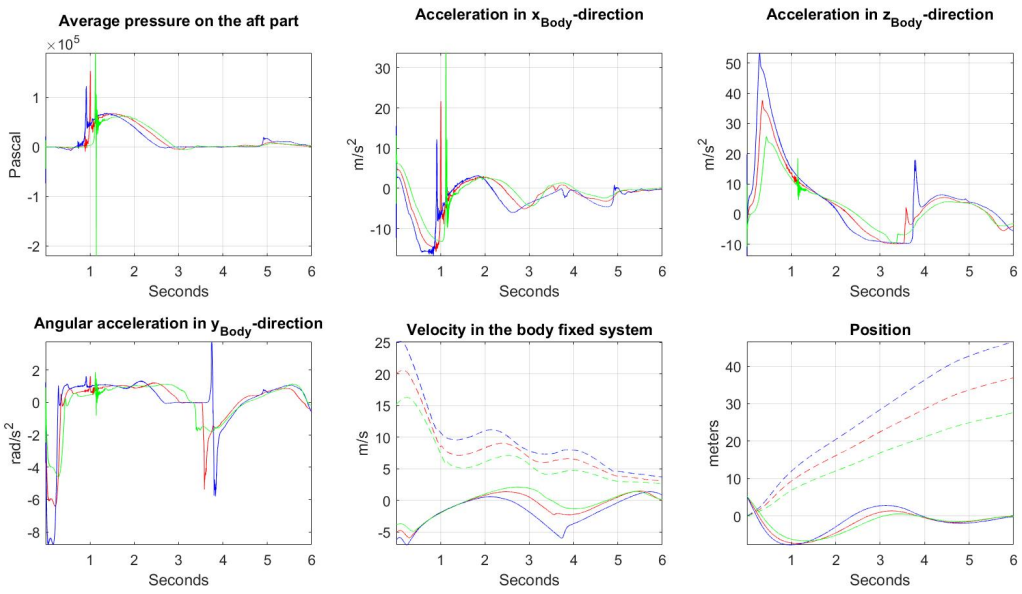

Figure 7.1: Green is 15.62 m/s, red is IC with maximum velocity 20.62 m/s and blue is 25.62 m/s. The accelerations and velocities are taken in the body fixed coordinate system. The dashed lines are in the x-direction, and the solid lines are in the z-direction in the velocity and position plots.

	15.62 m/s	**INITIAL CONDITION** **20.62** m/s	**25.62** m/s
CAVITY CLOSURE TIME (PEAK) $[s]$	1.121	1.009	0.915
WATER EXIT TIME $[s]$	3.073	2.730	2.366
POP-UP HEIGHT $[m]$	0.557	1.369	2.835
MAXIMUM SUBMERSION $[m]$	-6.633	-7.297	-7.700
SAILING DISTANCE AT 6 s $[m]$	27.635	36.969	46.619
VELOCITY x_{Body} **AT 6** s $[m/s]$	2.709	3.109	3.685
ACCELERATION PEAK MAGNITUDE $[m/s^2]$	33.720	21.678	12.189
MAX PRESSURE AFTER CAVITY CLOSURE $[kN/m^2]$	62.390	67.460	68.420

Table 7.2: Distinctive values for comparison the change in water entry velocity

The plots in Figure 7.1 reveal great differences. The accelerations in x_{body} and z_{body} is clearly largest for the high impact velocity case. It also has the most negative angular acceleration at the water impact phase, hence it will contribute the most to the counter clockwise rotation. The air cavity closure occurs earlier for the case with the highest velocity, this compares well with equation [14] The global horizontal velocity at the point of maximum submergence has a significantly larger value for the case

with the highest initial velocity, then for the two other cases. This, combined with a higher counter clockwise rotation, leads to high water exit velocity and angle. The result is an early water exit and a large pop-up height. As it "shoots" out of the water with high energy, it will get the longest sailing distance at 6 s. And since it also has the highest velocity at this point of time, it will have the best potential for sailing further away from the evacuation scene. The maximum submergence is also quite different, which is an important parameter since it is proportional to the hydrostatic pressure, when assuming constant density. High hydrostatic pressure is of concern for asymmetric geometry like appendages, as a result of the varying pressure loads. This can further cause implosions.

7.2 Water entry angle

A preferable water entry angle is approximately 60°. However, the different external forces affecting the lifeboat can change this. Three different water entry angles have been tested to investigate the effect they will have for the behaviour of the body. Their values are 55°, 60° and 65°.

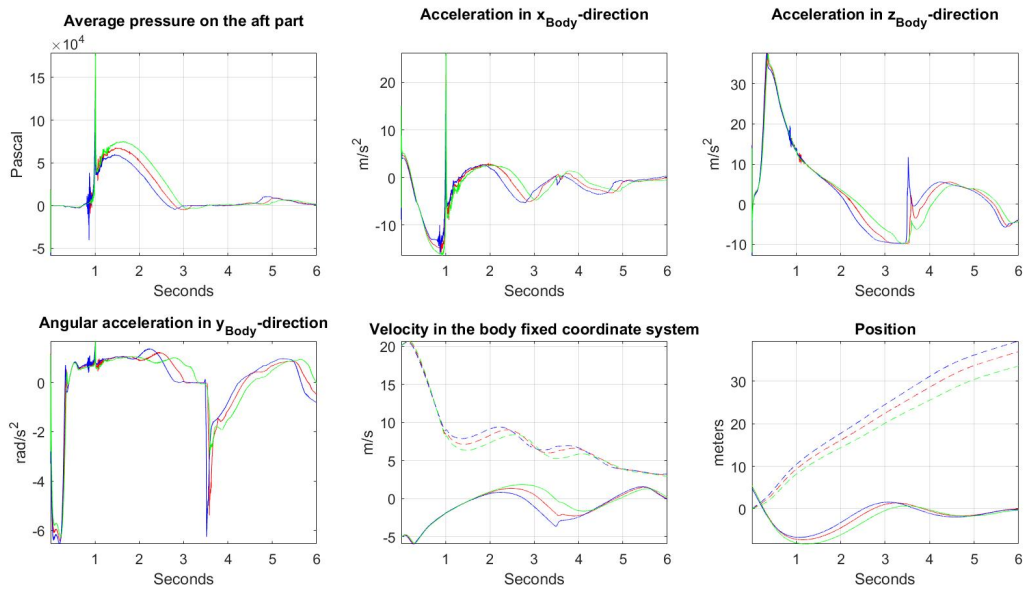

Figure 7.2: Plots of the results with different water entry angles, where blue is 55°, red is 60° and green is 65°. The accelerations and velocities are taken in the body fixed coordinate system. The dashed lines are in the x-direction, and the solid lines are in the z-direction for the velocity and position plots.

	55 DEGREES	INITIAL CONDITION	65 DEGREES
CAVITY CLOSURE TIME (PEAK) [s]	1.004	1.009	1.012
WATER EXIT TIME [s]	2.515	2.730	3.104
POP-UP HEIGHT [m]	1.542	1.369	0.657
MAXIMUM SUBMERSION [m]	-6.723	-7.297	-8.290
SAILING DISTANCE AT 6 s [m]	39.482	36.969	33.608
VELOCITY x_{Body} AT 6 s [m/s]	3.237	3.109	2.941
ACCELERATION PEAK MAGNITUDE [m/s^2]	18.511	21.678	26.194
MAX PRESSURE AFTER CAVITY CLOSURE [kN/m^2]	60.040	67.460	75.290

Table 7.3: Distinctive values for comparison for a change in water entry angle

The motion plot in Figure 7.2 shows that maximum submergence increases with increasing water entry angle. This is logical since the velocity is constant in the x_{body}- and z_{body}-direction, hence the body gets an increased initial velocity contribution in the vertical direction, in combination with small differences in angular acceleration. The maximum submergence is an important parameter, as discussed above and highly influenced by the water entry angle. Thus, the water entry angle is a crucial parameter. The smallest water entry angle gives the shortest submerged time and the highest body fixed velocity in x-direction at water exit. The contribution to counter clockwise rotation in the submerge phase seems to be independent of the three tested water entry angles. Hence, the case with the lowest water entry angle gives the highest water exit angle. Thus, an increase in pop-up height with decreasing water entry angle. The high exit velocity also leads to the longest sailing distance in global x-direction. The velocity is positive after 6 s for all the cases. It is most positive for the smallest water entry angle, as the decreasing rate is approximately equal for the three cases after second impact. The maximum pressure occurs just after the point of maximum submergence, where the hydrostatical pressure is at maximum. The case with water entry angle of 65° have the deepest maximum submergence point, and will also experience the highest pressure on the aft part.

a) b)

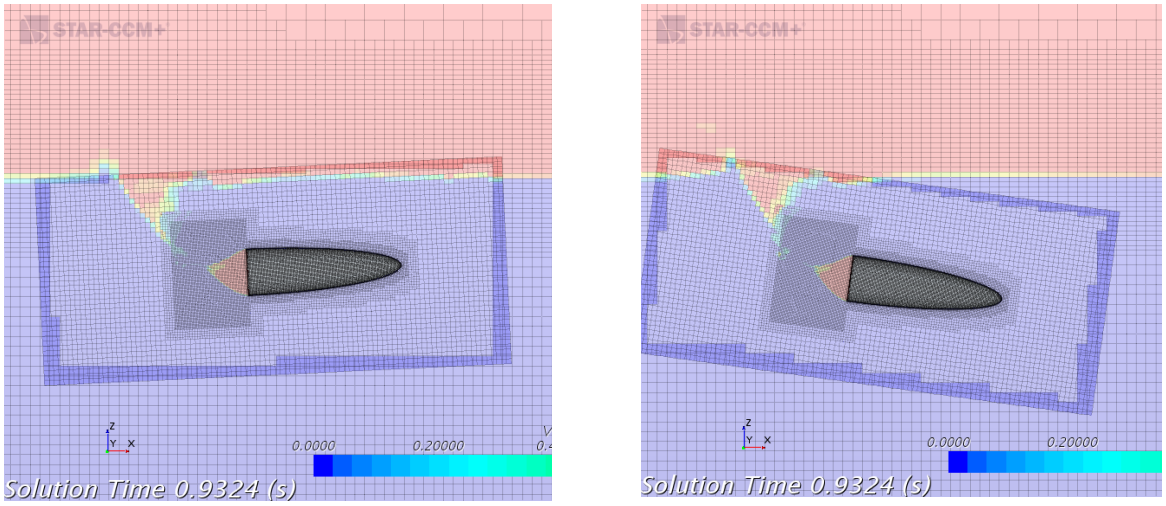

Figure 7.3: a) shows a picture of water entry angle 55° and b) shows a picture of water entry angle 65° at 0.9324s

The beginning of the air cavity closure can be seen from Figure 7.3, the time of the peak can be seen from Table 7.3. The VOF-pictures shows that case a) has started turning upwards, while case b) continues to decent.

7.3 COG

As earlier mentioned, the COG will be affected by the number of passengers and their seating arrangement. Three different values of COG in z-axis has been tested to see how the change in COG affects the behaviour of the free-falling lifeboat. The values are -0.3 m, -0.5 m and -0.7 m measure from the symmetrical centre line of the body.

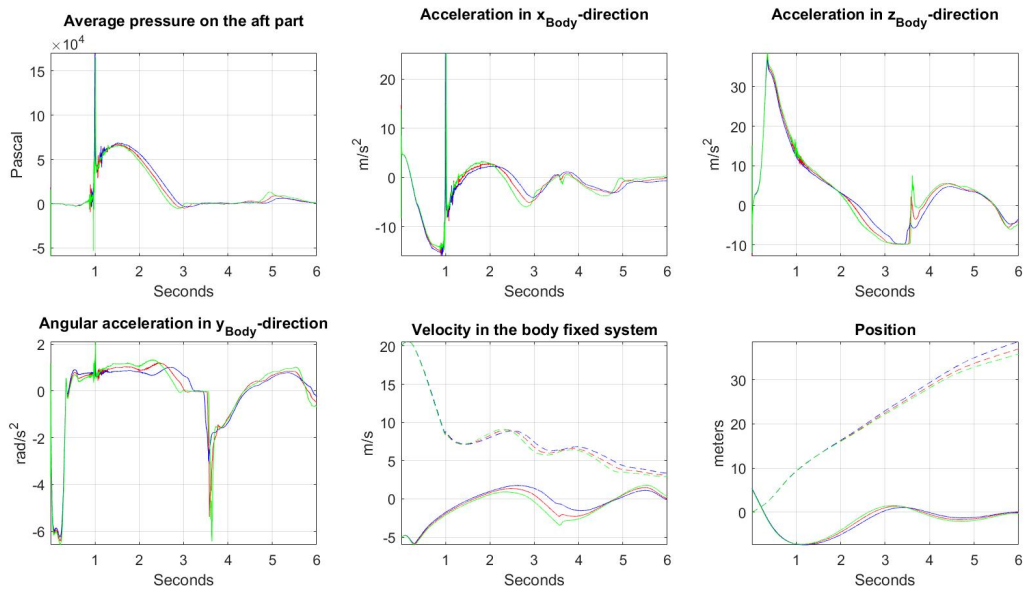

Figure 7.4: Result plots with different centre of gravity in z-direction, where blue is -0.3m, red is -0.5m and green is -0.7m. The accelerations and velocities are taken in the body fixed coordinate system. The dashed lines are in the x-direction, and the solid lines are in the z-direction for the velocity and position plots.

	-0.3 m	**INITIAL CONDITION**	**-0.7 m**
CAVITY CLOSURE TIME (PEAK) [s]	0.999	1.009	1.012
WATER EXIT TIME [s]	2.907	2.730	2.620
POP-UP HEIGHT [m]	1.083	1.369	1.516
MAXIMUM SUBMERSION [m]	-7.381	-7.297	-7.245
SAILING DISTANCE AT 6 s [m]	38.637	36.969	35.816
VELOCITY x_{Body} AT 6 s [m/s]	3.352	3.109	2.938
ACCELERATION x_{Body} PEAK MAGNITUDE [m/s^2]	25.306	21.678	25.297
MAX PRESSURE AFTER CAVITY CLOSURE [kN/m^2]	68.980	67.460	66.270

Table 7.4: Distinctive values for comparison of a change in centre of gravity in z-direction

The motion plot in Figure 7.4 reveals that the deepest maximum submergence, and the highest pressure after cavity closure, occur when the COG_Z is moved upwards. However, the difference is relatively small between the different cases. When the COG_Z is moved upward, the gravity-buoyancy arm becomes relative smaller. This result in a small counter clockwise rotation contribution in the water entry and in the submerged phase to the point where the body lies horizontal in the water. After this point, the gravity-buoyancy arm will contribute to a clockwise rotation. The behaviour is the same when moving

the COG_Z downward, but the arm is now longer, and contributes to a larger counter clockwise rotation before taking the horizontal position. This leads to the highest water exit angle, despite that the gravity-buoyancy arm counteract this rotation in the ascent. The water exit speed is approximately the same for all three cases, thus the most negative COG_Z gives the highest pop-up height. The water exit occurs last, and with the lowest water exit angle, for the case with the least negative COG_Z. This case gives the longest sailing distance as it has the largest water exit velocity.

7.4 Conclusion/ Discussion for the parameter investigation

The results shows that changing the maximum initial velocity with $\pm$ 5 m/s has the largest effects on the behaviour of the body. It manifests as the highest and lowest values in the air cavity closure time, pop-up height, acceleration peak magnitude, horizontal sailing distance and velocity at 6 s. It also manifests as the least maximum submergence and earliest water exit time for the lowest and highest initial velocity, respectively. By changing the water entry angle with $\pm 5°$, it shows great effect in the maximum average aft pressure, as it also has the largest maximum submergence. The highest and lowest values in maximum submergence is found for the highest and lowest water entry angle, respectfully. The latest water exit time and deepest submergence is also found for the highest water entry angle. The rearrangement of the COG with $\pm$ 0.2 m in z_{body} gave smallest effects, the only significant difference was the angular accelerations and the pop-up height difference.

8 Literature and CFD simulations relevant for compressible air simulations

8.1 Mass spring system for an air cushion without damping

The following derivation is taken from (Faltinsen & Timokha, 2009), where an air pocket is trapped at a tank corner as a result of the surface impacting geometry. Though this air cushion is not like the air cavity entrapped behind the lifeboat, the phenomena is quite similar and can be related with the same physics in terms of boundary conditions and assumptions.

8.1.1 Boundary conditions and assumptions

- The tank surface is assumed rigid

- Gas is considered compressible

- Spatial constant pressure within the gas cushion

- Thin gas cushion so the problem can be linearized

- No heat exchange

- The changing volume of the gas cushion can be described by potential flow theory of an incompressible fluid

- Pressure is continuous on the interface between the gas and liquid.

- The incident flow is assumed known

- The tank has only forced horizontal velocities

- The incident impacting free surface is assumed to have a time dependent vertical velocity, V(t) that is uniform in space

- The dynamic pressure in the air cushion is equal to the hydrodynamic pressure at the boundary of the air cushion.

- Surface tension is neglected

Resulting in the following three unknowns:

1) The dynamic gas density
2) The dynamic gas pressure
3) The velocity potential of the liquid flow

Three unknowns require at least three equations which are the following

1) The mass continuity for the gas cushion
2) A relationship between the gas pressure and the gas density
3) Laplace equation with boundary conditions for the velocity potential

8.1.2 Local coordinate system

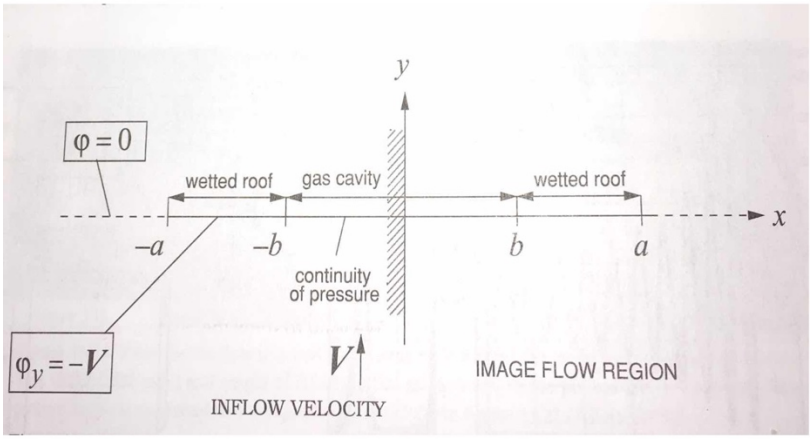

Figure 8.1: Coordinate system used in the derivation of natural frequency for a gas cavity (Faltinsen & Timokha, 2009)

A local coordinate system is placed with origin at the corner between the tank wall and tank roof in the impact region, and y is positive upward. Seen from the Figure 8.1, the wetted part of the roof is

represented from –a to –b. The incident impacting free surface is assumed to have a time dependent vertical velocity $V(t)$, which is uniform in space for the analysis. As a result of this, the velocity potential is equal to Vy. The tank wall at the opposite side of the impact area is assumed far away compared to the length of the impact area. Therefore, the tank bottom and the opposite tank wall can be assumed to be infinity in the analysis. The boundary condition for the wall adjacent to the impact area is taken into consideration by mirroring the flow about the tank wall. The boundary condition on the cavity surface and the free surface outside the impact are transferred to the x axis, which satisfies the dynamic free surface condition under the assumptions that the fluid accelerations are much greater than the gravity acceleration. Hence, $\phi = 0$ for $x < -a$. Modelling the liquid flow by a distribution of potential flow vortices on y =0, between $-a < x < a$. The vortex distribution causes only a vertical velocity outside the interval, satisfying the dynamic free surface condition, since the velocity potential is constant on y=0. The wetted tank roof has the velocity potential $\phi + Vy$. Therefore, $\frac{\partial \phi}{\partial y} = -V$, to ensure that there is no flow through the wetted tank roof and the vertical velocity v acting on the gas cavity is unknown.

The notation $u_{\pm}$ and $v_{\pm}$ were used for the values of the horizontal and vertical velocities u and v for $-a \leq x \leq a$ at $y = 0+$ and $y = 0-$, respectively. The velocities, $u_{\pm}$ and $v_{\pm}$ along the air cushion and tank roof are then expressed as

$$v_{\pm} = -\frac{1}{2\pi} * PV \int_{-a}^{a} \frac{\gamma(\xi)}{\xi - x} d\xi \qquad [\,38\,]$$

$$u_{\pm}(x) = \frac{1}{2} * \gamma(x)$$

PV denotes a principal value integral having a singularity when $\xi = x$. γ is the vortex density. The consequence of describing equation [38] like this, is that $v_{+} = v_{-}$. Hence, the subscript $\pm$ is unnecessary. For the solution to be unique, additional conditions must be applied, where the requirement is that $u_{\pm}(x) = -u_{\pm}(-x)$, meaning that the horizontal velocity is antisymmetric with respect to $x = 0$.

8.1.3 Natural frequency for a gas cavity

The compressibility of the gas causes a natural frequency, where resonant oscillations of the gas cushion are excited during impact. This result in an oscillating pressure for the gas cushion with the same frequency as the natural frequency of the gas pocket. To see the complete picture and all the detail in this lengthy derivation of the expression for the natural frequency, σ_n See (Faltinsen & Timokha, 2009). The main steps and basic understanding of this derivation are shown below.

An expression for the velocity potential on the cavity surface, ϕ_{cav} can be found by integration of $\frac{\partial \phi}{\partial x} = \frac{1}{2} * \gamma(x)$ using the free surface condition $\phi = 0$, then

$$\phi_{cav} = C(t) * \int_{-a}^{-b} \frac{dx}{\sqrt{a^2 - x^2} * \sqrt{x^2 - b^2}} = \frac{C(t)}{a} * K\left[\sqrt{1 - \left(\frac{b}{a}\right)^2}\right] \qquad [39]$$

Where $K(\theta) = \int_0^1 \left((1 - x^2) * (1 - \theta^2 * x^2)\right)^{-\frac{1}{2}}\, dx$ is the complete elliptic integral of first order, defined by (Gradstein & Ryzhik, 1965). The relation between the air cushion length and the wetted length in the tank, $\left(\frac{b}{a}\right)$, can be seen from Figure 8.1

Due to linear theory, the dynamic pressure in the cavity, $p_d =$, where ρ_l is the liquid density. $-\rho_{l*} \frac{\partial \phi_{cav}}{\partial t}$

The relationship between the gas pressure and the gas density can be described by an adiabatic process due to the assumption of no heat exchange.

$$\frac{p_{gas}}{p_0} = \left(\frac{\rho_{gas}}{\rho_0}\right)^k \qquad [40]$$

Where k is 1,4 for diatomic gas and equal the specific ratio of heat The pressure in the air cushion, $p_{gas} = p_0 + p_d$ and the density, in the air cushion, $\rho_{gas=\rho_0+\rho_d}$ where p_0 and ρ_0 is the initial pressure and density at gas pocket creation.

A Taylor expansion of equation [40] gives the relation between the gas density and initial density at creation

$$\frac{p_{gas}}{p_0} = 1 + \frac{p_d}{kp_o} \qquad [\,41\,]$$

Due to no inflow or leakage from the gas pocket, the continuity can be written as

$$p_{gas} * \dot{\Omega} + \frac{d\rho_{gas}}{dt} * \Omega = 0 \qquad [\,42\,]$$

where $\dot{\Omega}$ is the time rate of change of the cushion volume Ω. Linearizing equation [42] and inserting for equation [41], the continuity is then described by equation [43].

$$p_0 * \dot{\Omega} + \frac{\rho_0}{kp_0} * \frac{dp_D}{dt} * \Omega_0 = 0 \qquad [\,43\,]$$

The last steps consist of defining an expression for $\dot{\Omega}$, in addition to introduce a new variable, $C_1(t)$ representing the velocity potential obtain in equation [39] expedient.

The dynamic pressure in the cavity, p_d is then equal to $-\rho_l * \dot{C}_1(t)$. Finally, by assuming that $C_1(t)$has the harmonic time dependence $\exp(i\sigma_n t)$, the undamped natural frequency of the gas cushion given in radians/second, σ_n reads

$$\sigma_n \left(= \frac{K\left(\frac{b}{a}\right) * k p_0}{K\left(\sqrt{1-\left(\frac{b}{a}\right)^2}\right) * \Omega_0 * \rho_l} \right)^{\frac{1}{2}} = \left(\frac{K\left(\frac{b}{a}\right) * p_0}{K\left(\sqrt{1-\left(\frac{b}{a}\right)^2}\right) * \rho_l} \right)^{\frac{1}{2}} * \sqrt{\frac{k}{\Omega_0}} \qquad [\ 44\ ]$$

The most important discovery regarding equation [44] is that the natural frequency of the air cushion is invers proportional to the square root of the initial cushion volume, Ω_0.

8.2 Previous CFD simulations relevant for lifeboat diving

Andreas Ommundsen did a hydrodynamic study of the air cavity dynamics connected with free falling lifeboats. In order to resemble the cross section cut of the bow part of a lifeboat, a wedge with dead rise angle of 30 degrees was the chosen geometry. Ommundsen conducted CFD simulation with both incompressible and compressible air. Thereafter, he did comparisons with experiments conducted by Wang and Luigi, using the same geometry and initial conditions as in their experiment. Ommundsen conducted all simulations with VOF as the interface capturing technique, Segregated solver, RANS with $k - \varepsilon$ turbulence model and 1. Order temporal discretization. It should be noted that he did all the simulations in two dimensions, though he has a chapter showing the small influence of 3D effects. The different compressible methods applied, are explained more in detail in section 0. Ommundsen found out that the natural frequency of the air cavity was constantly under predicted in the CFD analysis compared to experimental results, where the adiabatic process gave the highest natural frequency. The natural frequencies were obtained from a Fast Fourier transform. The incompressible model had no pressure oscillations.

a)

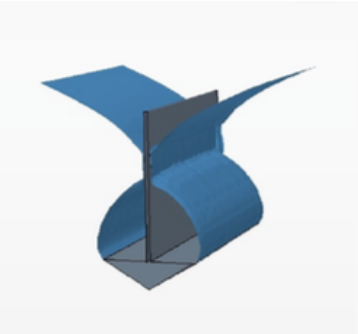

b)

Case	*Natural frequency (FFT)*	*Percentage of experimental value*
Experiment	29,30 Hz	100
Incompressible	—	—
Ideal gas	21,48 Hz	73
Adiabatic – $k = \gamma$	24,42 Hz	83
Polytropic – $k = 1{,}375$	23,44 Hz	80

Figure 8.2: a) Illustration of the wedge geometry used in Ommundsens CFD analysis and experiments. b) represent the natural frequencies Ommundsen found from the corresponding CFD analysis. The natural frequency obatained from experiment is found by Wang. (Ommundsen, 2014)

Inspired by Ommundsen discoveries, Vidar Tregde did comparisons of full scale lifeboat and 3D CFD simulations in his paper "compressible air effects in CFD simulations of free fall lifeboat drop". Tregde used the geometry of an actual lifeboat design, including a wheel house with only some simplification to ease the meshing. Therefore, an air cavity was also present behind the wheel house. Figure 8.3 below, indicates pressure oscillations in this part for all the compressible air simulations and the full-scale experiment he conducted.

a)

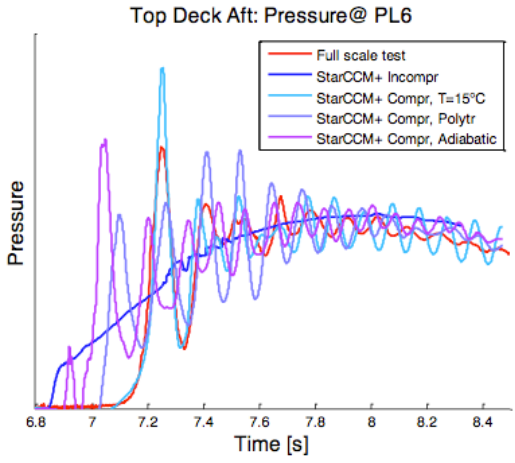

b)

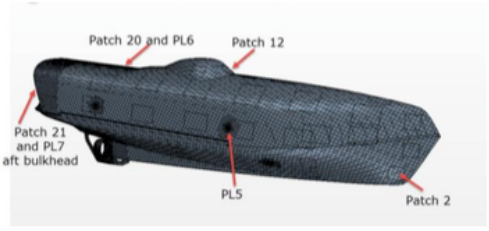

Figure 8.3: a) Comparison of full scale experiments and CFD for pressure probes behind the wheelhouase, shown as patch 20 and PL6 in figure2b (Tregde, 2015).

Tregde conducted all simulations with the same interface capturing technique, turbulence model, time scheme and compressible air relations as Ommundsen. Tregde found out that the Isothermal condition represented the right time of pressure peak, though the peak was overestimated with approximately 25%. In addition, the relative damping was much lower than the value obtained from the experiments. The polytrophic relation failed to model the time of the pressure peak correctly, but the relative damping was very similar. The adiabatic failed to model the damping sufficiently, though it was closer to the experiment compared to the isothermal. The pressure peak was also observed significantly earlier for the adiabatic model. The simulations were conducted with three different models for the compressible air. These relations, and how to implement them on Star, will be shown in detail later.

9 Compressibility of air relations in Star CCM+

There are various ways to model the air as compressible for the software, Star-CCM+. Since the interface capturing technique of choice has been VOF, as previously described the concept of in 3.3.2.1, the amount of compressibility of air options narrows significantly. The settings in Star used for the simulations regarding incompressible air, were carefully selected through trials and error, and a lot of research. Therefore, the same settings have been used when modelling the air as compressible, with only some few necessary changes.

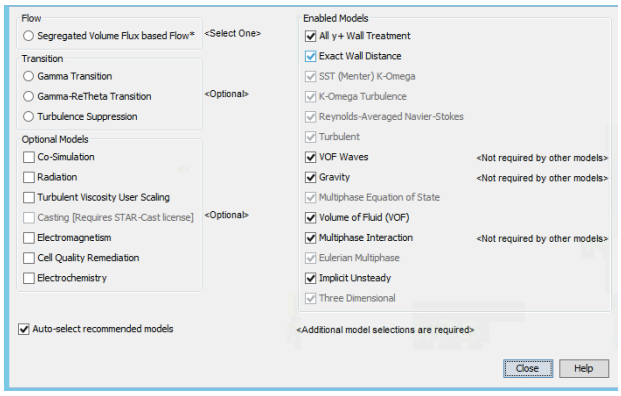

Figure 9.1: All the models that are kept the same for all the simulations

In the Eularian multiphase model for air, the constant density node selected in the PO were changed to "ideal gas". The only compatible solver for ideal gas, using VOF, was the "segregated volume flux based flow" as seen from Figure 9.1. There are three fluid energy models of choice when modelling the fluid energy using a segregated approach. These are:

-Segregated fluid enthalpy

- Segregated fluid temperature

- Segregated fluid isothermal

The segregated fluid enthalpy solves the total energy equation, where the chemical thermal enthalpy is the solved variable. According to Star-CCM+ user guide this model is recommended for any simulations involving combustion. Since combustion is not relevant in lifeboat diving, this model is not of interest. Segregated fluid temperature model solves the total energy equation with temperature as the solved variable. In contrast to the Segregated fluid enthalpy, Star-CCM+ user guide states that this model is

appropriate for simulations not involving combustion. The main drawback is that it is computational expensive to solve the energy equation with varying temperature. No simulations have been conducted for this method, though it might be an appropriate solver for the problem in question. The segregated fluid isothermal keeps the temperature in the continuum constant. The density of air is then computed by the ideal gas law

$$\rho_{air} = \frac{p_{abs}}{RT} \qquad [45]$$

Where p_{abs} is equal to the absolute pressure in the fluid. The specific gas constant, $R = \frac{R_u}{M}$, where R_u is the universal gas constant, equal to 81314.4621 $\mathrm{J/kmol} * \mathrm{K}$. M is the molecular weight, where the custom value for air in Star-CCM+ has been used and is equal to 28.9664 $kg/kmol$. T is the temperature measured in Kelvin, and is kept constant for this model. The segregated fluid isothermal method has been conducted for a constant temperature of 15℃, and is referred to as the Isothermal condition, which was also used as one of the compressible models by Tregde.

9.1 Adiabatic Relation

A procedure followed by Faltinsen, described in 8.1.3,where no heat exchange were assumed for the air cushion, meaning that the density in the air cushion could be related through equation [40]. Though Faltinsen e.t al used this relation to determine the density variation in the air cushion in a tank as a result of slamming, similar approach might be appropriate for the density calculations of the air cavity entrapped behind the lifeboat.

$$\frac{p_{cavity}}{p_0} = \left(\frac{\rho_{cavity}}{\rho_0}\right)^k \qquad [46]$$

Where p_{cavity} and ρ_{cavity} is the pressure and mass density in the air cavity and p_0 and ρ_0 is the pressure and density at the initial time of cavity creation. The adiabatic gas relation, is not a model that Star-CCM+ provide. Therefore, this relation had to be implemented manually by user defined field

functions. This have been done previously by Tregde and Ommundsen with satisfactory results. Instead of selecting the node “ideal gas”, the “User defined EOS is applied” in Figure 9.2

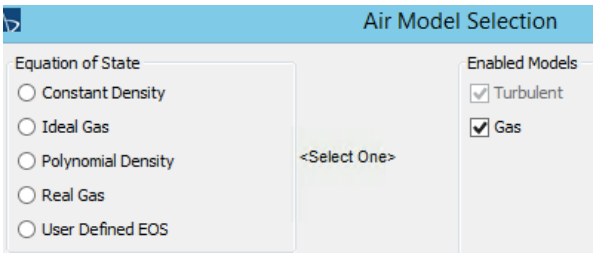

Figure 9.2 Models for air in the Eularian multiphase

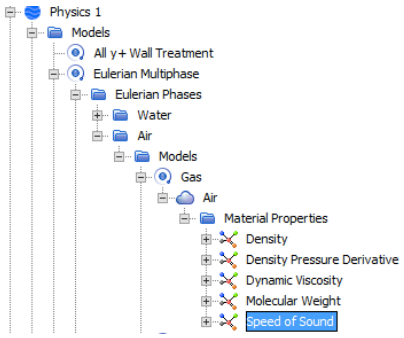

Figure 9.3 Material properties for air

The consequence of choosing user defined EOS is that an addition definition of the density pressure derivative must be applied for the material properties of air. Reformulation of equation [46], where the density is the solved variable:

$$\rho_{air} = \left(\frac{p_{air}}{p_0}\right)^{\frac{1}{k}} * \rho_0 \qquad [\,47\,]$$

$$\frac{\partial \rho_{air}}{\partial p_{air}} = \frac{\rho_0}{k * p_0} * \left(\frac{p_{air}}{p_0}\right)^{\frac{1}{k}-1} \quad [48]$$

Equation [47] and [48] are implemented as field functions written in C programing language, for the density and density pressure derivative shown in Figure 9.3. The absolute pressure solved within each cell by the software is inserted for p_{air} . It is assumed that the standard atmospheric values used in StarCCM+ for the pressure and density are equal to the pressure and density of the air at initiation of cavity creation. Therefore, p_0 and ρ_0, are set to 101325$\frac{N}{m^2}$ and 1.18415 $\frac{kg}{m^3}$, respectively. The ratio of specific heat, k is set to 1.4, since diatomic gases such as air, is equal to 1.4 for an adiabatic process. The simulations following this procedure is referred to as the adiabatic process, which has also been used by Tregde and Ommundsen.

Abrahamsen found out through experiments of sloshing in a rigid tank (when doing his Phd), that the heat exchange from an air cushion contribute to the decay of the pressure oscillations. For all of his air pockets, the polytrophic index, k, was found to be between $1.36 \leq k \leq 1.39$ (which is close to the ratio of specific heat for an adiabatic process). Hence, an adiabatic process might be inaccurate assumption (Abrahamsen, 2011). Therefore, an additional compressibility of air relation have been conducted, only changing the ratio of specific heat to $k = 1.375$ and using the same field functions obtained from equation [47] and [48]. This method is referred to as the polytrophic gas relation, and is the same relation as Tregde and Ommundsen used.

10 Preparing the simulation

An explanation of the mesh configuration with corresponding prism layer and boundary condition are explained earlier in 4.2. In addition, a sensitivity and convergence analysis were conducted. Since the air is modelled as compressible, other problems arises and new justifications are needed.

10.1 Mesh configuration and turbulence model

The mesh configuration used for the incompressible fluid simulations conducted in collaboration with Simen Groth and Vegard Netland have been used for the case of compressible air as well. Seen from Figure 6.1, the mesh refinement region, where the smallest cells are located, are fully capturing the air cavity. Therefore, no alterations have been made. This includes also the prism layer for the various mesh discretization's. The same turbulence model, and corresponding y^+ model selected in 3.3.3 are applied.

10.2 Sensitivity analysis

At first, there were no way to determine an appropriate time step for the simulations. This was due to the fact that all the simulations with a second order temporal discretization diverged after initial water impact. Very low time steps were applied combined with an increase of inner iteration by 30. Unfortunately, this got me nowhere. The time scheme was then changed to 1. Order temporal discretization and the simulations started to run smoothly. The First order temporal discretization, discretizes the unsteady term using the solution at the current time level and the previous time step. The second order temporal scheme obtain a solution of the unsteady term at the current time step as well as the solution for the previous two time steps. (Steve CD adapco, 2016)

To the authors knowledge, there has not been conducted simulations of life boat diving with Eularian multiphase, using a segregated solver, VOF and 2. Order temporal discretization. Both Ommundsen and Tregde used a 1. Order temporal discretization, described in "Previous CFD simulations relevant for lifeboat diving". Tregde did comparisons of lifeboat diving experiments in full scale and CFD analysis with satisfactory agreement for the compressible models. Therefore, a first order temporal discretization has been assumed valid. Figure X is a superimposed plot of accelerations in z_{body} and

x_{body} for an incompressible simulation with first and second order temporal discretization. The simulations are very similar when air is modelled as incompressible, which does not have to be the case when air is modelled as compressible.

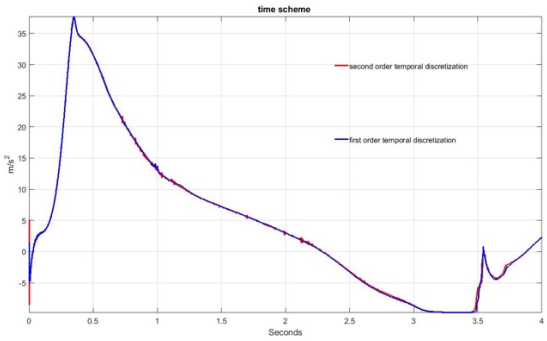

Figure 10.1:Acceleration in z_{body} direction for first (blue) and second(red) order time scheme

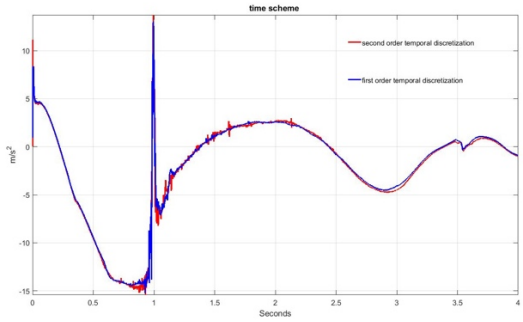

Figure 10.2: Acceleration in x_{body} direction for first (blue) and second(red) order time scheme

10.2.1 Iterations and time step

An investigation of the influence of time step and inner iterations is conducted for the coarsest grid discretization, x_3, to save computational time. For each iteration, the Navier-stokes equation, Continuity equation and the volume fractions are solved. More details about iteration, and how the amount of them within each time step influence the residuals obtained from Star-CCM+ are described more in detail in the PO. From the figure below, the residuals do not seem to converge after 10 iterations, which was the case when air was modelled as incompressible. The simulation time, chosen to investigate the appropriate number of iterations, is taken at approximately 0.4 s, where problems related to the turbulence model occurred for the incompressible case. Seen from Figure 10.3, the Continuity equation needs additional iteration to converge, compared to the incompressible. The continuity seems to flatten out after approximately 25 iterations. Therefore, 25 iteration have been applied for all the compressible air models conducted. In comparison, Tregde increased the number of iteration from 6 to 20 in the transition from incompressible to compressible air.

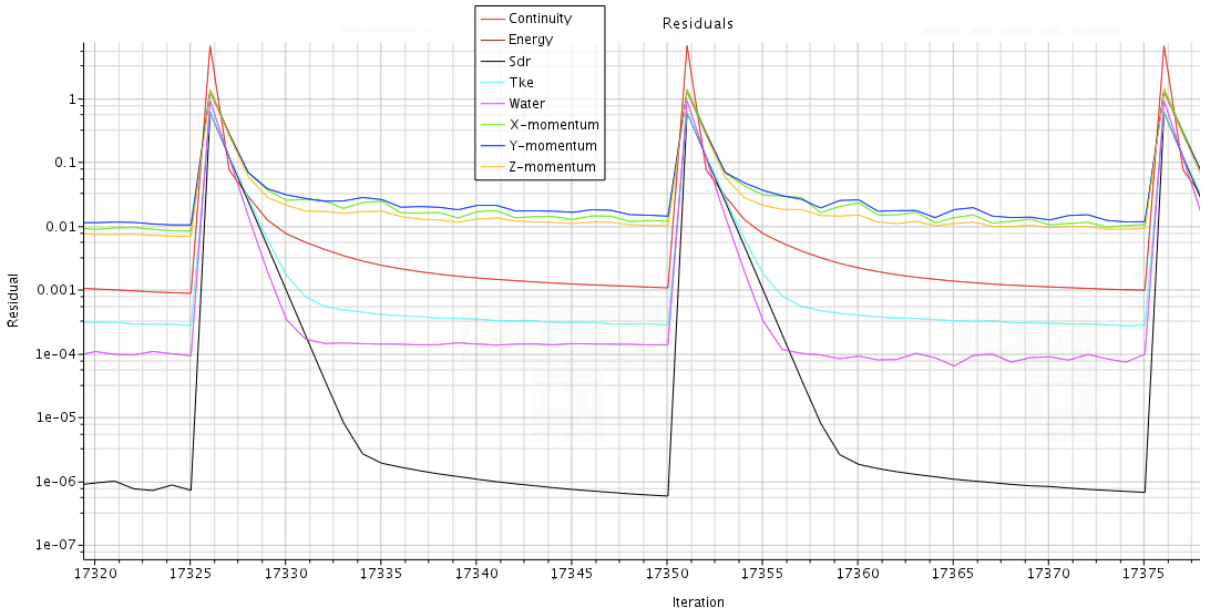

Figure 10.3 The Residuals for the coarsest grid with a time step of 0.0006seconds and 25 iterations for isothermal condition

11 Error sources

For the sake of getting an accurate interpretation of the results obtained from both the simulations conducted with incompressible and compressible air, the uncertainties and sources of error influencing the accuracy is important to take into consideration.

11.1 Segregated flow solver

The segregated flow solver is applied for both compressible and incompressible simulatiions. Mentioned in 4.4, the solver has its limitations for mildly compressible flow and high Mach numbers. For Mac numbers higher than 0.3, another solver is recommended (Steve CD adapco, 2016).

The speed of sound is much lower in a liquid gas mixture compared to only gas and liquid. The speed of sound is about 1440-1480 m/s and around 340 m/s for water and air, respectively, but can fall to approximately 20 m/s for an air-water mixture. The significantly drop in speed of sound, is a combination of the fact that the two phases are easily compressed due to the presence of air, but relative dens because of the dominant mas of the liquid. This influences the fluids ability to transmit a small disturbance like velocity. (McWilliam & Duggins, 1969) (Kieffer, 1977). Seen from Figure 11.1, velocities with a greater magnitude than approximately 10 m/s seems to be present in air phase mixtures. Hence, The Mach number is likely to exceed 0.3, further altering the accuracy of the solver.

a)

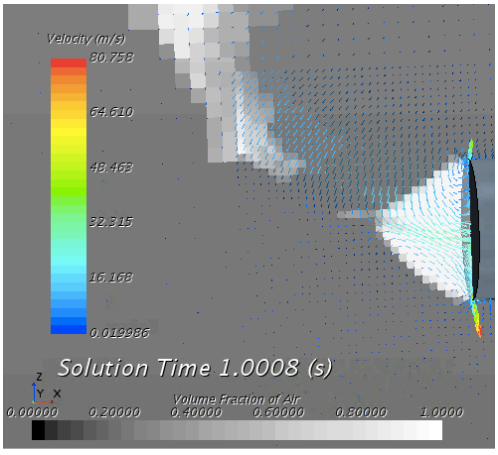

b)

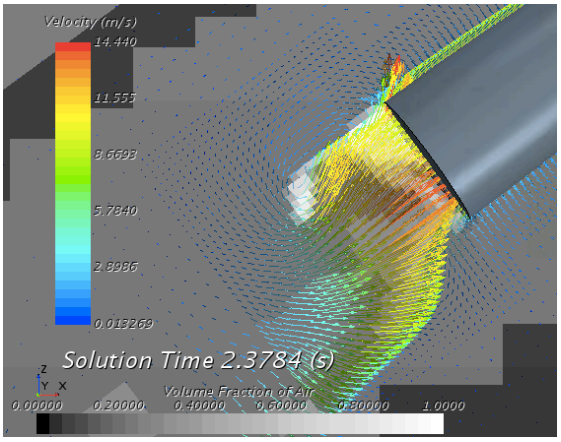

Figure 11.1: The fraction of air is shown in combination with velocity vectors shown for adiabatic relation. a) Time instant close to cavity closure. b) At the end of the submergence phase, where air-water mixtures still are present

11.2 CFL peaks and turbulence model

Problems related to solving the turbulence model occurred for the incompressible simulations. Mentioned in 5.1.3, rapid density changes in connection with sharp corners may cause unrealistic high accelerations. For this time instant, unrealistic high velocities directed outwards from the back of the lifeboat occurred (Figure 11.2). This explains the large local CFL, and might be the reason for the complications regarding the turbulence model.

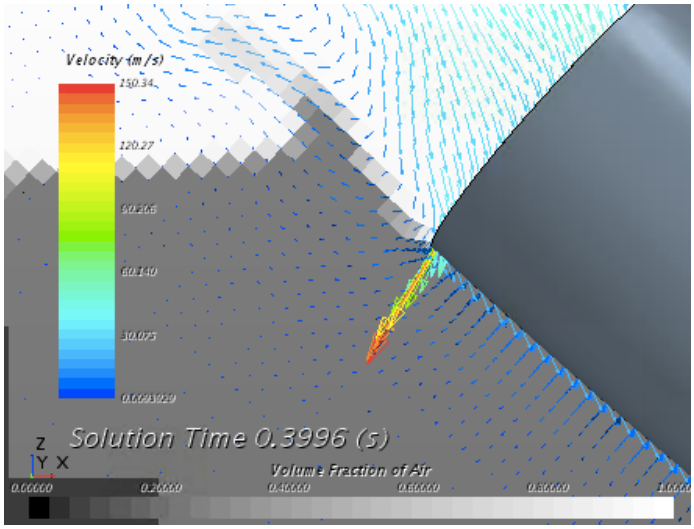

Figure 11.2: Velocity vectors measured relative to COG_{global} for an incompressible simulation after 0.4 seconds

The same turbulence and Y^+ model was selected for incompressible and compressible models. The Y^+ model was a hybrid version, appropriate for Y^+ varying between lower than 30 and above. Seen from Figure 11.3, the average value lays in the log-log layer (Y^+>30), where the high Y^+ model is an appropriate solver. However, the hybrid model was selected as a result of varying density in the simulation, resulting in large changes. Seen from Figure 11.3, values below 30 are present. As mentioned in the convergence study in 5.2 it is unknown how this code work in the transition from log layer to viscous sub layer and is therefore an uncertainty for all the simulations.

a)

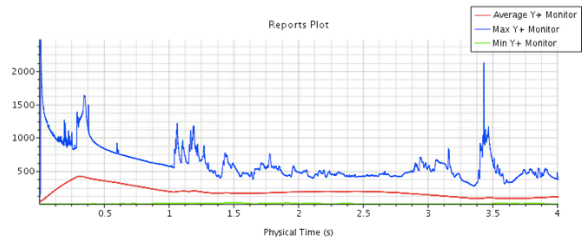

b)

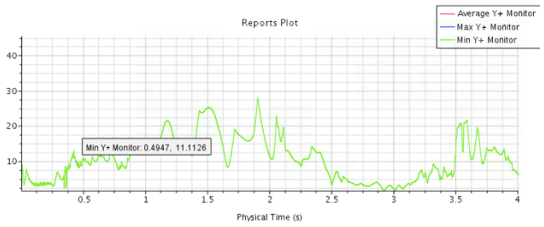

Figure 11.3: Y+ measured at the body hull, where figure b is zoomed in to see the low values

11.3 Spatial constant pressure

The pressure on the aft part of the body is calculated as an average pressure over this part. Faltinsen, et al. (2009) and Abrahamsen investigated pressure differences in air cushions due to slamming. They both stated that the assumption of spatial constant pressure was an accurate assumption, as a result of the uniform pressure measurements from the nodes in the tank. Seen from Figure 11.5, the pressure is uniformly distributed in the beginning of the pressure oscillations. However, the assumption of spatially constant pressure on the aft part later on when the entrapped air is starting to dissolve seems wrong. The pressure distribution in combination with fraction of air is highlighted at 2 seconds in Figure 11.4. It is difficult to see from the picture, but is seems that the entrapped air is not distributed over the whole surface, explaining the significant difference. The spatial pressure variations on the aft part were largest for the compressible model shown, in comparison of adiabatic and polytrophic. This could explain the more asymmetric pressure oscillations for Isothermal condition after three oscillations, compared to adiabatic process and polytrophic gas relation, seen in Figure 12.1.

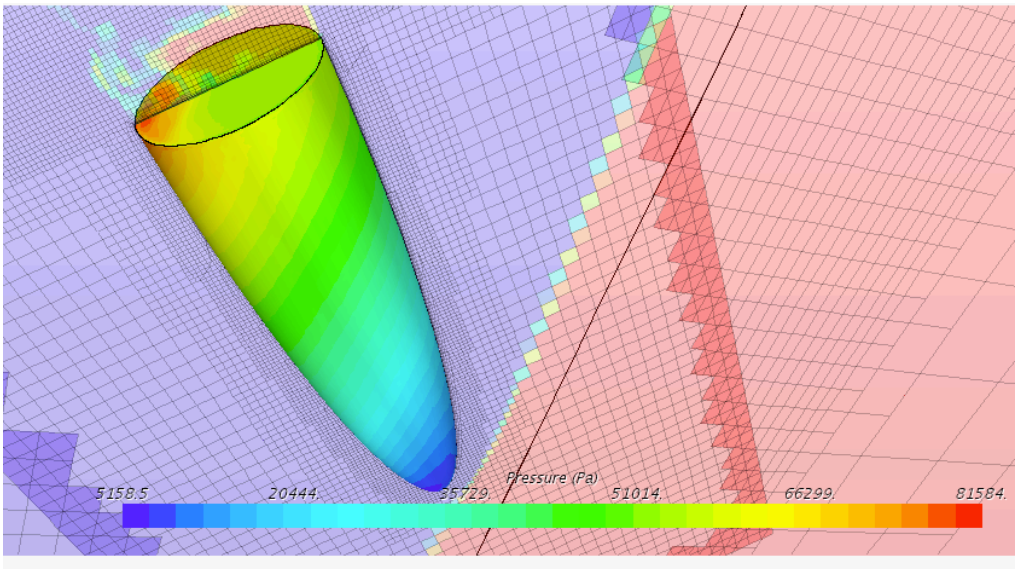

Figure 11.4: Pressure distribution and fraction of air for isothermal after 2 seconds

a)1.1s

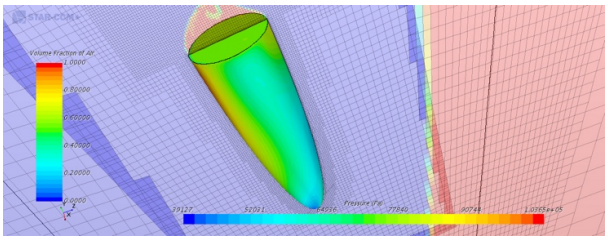

b)1.3s

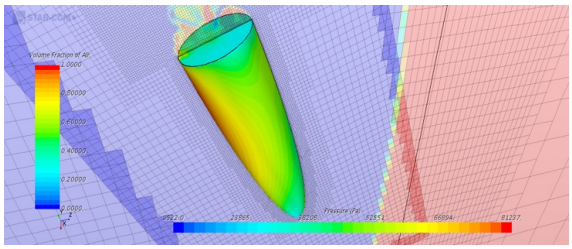

c)1.5s

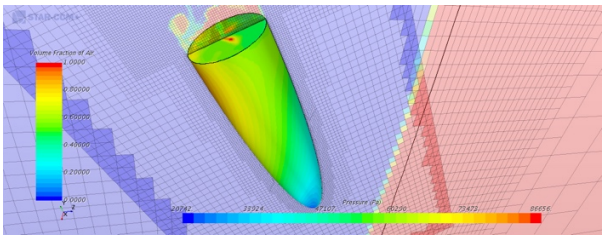

d)1.7s

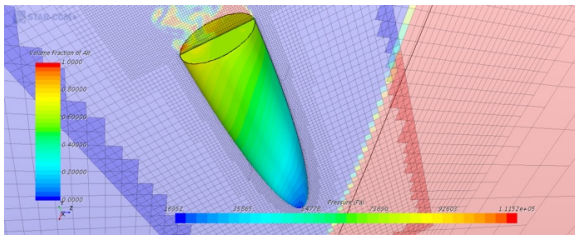

e)1.9s

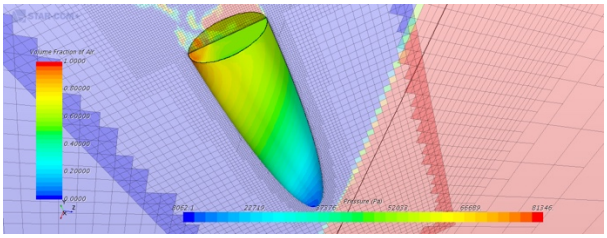

f)2.1s

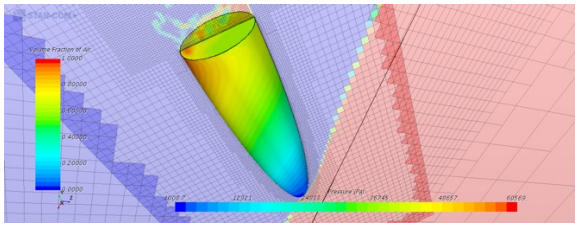

g)2.3s

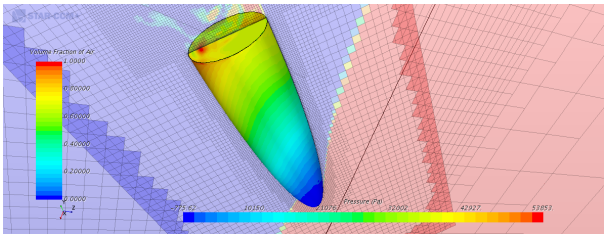

h)2.5s

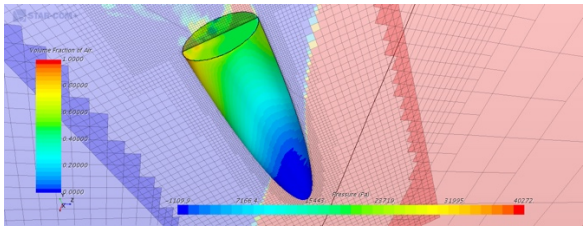

Figure 11.5: pressure distribution on the aft part of the hull from 1,1 to 2,5 seconds for isothermal condition.

11.4 Mesh configuration

A convergence study of the different mesh discretization's was conducted with incompressible air. The coarsest grid discretization might have been to coarse, influencing the physics in connection with life boat diving. The formula for order of accuracy was based on a log linear relationship between mesh discretization and an integrated quantity. Hence a too coarse mesh discretization, where different phenomena regarding the physics are simulated, will not follow this relationship.

12 Results

In this chapter, the influence of modeling the air as compressible compared to incompressible will be investigated. In addition, a comparison of the various air compressible models will be considered and compared with previous CFD simulations, experiments and parameters influencing the natural frequency. In addition, the damping ratio has been calculated.

12.1 Pressure

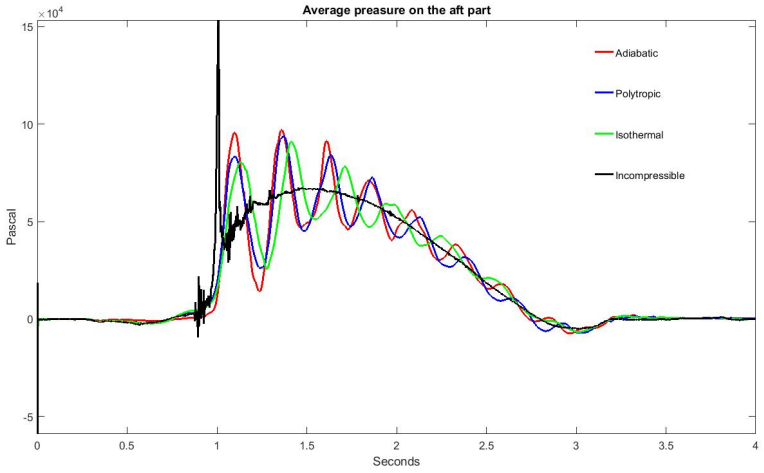

Figure 12.1 Comparison of the pressure oscillations measured on the aft part of the lifeboat

Seen from Figure 12.1, all the simulations get a pressure peak close to cavity closure. For the compressible models, the first peak appears approximately after 1.1 seconds and start to oscillate as the air cavity is varying in size. The pressure peak appears later when air is modelled as compressible compeered to incompressible (see Table 12.2). A reason for this might be that the cavity gets compressed when being entrapped by the surrounding water before it creates a positive acceleration on the aft part of the body in x_{body} direction. The unrealistic high pressure peak for the incompressible makes it difficult predicted the local pressure loads for this time instant. However, a filter cannot be applied since the pressure peak might contribute to local failure. Therefore, air should be modeled as compressible, to account for the local varying pressure.

The natural frequency for all the simulations are shown in Table 12.1. The natural frequency is varying from 3.5Hz to 4Hz for the compressible air models, while the incompressible run only has one pressure peak. The natural frequencies are significantly lower than the frequencies Tregde obtained for both CFD and full scale model tests. Since Tregdes pressure oscillations where due to the air entrapped behind the wheelhouse, the initial cavity volume is most likely much smaller in size, compared to the air cavity behind the aft of the life boat. According to equation [44], the natural frequency is invers proportional to the square root of the initial cavity volume. Hence a lower frequency is reasonable for this geometry. Tregde stated that the Isothermal condition predicted the time of pressure peak most satisfactory, but overestimated the amplitude. Seen from Figure 12.1 and Table 12.2, the first pressure peak for all the compressible air models are relatively close to each other, where the pressure peak for the isothermal condition occurs approximately 0.035seconds later than for the adiabatic process and polytrophic gas relation. The adiabatic process predicts the largest amplitude, where the polytrophic gas relation is significantly lower, but still a bit larger than for the isothermal condition. According to Abrahamsen, the heat exchange from an air cushion contributes to a decay of the pressure amplitude, which might then be neglected, when an adiabatic process is assumed. This might also be the case for the entrapped air behind the lifeboat, where the adiabatic process shows larger amplitudes due to the most likely under predicted damping. The polytrophic gas relation has a smaller pressure peak, which could imply that more energy from the entrapped air is being transferred to the surroundings, contributing to damping of the oscillations. However, varying hydrostatic pressure has not been subtracted. Therefore, a comparisons of these pressure peaks is not an accurate prediction of the damping. A thorough investigation of the damping will be conducted later in the results.

COMPRESSIBLE RELATION	**NATURAL FREQUENCY (FFT)**
ISOTHERMAL	3.50 Hz
ADIABATIC	4.00 Hz
POLYTROPHIC	3.75 Hz

INCOMPRESSIBLE	Undefined

Table 12.1: show the air compressible model used with corresponding natural frequency obtained from a Fast Fourier Transform

The natural frequency for the compressible air relations are found by a Fast Fourier Transform. The plot from Figure 12.2 shows a single sided amplitude spectrum, representing where the energy in the pressure plot is concentrated given by the frequency of the oscillations. The first peak is not a "real peak" as it just shows the lowest possible frequency for the given data. Since the data is obtained from a time series of 4seconds, this peak shows a maximum energy concentration for a frequency of exactly 0.25 Hz. Most energy will be concentrated around the second peak, representing then the natural frequency of the air cavity. For an adiabatic process, the natural frequency was found to be 4Hz, seen from Figure 12.2. The same procedure was followed, when the natural frequency for isothermal conditions and polytrophic gas relation was found, where the unreal peak at 0.25 Hz was not considered. From the derivation made by Faltinsen.et.al in section 8.1.3, the natural frequency for a gas cushion is proportional to the square root of the ratio of specific heat, k. Hence, a smaller natural frequency for the for the polytrophic gas relation compared to an adiabatic process is reasonable.

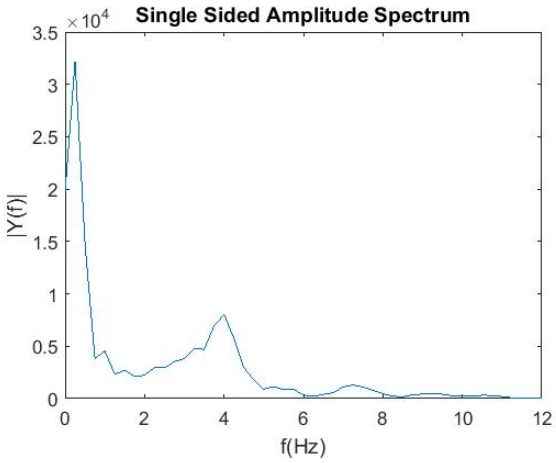

Figure 12.2: shows a single-handed Amplitude spectrum obtained from a FFT of the pressure on the aft part modelled for an adiabatic process

12.2 Acceleration

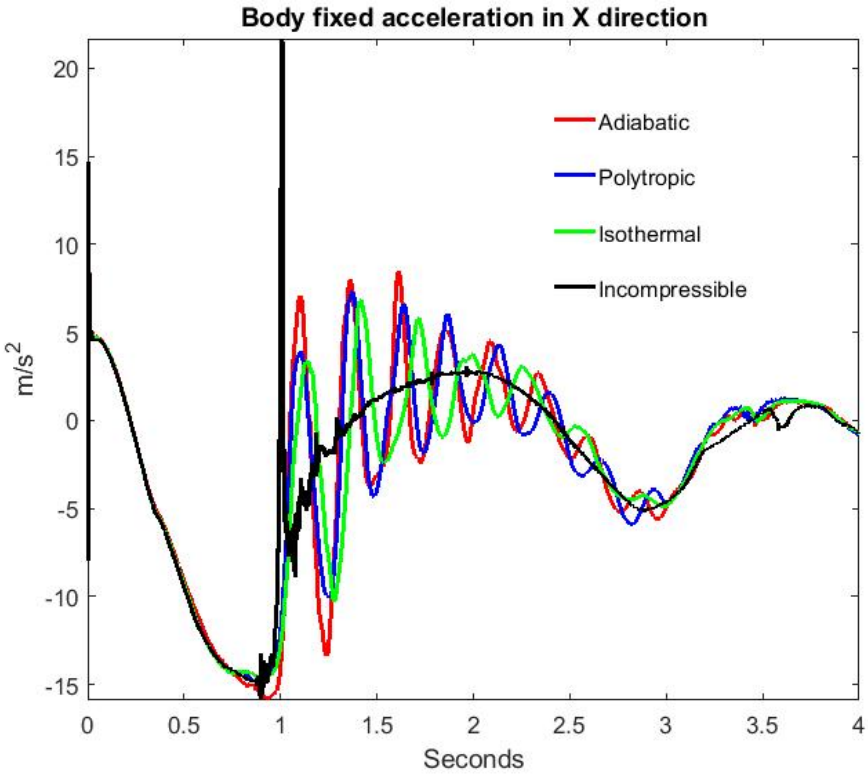

Figure 12.3 acceleration in x_{body} direction

When the air cavity closes, the surrounding water will create an impulse on the aft part of the body as the surrounding water squishes the entrapped air. The acceleration peaks are observed later for compressible models, probably due to the compression of the entrapped air before it creates a push in positive body fixed x direction. When the air cavity closes, two jets will be ejected, one outward and one inwards relative to the lifeboat. These water jets travel with large velocities and have unfortunately not been captured for by the 2D VOF pictures taken. The plot of the body fixed accelerations in x_{body} direction in Figure 12.3 is quite similar to the pressure plot, in Figure 12.1, where the accelerations peaks are present for the same time instant as the pressure peaks. This makes sense, since the pressure on the aft part of the body contributes to a positive acceleration, most pronounced in the body fixed x direction. When calculating CAR index, to cheek for safety and comfort for the occupants, a Butterworth fourth order is filter is used. This filter will attenuate the acceleration peak in x_{body} direction. Hence passenger safety might be calculated when air is assumed incompressible, though the oscillating acceleration in x_{body} direction will in fact influence the CAR index.

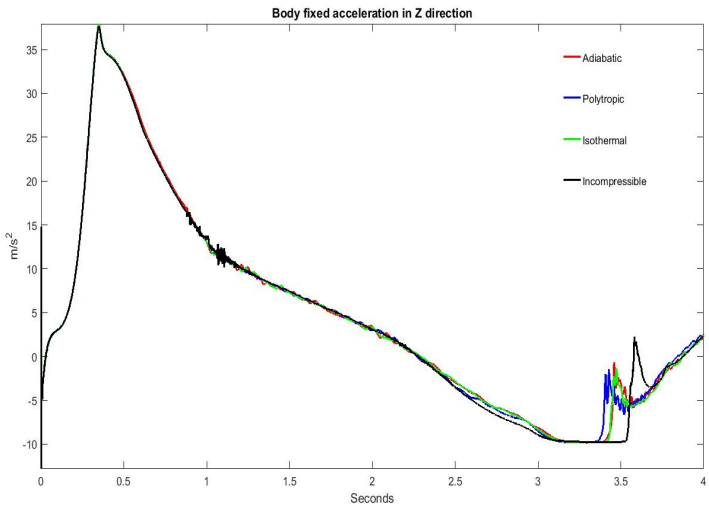

Figure 12.4: Acceleration in z_{body} direction

The body fixed accelerations in z direction is very similar to each other for all the models until approximately 3 seconds. Some disturbance is observed for the incompressible model around cavity closure, while all the compressible models show small oscillations after cavity closure, indicating that the pressure oscillations also influence the body fixed z acceleration. The second water entry appears quite different from each other, seen from Figure 12.4 and Figure 12.5. At approximately 3.4 seconds, the polytrophic model is effected by slamming forces, as the lifeboat hits the water a second time. The same happens for isothermal condition and adiabatic process almost instantaneously 0.05 seconds later, while it occurs additionally 0.15 seconds later for the incompressible model, shown in Table 12.2.

a) c)

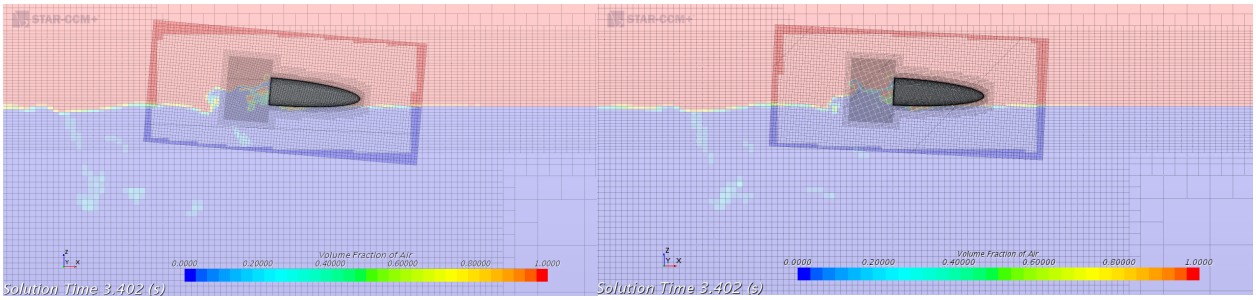

b) d)

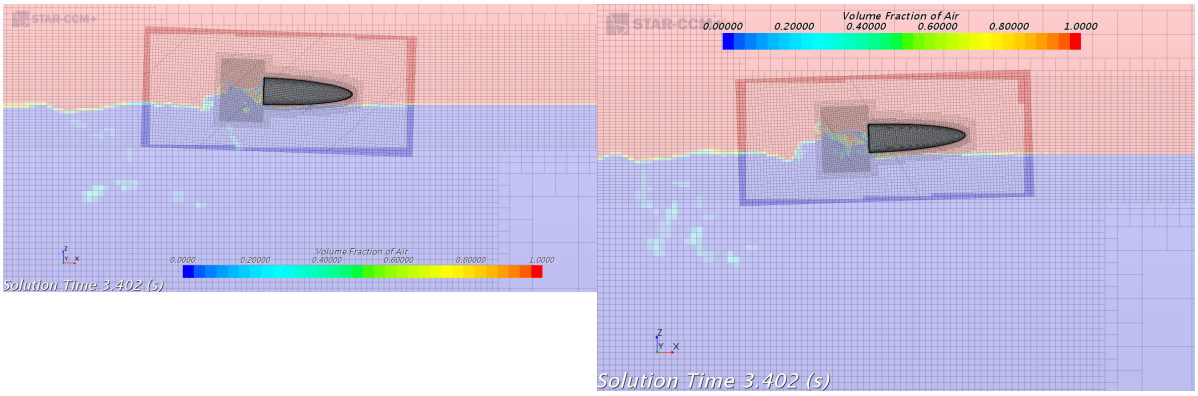

Figure 12.5: Vof picture after 3.402 seconds showing the different time of second water entry. A, b, c, d are polytrophic, adiabatic, isothermal and incompressible, respectively

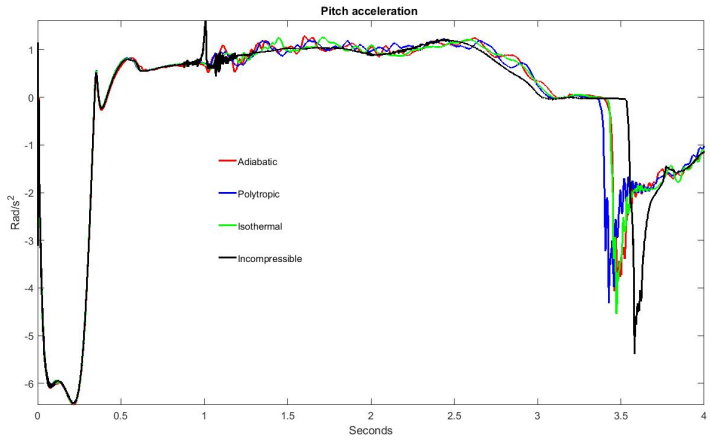

Figure 12.6 Pitch accelerations

The cavity closure also contributes to a pitch acceleration. As for the other accelerations mentioned, the incompressible case only consists of one peak, while the compressible models show oscillations. Seen from Figure 12.7, the asymmetric circulation/vortex shedding, seem to be more pronounced for the compressible models compared to the incompressible. This could explain the oscillating pitch accelerations for the compressible models and the small oscillations in body fixed z direction for the compressible models.

a) b)

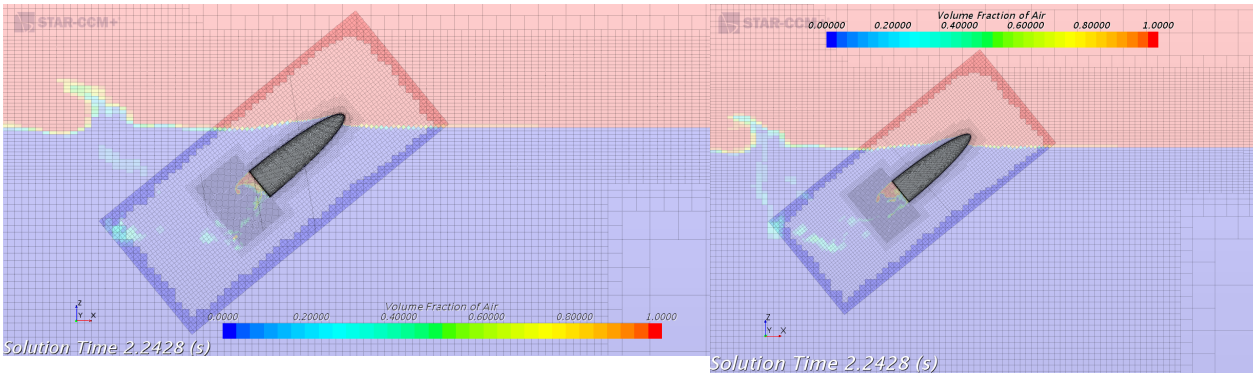

Figure 12.7: Comparison of the vortex shedding on the aft part of the body at 2.2428 seconds, where a) is adiabatic and b) is incompressible

12.3 Velocity

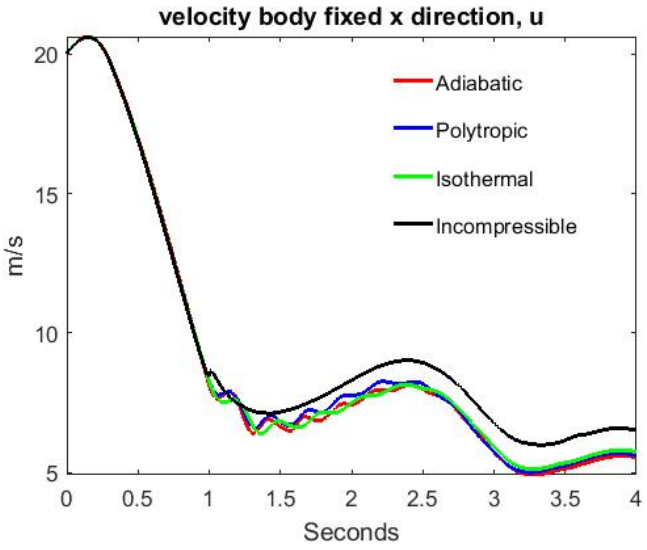

Figure 12.8: Velocity in x_{body} direction

The velocity in x_{body} direction for the incompressible case is barely influenced by the acceleration peak at cavity closure, indicating that the acceleration happens over a very short duration. The velocities in x_{body} direction for the compressible models start to oscillate after cavity closure, due to the oscillating accelerations mentioned in 12.2. The velocities for the compressible models are all of less magnitude for x_{body} direction, compared to the incompressible, seen from Table 12.2 after cavity closure. Therefore, the impulse from the acceleration peak in x_{body} direction for the incompressible air could be the reason. The influence of different velocity in x_{body}direction at water exit is shown in Figure 12.11. The entrapped air on the aft part creates a suction in negative x_{body} direction, influencing the acceleration and then also the velocities. Since the entrapped air for the incompressible just implodes, instead of oscillating in size, the suction might be present for a longer time. This is only a possibility, as the VOF pictures not give a good indication on the volume of the entrapped air, since the pictures are in 2D.

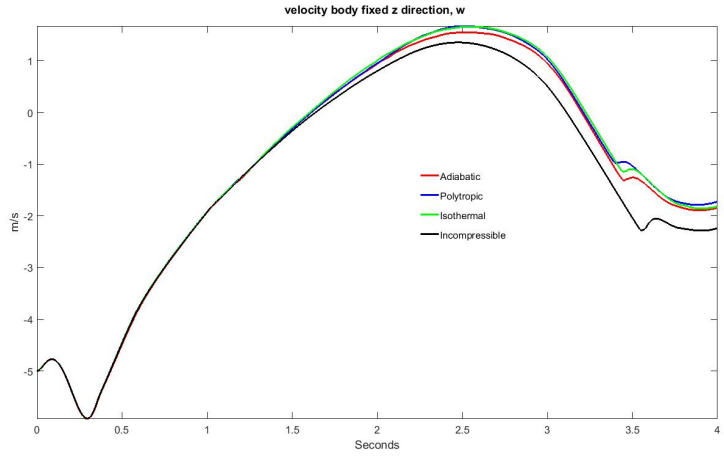

Figure 12.9: Velocity in z_{body} direction

The velocity in z_{body} shown in Figure 12.9 are quite similar for all the models up until 1.5 seconds, where the compressible models later on shows larger velocity in z_{body} direction. The sudden change of the velocities after approximately 3.4 seconds are due to different time of the second water entry, mentioned in 12.2.

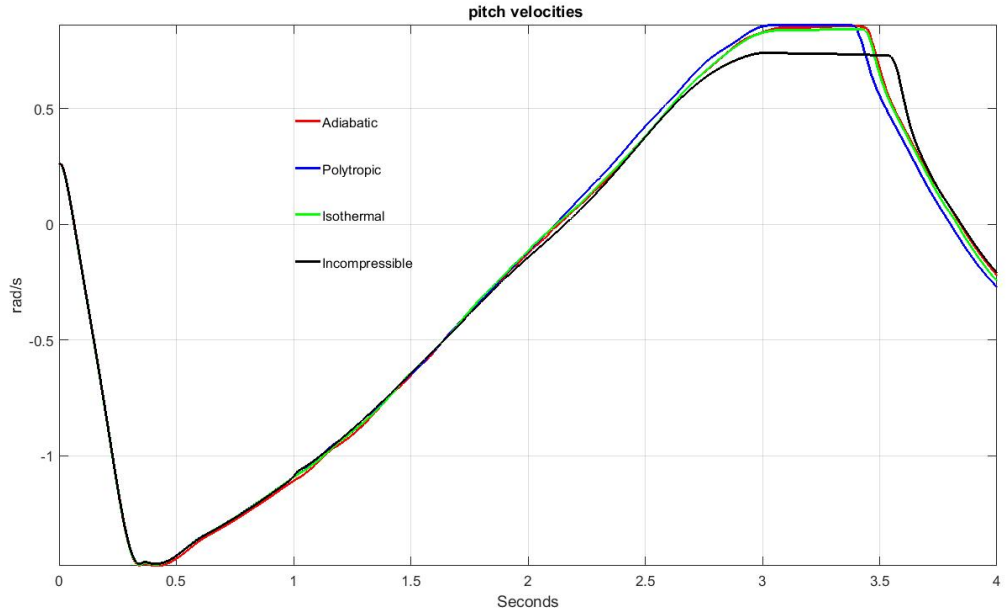

Figure 12.10: Pitch velocity

The compressible air models have lower velocity in x_{body} direction at water exit compared to the incompressible model, resulting in a higher positive pitch velocity when the body breaches the surface. This is shown in Figure 12.11.

a) b)

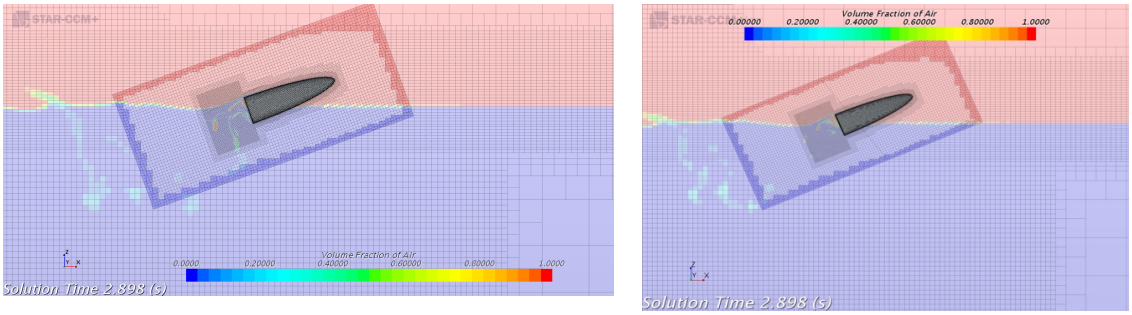

Figure 12.11: water exit for a) polytrophic gas relation and b) incompressible model after 2.898 seconds

12.4 Motion

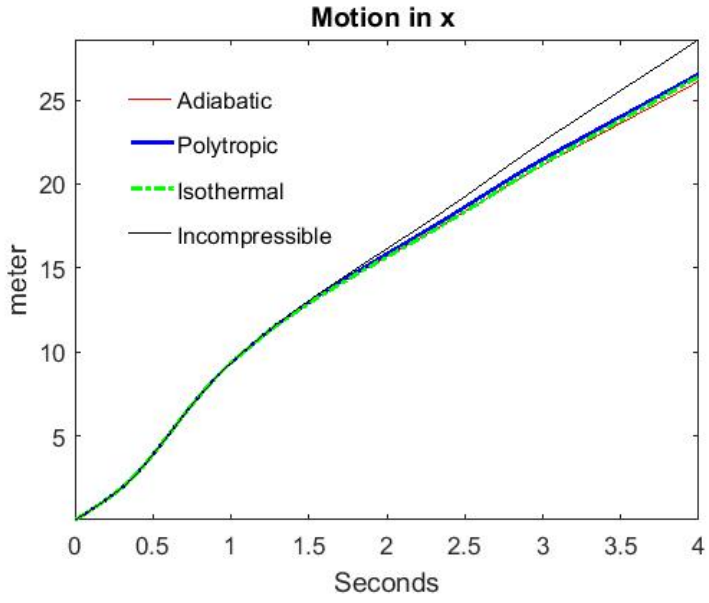

Figure 12.12 Sailing distance measured in meters from origin in water entry

The sailing distance for the compressible model is quite smaller then for the incompressible, seen from Figure 12.12 and Table 12.2. This is a result of the different velocities shown earlier, though the reason for the velocity difference is not certain.

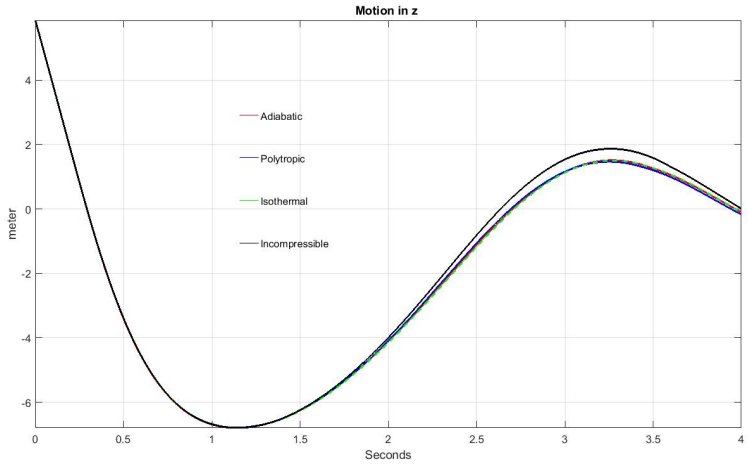

Figure 12.13 Submergence for the lifeboat measured from COG_{body}

Seen from Figure 12.13 and Table 12.2, the maximum submergence is almost equal for all the simulations. Hydrostatic pressure will contribute to additional pressure on the hull, and deformations

might be critical where the geometry is asymmetric, like a wheel house or other appendages. The hydrostatic pressure is increasing proportionally to the submergence, assuming constant density. Hence, maximum submergence is an important parameter to investigate. For this geometry, no wheel house or appendages are present, therefore, the submergence height is only measured from $\mathrm{COG}_{\mathrm{body}}$

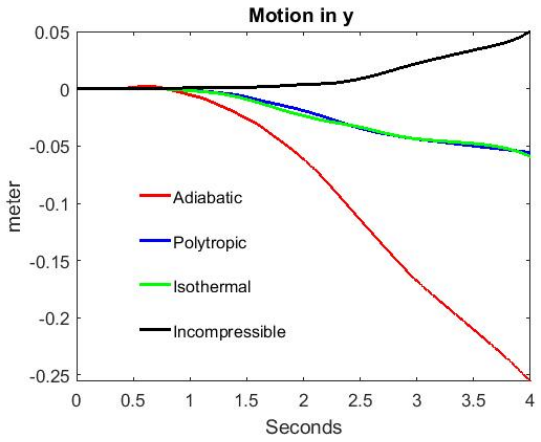

Figure 12.14: Motion in y direction measured from COG_{global}

The motion in y direction is close to zero for the incompressible simulation, polytrophic gas relation and isothermal condition. The adiabatic process has moved 25cm in y direction compared to COG_{global}. The motion in y direction (though zero initial velocities or accelerations in that direction is applied) is possible due to the asymmetric vortex shedding, mentioned in 12.2 All the plots showing velocity or acceleration in y_{body}direction has not been included as the plots are very similar.

METHOD	MAXIMUM SUBMERGENCE	SAILING DISTANCE AFTER 4 SECONDS	VELOCITY IN x_{body} DIRECTION AFTER 4 S	FIRST PRESSURE PEAK TIME	SECOND WATER ENTRY TIME
INCOMPRESSIBLE	-6.7966 m	28.5181 m	6.5264 m/s	1.007	3.581
ISOTHERMAL	-6.7937 m	26.31 m	5.7396 m/s	1.134	3.462

POLYTROPHIC	-6.7912 m	26.55 m	5.6199 m/s	1.098	3.408
ADIABATIC	-6.7957 m	26.1126 m	5.5493 m/s	1.101	3.462

Table 12.2 Key parameters measured from center of gravity

12.5 Damping

Damping give an indication of the reduction of an amplitude as a result of dissipation of kinetic and potential energy of the system (Abrahamsen, 2011). The damping is relevant regarding the compressible models, as it offers another comparison with experimental values.

12.5.1 Method

For a free decay of a under damped linear mass system, the pressure peak would follow the formula

$$P_i = C * e^{-\alpha t_i / T_a} \qquad [49]$$

Where C is dependent on the initial conditions. The damping ratio, $\xi = \alpha/(2\pi)$, where α can be found by plotting the pressure oscillation on a log linear plot. Abrahamsen plotted the average amplitude ($(P_i + P_{i+1})/2$) non-dimensional with respect to the first pressure peak, P_1 as a function of time ($(t_i + t_{i+1})/2$) made non-dimensional with respect to the average period T_a. Abrahamsen plotted the average pressure amplitude because his pressure oscillations did not accurately oscillate around zero. He then determined $-\alpha$ from the slope of the straight line fitted peak values in the log linear plot.
Since the pressure oscillations I have obtained resembles Abrahamsen's pressure oscillation s and don't accurately oscillate around zero, this same procedure has been followed. In addition, Tregde has used this procedure as well, making it easier to compare the damping ratios obtained. It is assumed small linear damping relative to the critical damping, in order to compare the pressure oscillations with a free decay of a linear mass spring system. If this is the case, the pressure amplitude should form a straight line in the logarithmic plot.

12.5.2 Subtracting the hydrostatic pressure

The hydrostatic pressure is included in the pressure oscillations on the aft part, shown in Figure 12.1. Since the hydrostatic pressure throughout the simulation is varying as a result of the different submergence height, the pressure peak from Figure 12.1 should be modified in pursuance of an accurate damping representation. To account for the hydrostatic pressure, the submergence height (measured from center of the aft part) was multiplied with the gravitational acceleration and density of the surrounding liquid and then subtracted. The surrounding liquid has not a constant density due to the air water mixture and entrapped air. In addition, the fluid velocity on the outside of the air bubble will likely influence the pressure inside the air bubble. However, this procedure was first followed with unsatisfactory results. Instead, a second order Butterworth high pass filter was applied to the output data of the pressure oscillation. The frequencies below 1Hz were attenuated, under the assumption that the hydrostatic pressure has a much lower frequency, compared to the natural frequency of the air cavity. Seen from Figure 12.2, and mentioned in 12.1, the natural frequency for the various compressible models are significantly larger than the frequencies of the signal that has been attenuated. The resulting dynamic pressure is shown in Figure 12.15, where the “hydrostatic” represent the pressure that has been removed when the mentioned filter is applied.

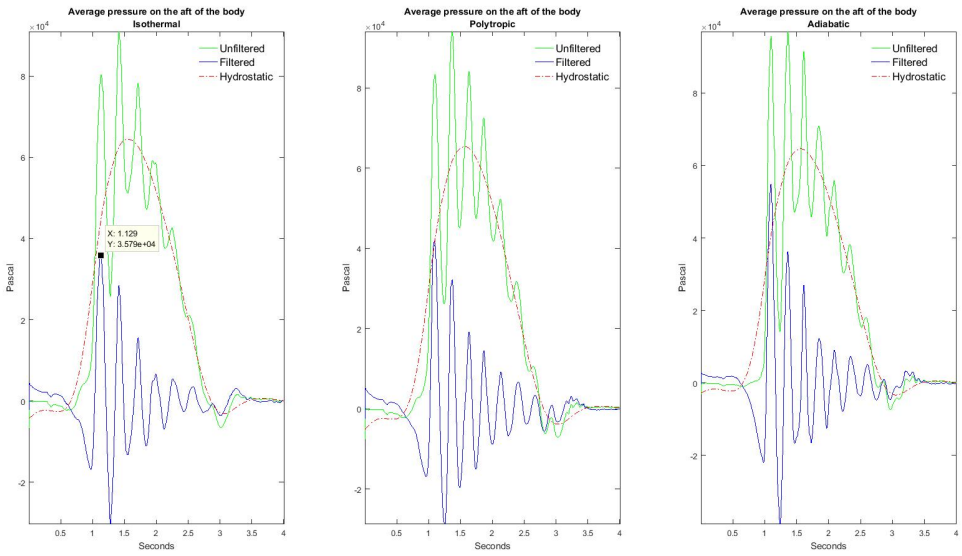

Figure 12.15: Pressure oscillations on the aft part of the body, where the green lines are the pressure oscillations shown in Figure 12.1. The blue line represents the dynamic pressure, where the high pass Butterworth filter has attenuated frequencies related to the hydrostatic pressure.

12.5.3 Damping ratio

The none dimensional average dynamic amplitude (obtained from Figure 12.15) where plotted log linear against the average none dimensional oscillation period, Figure 12.16

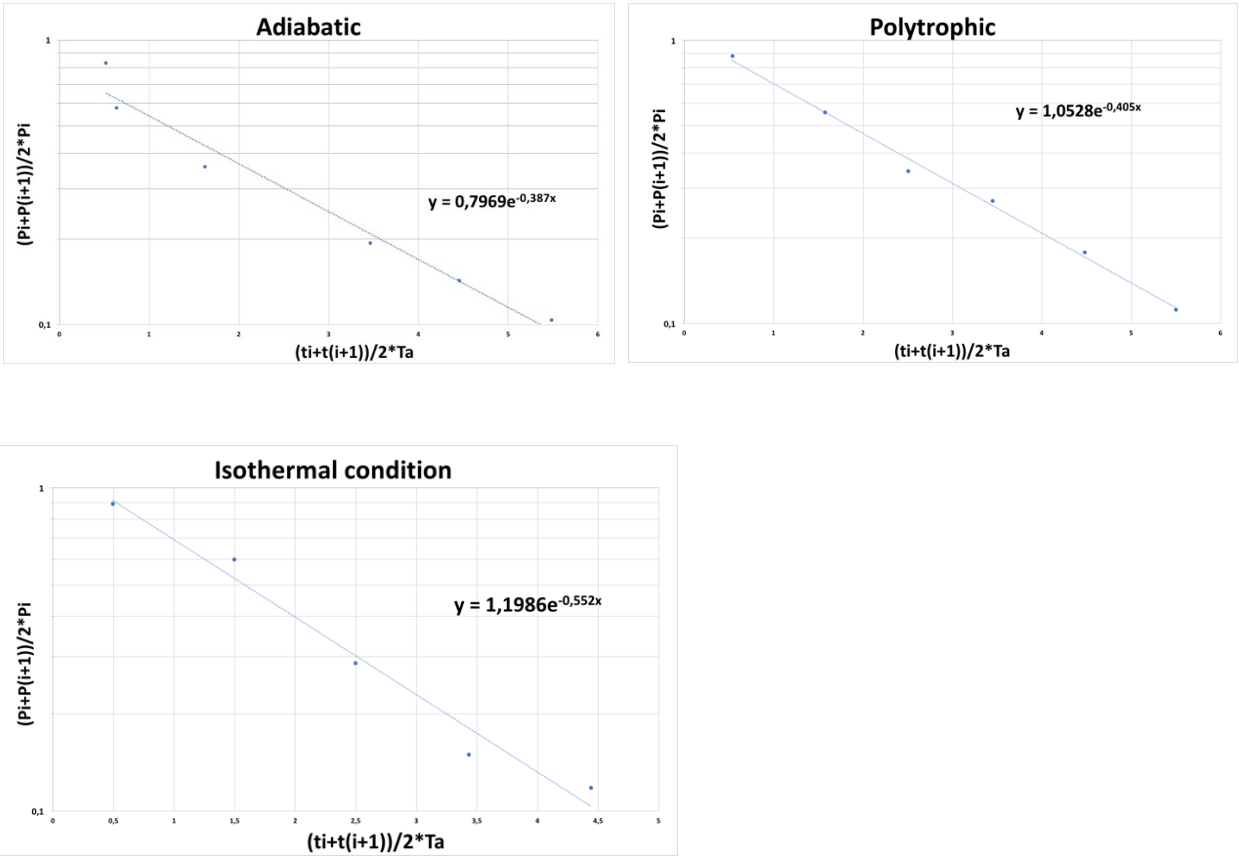

Figure 12.16: None dimensional pressure peaks plotted log linear against none dimensional period for Adiabatic process, Polytrophic and isothermal condition

COMPRESSIBLE MODEL	DAMPING RATIO, ξ
ISOTHERMAL	0.088
ADIABATIC	0.062
POLYTROPHIC	0.064

Table 12.3: Damping ratio for different compressible models

The isothermal condition indicates largest damping ratio, while the polytrophic is slightly greater then adiabatic. The assumption that the steepness from a linear log plot is $-\alpha$, is based on equation [49],

which is only accurate if the points are close to the fitted line. Ideally, there should have been more data, to improve the accuracy of the fitting line, but since the water exit start approximately around 2.7 seconds, no more pressure peaks were present. Seen from Figure 12.16, the isothermal condition and adiabatic process have at least one observation relatively far away from the fitted line. The polytrophic gas relation has most points close to the fitted line. Tregde followed the same procedure, where he studied the damping ratio on the part behind the wheel house. As a result of possibly smaller initial cavity volume, resulting in a higher natural frequency, Tregde had more pressure peaks available to get a better estimation of the fitting line, seen from Figure 12.17. Tregde got the lowest damping ratio for isothermal, in complete opposite of my results. In Figure 12.17 for T=15 ℃ (isothermal condition), the fitting line seems to give an inaccurate estimate of the actual damping as the two first none dimensional pressure amplitudes are significantly higher than the fitting line. The linear trend in the log linear plots from Tregde are better represented for polytrophic and adiabatic compared to the isothermal, where the polytrophic indicates the highest damping ratio, which is very close to the damping ratio obtained from experiments. It is worth mentioning that Tregde used another filter and possibly a different cut of frequency for subtraction of the hydrostatic pressure.

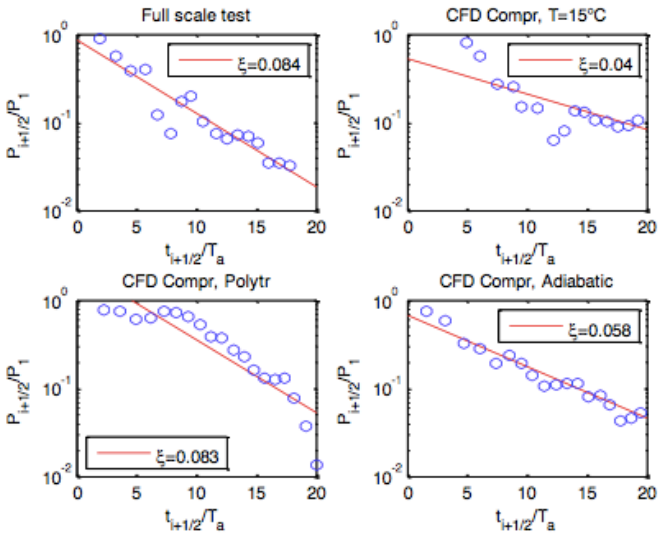

Figure 12.17: Damping ratios from Tregdes paper with various compressible air models (Tregde, 2015)

13 Further work

- Do the convergence study all over again by decreasing the cell size for the coarsest mesh discretization

- Parameter investigation also for compressible air, to se how the natural frequency and damping is influenced by different initial conditions

- More research on the problems related to 2. order temporal discretization in combination with compressible air simulations and segregated flow solver.

- Conduct experiments of the same geometry and initial conditions, making it easier for comparisons and validation of results.

- More research on the process of subtracting the surrounding hydrostatic pressure with focus on the various filter and cut of ratio.

- Comparing pressure sensors distributed on the aft part of the body to cheek for spatial constant pressure.

- Find a better way to capture the behavior of the air cavity in 3D

- Investigate the influence of damping for even lower values for the polytrophic index.

14 Conclusion

The convergence study conducted for incompressible air indicated low convergence rate for all the integrated quantities. Similar motion path for all the mesh discretization suggest that global convergence was obtained. Local converging regarding acceleration in x_{body}direction and pressure on the aft part close to cavity closure was not the case, though the cavity closure time appeared very close for the two finest mesh discretization's. The coarsest mesh discretization might have been to coarse, influencing the simulation of the physics. Therefore, the assumption made for obtaining the order of accuracy is no longer valid. A better way of calculating the order of accuracy would have been to use a finer mesh discretization, where the simulated physic was not affected. The sensitivity analysis for incompressible and compressible air, showed that the number of inner iterations had to be increased from 10 to 25 iteration to satisfy the continuity equation for compressible air.

From the parameter investigation for incompressible air, parameters such as sailing distance and maximum submergence were less influenced of a change in vertical position of the center of gravity. The submergence height was most influenced by the alteration of water entry angle. The cavity closure occurred earlier for higher velocities, corresponding with theory mentioned in the literature study. In addition, the different initial velocities contributed to the largest difference in terms of sailing distance.

Incompressible air simulations are most likely appropriate when estimating passenger safety, since the large acceleration peak in x_{body} direction can be removed when applying a filter for the calculations of the CAR indexes. Pressure peaks may cause local failure on the lifeboat, therefore, filters should not be used for the purpose of removing pressure peaks, since they may influence the structural integrity. Hence, air should be modelled as compressible for an accurate assessment of the structural capacity.

The pressure measured on the aft part of the body started to oscillate after cavity closure for all the three simulations with compressible air modelled, while the incompressible simulation only showed on distinctive pressure peak with a much greater amplitude. The first pressure peak was also observed later, which might be a result of the compression of the entrapped air, before creating an instant push on the aft part of the body. The natural frequency of the entrapped air was highest for the adiabatic model, slightly lower for polytrophic and lowest for the isothermal condition. The damping ratio was found slightly higher for polytrophic compared to adiabatic, strengthening Abrahamsen theory that the heat exchange from an air cushion contributes to damping. However, the isothermal condition

suggested the highest damping ratio, closest to the damping ratio Tregde obtained for full scale experiment. The natural frequency of the entrapped air is possibly under predicted for the isothermal condition. The adiabatic process assumes no heat exchange from the air cavity, which seems to influence the damping of the pressure amplitudes. Therefore, polytrophic model is what I would recommend using for further work due to the higher natural frequency compared with isothermal condition and slightly higher damping ratio than adiabatic, although more research is need to be curtain.

References

Abrahamsen, B. C., 2011. *Sloshing induced tank-roof impact with entrapped air pocket,* s.l.: s.n.

Berchiche, N., Östman, A., Hermundstad, O. A. & Reinholdtsen, S.-A., 2015. *Experimental validation of CFD simulations of Free-Fall Lifeboats launches in Regular Waves,* s.l.: s.n.

Califano, A. & Brinchmann, K., 2013. *Evaluation of Loads During a Free-Fall Lifeboat Drop,* s.l.: ASME.

Colicchio, G., Greco, M. & Faltinsen, O. M., 2006. *A BEM-level set domain-decomposition strategy for non-linear and fragmented interfacial flows,* s.l.: INTERNATIONAL JOURNAL FOR NUMERICAL METHODS IN ENGINEERING.

Consultance, M., 2017. *Marin Consultance.* [Internett]
Available at: http://www.mcl.co.tt/product/norsafe-free-fall-lifeboat/

DNV-GL, 2010. *Environmental Conditions and Environmental Loads,* s.l.: s.n.

DNV-GL, 2016. *Design of free-fall lifeboats,* s.l.: DNV-GL.

Engineering ToolBox, u.d. *Engineeringtoolbox.* [Internett]
Available at: http://www.engineeringtoolbox.com/fluid-density-temperature-pressure-d_309.html
[Funnet 01. May 2017].

Faltinsen, O. M., 1990. *SEA LOADS ON SHIPS AND OFFSHORE STRUCTURES.* s.l.:Cambridge university press.

Faltinsen, O. M. & Greco, M., 2013. *CFD and Wave and Current Induced Loads on Offshore.* s.l.: NTNU.

Faltinsen, O. M. & Timokha, A. N., 2009. *Sloshing.* s.l.:Cambridge university press.

Faltinsen, O. M. & Timokha, A. N., 2009. Sloshing. I: s.l.:Cambridge University Press, pp. 506-510.

Fouques, S. & Hermundstad, O. A., 2016. *Structural Integrity Assessment of Free-Fall Lifeboats by combining fast Monte-Carlo simulations with CFD by means of Proxy Load variables,* s.l.: ASME.

Gekle, S. et al., 2008. *Noncontinous Froude Number Scaling for the Closure Depth of a Cylindrical Cavity ,* s.l.: The American Physical Society.

Gradstein & Ryzhik, 1965. *Tables of integrals ,* s.l.: Acedemic press.

Greco, M., 2012. *TMR4215 - Sea Loads - Lecture Notes,* s.l.: s.n.

Hirt, C. W. & Nichols, B., 1979. *Volume of fluid (VOF) Method for the dynamics for free boandaries ,* Los Alamos: Los Alamos Scientific Laboratory .

J. Andreson, G. D. J. D. E. D. R. G. J. V., 2009. *Computional Fluid Dynamics.* Berlin: Springer.

Jin, J., Ringen, E. & Reinholdtsen, S.-A., 2014. *Forward Distance Performance of a Free Fall Lifeboat in a Seaway,* s.l.: ISOPE.

Kieffer, S. W., 1977. *Sound Speed in Liquid-Gas mixtures: Water-Air and Water-Steam,* s.l.: s.n.

Kim, G.-H. & Park, S., 2016. *Development of numerical simulation tool for efficient and robust prediction of ship resistance,* s.l.: International Journal of Naval Architecture and Ocean Engineering.

McWilliam, D. & Duggins, R. K., 1969. *Speed of sound in Bubbly Liquids,* s.l.: s.n.

NTNU HPC Group, 2016. [Internett]
Available at: https://www.hpc.ntnu.no/display/hpc/About+Vilje

Ommundsen, A., 2014. *Air Cavity Dynamics of Free Fall Lifeboats: Hydrodynamic Study,* s.l.: NTNU.

Sauder, T. & Fouques, S., 2009. *Theoretical Study of the Water Entry of a Body in Waves. Application to Safety of Occupants in Free-Fall Lifeboats,* s.l.: s.n.

Steve CD adapco, 2016. *User guide Star-CCM+ version 11.06,* s.l.: https://stevedocs.cd-adapco.com/starccmplus_latest_en/index.html?param=gYuRe#page/STARCCMP%2FGUID-899D7E79-198D-4E90-B064-F085542B954F%3Den%3D.html%23.

Tregde, V., 2015. *Compressible Air Effects in CFD Simulations of Free Fall Lifeboat Drop,* s.l.: s.n.

Truscott, T. T., Epps, B. P. & Belden, J., 2013. *Water Entry of Projectiles,* s.l.: s.n.

Truscott, T. T., Epps, B. P. & Munns, R. H., 2016. *Water exit of buoyant spheres,* s.l.: American Physical Society .

White, F. M., 2006. *Viscous fluid flow.* Singapore: McGraw-hill companies .

Yan, H., Liu, Y., Kominiarczuk, J. & Yue, D. K. P., 2009. *Cavity dynamics in water entry at low Froude numbers,* s.l.: Cambridge university.

Ytrehus, T., u.d. *The gouverning conservation equations in fluid mechanics,* Trondheim: NTNU.